STATE OF THE CLIMATE IN 2024

THE ARCTIC

R. L. Thoman, T. A. Moon, and M. L. Druckenmiller, Eds.

Special Online Supplement to the *Bulletin of the American Meteorological Society* Vol. 106, No. 8, August, 2025

https://doi.org/10.1175/BAMS-D-25-0104.1

Corresponding author: Richard L. Thoman / rthoman@alaska.edu

STATE OF THE CLIMATE IN 2024

The Arctic

Editors

Jessica Blunden
James Reagan

Chapter Editors

Anthony Arguez
Josh Blannin
Peter Bissolli
Kyle R. Clem
Howard J. Diamond
Matthew L. Druckenmiller
Robert J. H. Dunn
Catherine Ganter
Nadine Gobron
Gregory C. Johnson
Rick Lumpkin
Rodney Martinez
Ademe Mekonnen
Twila A. Moon
Gary A. Morris
Marilyn N. Raphael
Carl J. Schreck III
Laura Stevens
Richard L. Thoman
Kate M. Willett
Zhiwei Zhu

Technical Editor

Lukas Noguchi

BAMS Special Editor for Climate

Timothy DelSole

American Meteorological Society

Cover Credit:
Mulgrove Hills tundra landscape of shrubs, rock, and snow in the Alaskan Arctic.
Photo credit: J. J. Frost

How to cite this document:

The Arctic is one chapter from the *State of the Climate in 2024* annual report and is available from https://doi.org/10.1175/BAMS-D-25-0104.1. Compiled by NOAA's National Centers for Environmental Information, *State of the Climate in 2024* is based on contributions from scientists from around the world. It provides a detailed update on global climate indicators, notable weather events, and other data collected by environmental monitoring stations and instruments located on land, water, ice, and in space. The full report is available from https://doi.org/10.1175/2025BAMSStateoftheClimate.1.

Citing the complete report:

Blunden, J. and J. Reagan, Eds., 2025: "State of the Climate in 2024". Bull. Amer. Meteor. Soc., 106 (8), Si–S513 https://doi.org/10.1175/2025BAMSStateoftheClimate.1.

Citing this chapter:

Thoman, R. L., T. A. Moon, and M. L. Druckenmiller, Eds.,
2025: The Arctic [in "State of the Climate in 2024"]. Bull. Amer. Meteor. Soc., 106 (8), S300–S356, https://doi.org/10.1175/BAMS-D-25-0104.1.

Citing a section (example):

Smith, S. L., V. E. Romanovsky, K. Isaksen, K. E. Nyland, N. I. Shiklomanov, D. A. Streletskiy, and H. H. Christiansen, 2025: Permafrost [in "State of the Climate in 2024"]. Bull. Amer. Meteor. Soc., 106 (8), S338–S341, https://doi.org/10.1175/BAMS-D-25-0104.1.

Editor and Author Affiliations (alphabetical by name)

Askjaer, Thomas G., Danish Meteorological Institute, Copenhagen, Denmark

Ballinger, Thomas J., International Arctic Research Center, University of Alaska Fairbanks, Fairbanks, Alaska

Bhatt, Uma S., Geophysical Institute, University of Alaska Fairbanks, Fairbanks, Alaska

Berner, Logan T., School of Informatics, Computing, and Cyber Systems, Northern Arizona University, Flagstaff, Arizona

Bernhard, Germar H., Biospherical Instruments Inc., San Diego, California

Bigalke, Siiri, Department of Geography, Portland State University, Portland, Oregon

Bjerke, Jarle W., Norwegian Institute for Nature Research, Trondheim, Norway; FRAM – High North Research Centre for Climate and the Environment, Tromsø, Norway

Bliss, Angela, NASA Goddard Space Flight Center, Greenbelt, Maryland

Box, Jason E., Geological Survey of Denmark and Greenland (GEUS), Copenhagen, Denmark

Brady, Mike, Climate Research Division, Environment and Climate Change Canada, Toronto, Canada

Brettschneider, Brian, NOAA/NWS Alaska Region, Anchorage, Alaska

Butler, Amy H., Chemical Sciences Laboratory, Boulder, Colorado

Christiansen, Hanne H., Arctic Geophysics Department, University Centre in Svalbard, Longyearbyen, Norway

Crawford, Alex, Department of Environment and Geography, University of Manitoba, Winnipeg, Canada

Decharme, Bertrand, Centre National de Recherches Météorologiques, Météo-France/CNRS, Toulouse, France

Derksen, Chris, Climate Research Division, Environment and Climate Change Canada, Toronto, Canada

Divine, Dmitry, Norwegian Polar Institute, Fram Centre, Tromsø, Norway

Druckenmiller, Matthew L., National Snow and Ice Data Center, Cooperative Institute for Research in Environmental Sciences, University of Colorado, Boulder, Colorado

Elias Chereque, Alesksandra, Department of Physics, University of Toronto, Toronto, Canada

Epstein, Howard E., Department of Environmental Sciences, University of Virginia, Charlottesville, Virginia

Farrell, Sinead, Department of Geographical Sciences, University of Maryland, College Park, Maryland

Fausto, Robert S., Geological Survey of Denmark and Greenland (GEUS), Copenhagen, Denmark

Fettweis, Xavier, SPHERES Research Unit, University of Liège, Liège, Belgium

Fioletov, Vitali E., Environment and Climate Change Canada, Toronto, Canada

Forbes, Bruce C., Arctic Centre, University of Lapland, Rovaniemi, Finland

Frost, Gerald V. (JJ), Alaska Biological Research, Inc., Fairbanks, Alaska

Gerland, Sebastian, Norwegian Polar Institute, Fram Centre, Tromsø, Norway

Grooß, Jens-Uwe, Forschungszentrum Jülich (ICE-4), Jülich, Germany

Hanna, Edward, Department of Geography and Lincoln Climate Research Group, Lincoln, United Kingdom

Hendricks, Stefan, Alfred Wegener Institute, Helmholtz Centre for Polar and Marine Research, Bremerhaven, Germany

Howell, Stephen, Climate Research Division, Environment and Climate Change Canada, Toronto, Canada

Ialongo, Iolanda, Finnish Meteorological Institute, Helsinki, Finland

Isaksen, Ketil, Norwegian Meteorological Institute, Oslo, Norway

Jia, Gensuo, Institute of Atmospheric Physics, Chinese Academy of Sciences, Beijing, China

Johnsen, Bjørn, Norwegian Radiation and Nuclear Safety Authority, Østerås, Norway

Kaleschke, Lars, Alfred Wegener Institute, Helmholtz Centre for Polar and Marine Research, Bremerhaven, Germany

Kim, Seong-Joong, Korea Polar Research Institute, Incheon, South Korea

Labe, Zachary M., Geophysical Fluid Dynamics Laboratory, Princeton, New Jersey

Lader, Rick, International Arctic Research Center, University of Alaska Fairbanks, Fairbanks, Alaska

Lakkala, Kaisa, Finnish Meteorological Institute, Sodankylä, Finland

Lara, Mark J., Department of Plant Biology, University of Illinois, Urbana, Illinois; Department of Geography, University of Illinois, Urbana, Illinois

Lee, Simon H., School of Earth and Environmental Sciences, University of St Andrews, St Andrews, United Kingdom

Loomis, Bryant D., NASA Goddard Space Flight Center, Greenbelt, Maryland

Luojus, Kari, Arctic Research Centre, Finnish Meteorological Institute, Helsinki, Finland

Macander, Matthew J., Alaska Biological Research, Inc., Fairbanks, Alaska

Magnússon, Rúna Í., Plant Ecology and Nature Conservation Group, Wageningen University & Research, Wageningen, Netherlands

Mankoff, Ken D., Business Integra, New York, New York; NASA Goddard Institute for Space Studies, New York, New York

McClelland, James W., Marine Biological Laboratory, Woods Hole, Massachusetts

Medley, Brooke, Cryospheric Sciences Laboratory, NASA Goddard Space Flight Center, Greenbelt, Maryland

Meier, Walter N., National Snow and Ice Data Center, Cooperative Institute for Research in Environment Sciences, University of Colorado, Boulder, Colorado

Montesano, Paul M., NASA Goddard Space Flight Center, Greenbelt, Maryland

Moon, Twila A., National Snow and Ice Data Center, Cooperative Institute for Research in Environmental Sciences, University of Colorado, Boulder, Colorado

Mote, Thomas L., University of Georgia, Athens, Georgia

Motrøen Gjelten, Herdis, Norwegian Meteorological Institute, Oslo, Norway

Mudryk, Lawrence, Climate Research Division, Environment and Climate Change Canada, Toronto, Canada

Müller, Rolf, Forschungszentrum Jülich (IEK-7), Jülich, Germany

Neigh, Christopher S. R., NASA Goddard Space Flight Center, Greenbelt, Maryland

Nyland, Kelsey E., George Washington University, Washington, DC

Overland, James E., NOAA/OAR Pacific Marine Environmental Laboratory, Seattle, Washington

Perovich, Donald K., Dartmouth College, Hanover, New Hampshire

Petty, Alek, NASA Goddard Space Flight Center, Greenbelt, Maryland

Phoenix, Gareth K., School of Biosciences, University of Sheffield, Sheffield, United Kingdom

Poinar, Kristin, University at Buffalo, Buffalo, New York

Ricker, Robert, NORCE Norwegian Research Centre, Tromsø, Norway

Romanovsky, Vladimir E., Geophysical Institute, University of Alaska Fairbanks, Fairbanks, Alaska

Scheller, Johan H., Department of Ecoscience, Arctic Research Centre Aarhus University, Roskilde, Denmark

Serreze, Mark C., National Snow and Ice Data Center, Cooperative Institute for Research in Environmental Sciences, University of Colorado, Boulder, Colorado

Shiklomanov, Alexander I., University of New Hampshire, Durham, New Hampshire; Arctic and Antarctic Research Institute, St. Petersburg, Russia

Shiklomanov, Nikolay I., George Washington University, Washington, DC

Smith, Benjamin E., Polar Science Center, Applied Physics Laboratory, University of Washington, Seattle, Washington

Smith, Sharon L., Geological Survey of Canada, Natural Resources Canada, Ottawa, Canada

Spencer, Robert G. M., Florida State University, Tallahassee, Florida

Streletskiy, Dmitry A., George Washington University, Washington, DC

Suslova, Anya, Woodwell Climate Research Center, Falmouth, Massachusetts

Svendby, Tove, The Climate and Environmental Research Institute NILU, Kjeller, Norway

Tank, Suzanne E., University of Alberta, Edmonton, Canada

Editor and Author Affiliations (continued)

Tian-Kunze, Xiangshan, Alfred Wegener Institute, Helmholtz Centre for Polar and Marine Research, Bremerhaven, Germany

Tedesco, Marco, Lamont-Doherty Earth Observatory, Columbia University, Palisades, New York

Timmermans, Mary-Louise, Yale University, New Haven, Connecticut

Thoman, Richard L., International Arctic Research Center, University of Alaska Fairbanks, Fairbanks, Alaska

Tømmervik, Hans, Norwegian Institute for Nature Research, Trondheim, Norway; FRAM – High North Research Centre for Climate and the Environment, Tromsø, Norway

Tretiakov, Mikhail, Arctic and Antarctic Research Institute, St. Petersburg, Russia

Waigl, Christine F., Geophysical Institute, University of Alaska Fairbanks, Fairbanks, Alaska

Walker, Donald (Skip) A., Institute of Arctic Biology, University of Alaska Fairbanks, Fairbanks, Alaska

Walsh, John E., International Arctic Research Center, University of Alaska Fairbanks, Fairbanks, Alaska

Wang, Muyin, NOAA/OAR Pacific Marine Environmental Laboratory, Seattle, Washington; Cooperative Institute for Climate, Ocean, and Ecosystem Studies, University of Washington, Seattle, Washington

Webster, Melinda, Polar Science Center, Applied Physics Laboratory, University of Washington, Seattle, Washington

Yang, Dedi, Environmental Sciences Division, Oak Ridge National Laboratory, Oak Ridge, Tennessee

Zolkos, Scott, Woodwell Climate Research Center, Falmouth, Massachusetts

Editorial and Production Team

Allen, Jessicca, Graphics Support, Cooperative Institute for Satellite Earth System Studies, North Carolina State University, Asheville, North Carolina

Camper, Amy V., Graphics Support, Innovative Consulting and Management Services, LLC, NOAA/NESDIS National Centers for Environmental Information, Asheville, North Carolina

Carroll, Lauren, Content Team Lead, Communications and Outreach, NOAA/NESDIS National Centers for Environmental Information, Asheville, North Carolina

Haley, Bridgette O., Graphics Support, NOAA/NESDIS National Centers for Environmental Information, Asheville, North Carolina

Love-Brotak, S. Elizabeth, Lead Graphics Production, NOAA/NESDIS National Centers for Environmental Information, Asheville, North Carolina

Ohlmann, Laura, Technical Editor, Innovative Consulting and Management Services, LLC, NOAA/NESDIS National Centers for Environmental Information, Asheville, North Carolina

Noguchi, Lukas, Technical Editor, Innovative Consulting and Management Services, LLC, NOAA/NESDIS National Centers for Environmental Information, Asheville, North Carolina

Riddle, Deborah B., Graphics Support, NOAA/NESDIS National Centers for Environmental Information, Asheville, North Carolina

Veasey, Sara W., Visual Communications Team Lead, Communications and Outreach, NOAA/NESDIS National Centers for Environmental Information, Asheville, North Carolina

5. Table of Contents

5. THE ARCTIC

R. L. Thoman, T. A. Moon, and M. L. Druckenmiller, Eds.

a. Overview

—R. L. Thoman, T. A. Moon, and M. L. Druckenmiller

The Arctic environment in 2024 continued on a trajectory that has put it in a state far different from that of the twentieth century. Ongoing accumulation of greenhouse gases in the atmosphere continues to quickly warm the Arctic, resulting in rapid changes in the cryosphere that are driving cascading impacts to climate, ecological, and societal systems.

Many weather- and climate-related impacts in the Arctic are the result of compounding change, such as increased riverbank erosion, which is proximately due to increased river discharge from higher seasonal precipitation, yet is also exacerbated by thawing permafrost. However, even individual storms occur within very different ocean and ice conditions than were typically present in the late twentieth century. As a result, the impacts, including high winds, excessive precipitation, and coastal inundation, may be quite different nowadays, as exemplified by the October 2024 storm in northwest Alaska that produced severe coastal flooding in several communities. To share some of these impacts with a wider audience, select extreme weather impacts around the greater Arctic have been highlighted through the inclusion of sidebars in recent *State of the Climate* Arctic chapters (e.g., Benestad et al. 2023; Thoman et al. 2024).

Average surface air temperatures for the Arctic overall (poleward of 60°N) for 2024 averaged 1.27°C above the 1991–2020 baseline average, the second-highest annual temperature since records began in 1900. For the 11th consecutive year, the Arctic annual temperature anomaly was larger than the global average anomaly. Seasonally, summer (July–September) 2024 ranked as the third-highest average temperature, and autumn (October–December) 2024 saw its highest average temperature on record. At the subseasonal scale, an intense August heatwave brought all-time record high temperatures to parts of the northwest North American Arctic. Closely but not completely tied to spring and summer air temperature trends, productivity of tundra and boreal forest vegetation has dramatically increased in recent decades. Overall "tundra greenness" was the fifth highest since 1982. However, local to regional "browning" (reduced vegetation productivity) shows that disturbance factors besides temperatures, such as wildfire, can be important.

Sea ice is one of the most iconic features of the Arctic environment and plays an important role in regulating global climate, regional ecosystems, and economic activities. Sea ice extent typically reaches the annual maximum in March, and in 2024 the maximum was near the 1991–2020 average overall, but somewhat below average in the Barents Sea and Gulf of St. Lawrence. The annual minimum sea ice extent occurs in September, and in 2024 the September monthly average was the sixth lowest in the 46-year satellite record. The Northern Sea Route along the north Russia coast opened later than the past 20 years' average due to persistent ice in the southwest Chukchi Sea. The Northwest Passage's southern route through northwest Canada opened again this year and, quite unusually, the deepwater northern route was also almost entirely ice free at the end of September.

Decreasing sea ice extent during the late spring and summer months exposes larger areas of ocean to direct warming during the time of year of high incoming solar radiation. Poleward of 65°N, open ocean surface temperatures typically peak in August. In 2024, late summer sea surface temperature anomalies showed significant regional variability, with the waters in the Barents and Kara Seas 2°C–4°C warmer than normal. In sharp regional contrast, Chukchi Sea sea surface temperatures were the lowest in more than 40 years, while just to the east, sea surface temperatures in the southern Beaufort Sea were significantly above the 1991–2020 average.

Like sea ice, permafrost (soils or other earth materials that have remained frozen for at least two years) is an important feature of Arctic environments that occurs widely on land and throughout some submarine continental shelf areas that were exposed land during the last Ice Age (about 15,000 years ago). Unlike many parts of the Arctic environmental system, permafrost temperatures and the summer surface thaw zone cannot be monitored from space-borne instruments and depend on in situ measurements. While long-term observations are not available over most of the Asian Arctic, observations elsewhere show multi-decade warming of deeper permafrost continuing across the Arctic, with some sites in North America and Svalbard having seen their highest temperatures on record in 2024. Overall, colder permafrost is warming more rapidly; areas where permafrost temperatures are close to freezing have slower rates of warming as ice changes phase to liquid water.

Precipitation monitoring in the Arctic has historically been limited due to the lack of in situ measurements over the Arctic Ocean, a sparse land station network, and significant problems with solid precipitation undercatch because of the inherent difficulties in capturing solid precipitation in strong wind environments. Recent advances in reanalyses that combine observations and computer simulations now allow for more robust regional-scale precipitation analysis and historical comparisons. In 2024, Arctic-wide annual precipitation was the third highest on record, and summer (July through September) precipitation was the highest since 1950. Rivers serve as regional integrators of precipitation. Arctic river discharge overall for both 2023 and 2024 was close to the 1991–2020 average, albeit with significant differences across basins. For example, in North America, Mackenzie River discharge was well below average in both years, but Yukon River discharge was above average in both years; most basins in Eurasia saw above-normal discharge in 2024 but below-average discharge in 2023.

In much of the Arctic, snow is the dominant form of precipitation for most of the year, and the presence or absence of snow cover is a critical factor in many climate and environmental processes. During the 2023/24 snow season, there were marked regional and continental scale differences in snow cover duration. The snow cover duration varied from the shortest to date in the twenty-first century over parts of Canada to at or near the longest in this century in parts of the Nordic and Asian Arctic.

Melt and discharge from the Greenland Ice Sheet play important roles in modulating North Atlantic weather and climate. In 2024, the total amount of ice decreased, as it has every year since the late 1990s, but the loss was 50%–80% less than the 2002–23 annual average. This was the result of an unusual but persistent weather pattern that inhibited the development and persistence of warm air masses over Greenland during the summer. Ongoing monitoring of the Greenland Ice Sheet, which holds enough water to raise global sea levels by more than seven meters if entirely melted, is critical for understanding drivers of melt and ice sheet dynamics.

The Arctic stratosphere experienced two major sudden warming events early in 2024 that resulted in enhanced ozone transport into the region from lower latitudes. As a result, surface ultraviolet radiation was reduced in parts of the Asian Arctic in spring and the central Arctic and North America in summer.

Special Notes: The 1991–2020 baseline is used in this chapter except where data availability requires use of a different baseline. This chapter includes a focus on Arctic river discharge (section 5h), which alternates yearly with a section on glaciers and ice caps outside of Greenland.

b. Atmosphere

—A. H. Butler, S. H. Lee, G. H. Bernhard, V. E. Fioletov, J-U. Grooß, I. Ialongo, B. Johnsen, K. Lakkala, R. Müller, and T. Svendby

The dynamics and chemistry of the Arctic atmosphere are affected by both strong year-to-year internal variability and long-term changes forced by greenhouse gases, ozone-depleting substances, and aerosols. The atmosphere is also closely coupled to Arctic sea ice and snow cover; positive feedbacks with sea ice loss have amplified long-term polar atmospheric warming (Dai et al. 2019; He et al. 2024).

In 2024, the most notable features of the atmospheric circulation were: 1) an unusually disturbed Arctic stratospheric polar vortex, with two reversals of the zonal winds at 60°N and 10 hPa (known as major sudden stratospheric warmings [SSWs]; Baldwin et al. 2021); 2) persistently high total column ozone corresponding to substantial reductions in surface ultraviolet (UV) radiation from spring through summer; 3) a monthly record-high positive Arctic Oscillation in August, corresponding to low sea level pressure anomalies over the Arctic, despite strong blocking high pressure aloft; and 4) persistent blocking high pressure over the Hudson Bay that lasted throughout summer and autumn.

1. THE ARCTIC STRATOSPHERE IN 2024

The Arctic stratosphere experienced two SSWs: one on 16 January and another on 4 March 2024 (Qian et al. 2024; Lee et al. 2025). The occurrence of two SSWs in a single winter is relatively unusual, occurring only about once every decade (Lee et al. 2025). These events are evident in Fig. 5.1a that shows a metric of large-scale circulation, the polar cap (60°N–90°N) averaged geopotential height (PCH), which is the altitude of a given atmospheric pressure. In general, when the PCH is anomalously positive, the polar circulation is predominantly anti-cyclonic, and the polar air is warmer (and vice versa when the PCH is anomalously negative). Near the surface, the PCH is negatively correlated with the Arctic Oscillation, the dominant pattern of Northern Hemisphere climate variability that describes a fluctuation in atmospheric mass between the pole and the midlatitudes (Thompson and Wallace 2000). The PCH indicates when the polar

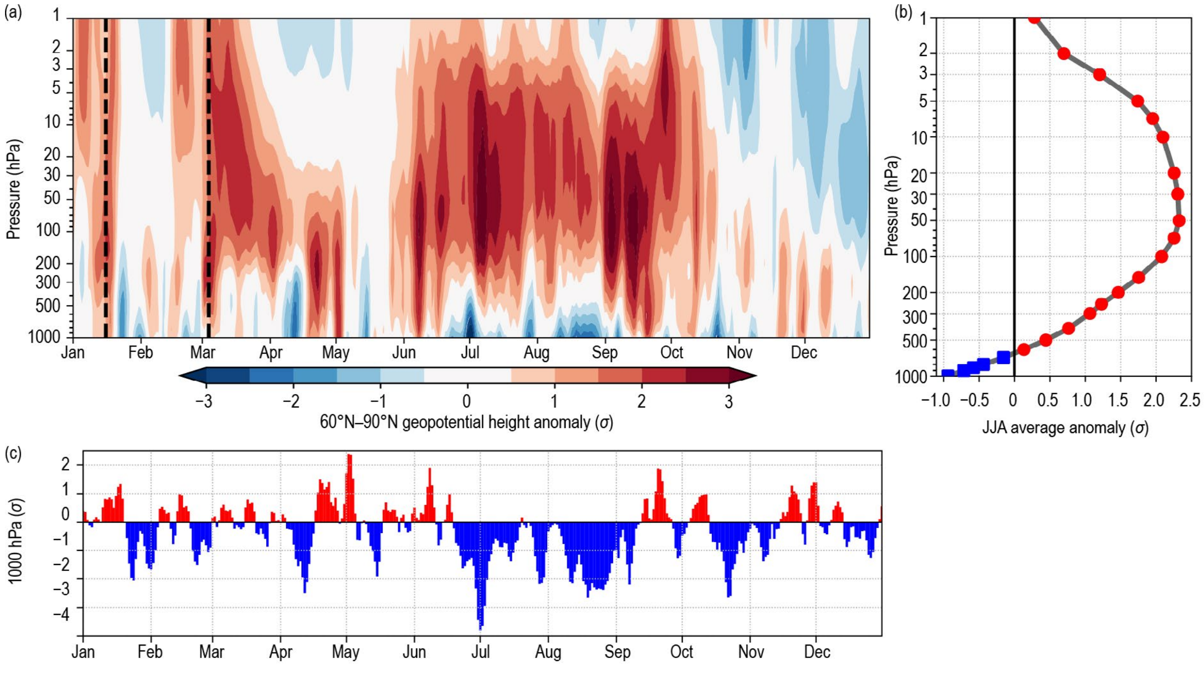

Fig. 5.1. (a) Vertical profile of daily standardized Arctic polar cap (60°N–90°N) geopotential height (PCH) anomalies during 2024. Anomalies are shown with respect to a 30-day centered running mean 1991–2020 climatology and standardized at each pressure level by the standard deviation of each calendar day during 1991–2020 (smoothed with a 30-day running mean). Standardizing makes vertical coupling easier to visualize, given the large differences in magnitude of the raw geopotential height values from the surface to 1 hPa. Dashed vertical lines show the dates of the two 2024 sudden stratospheric warmings. (b) The Jul–Sep average of standardized PCH anomalies. The near-surface PCH anomalies were negative (blue), while upper atmosphere anomalies were positive (red). (c) 1000-hPa standardized PCH anomalies (closely correlated to the Arctic Oscillation, multiplied by –1) for 1 Jan–31 Dec 2024. (Data source: Once-daily 0000 UTC ERA5 at 1° horizontal resolution [Hersbach et al. 2020].)

atmosphere is vertically coupled (i.e., has the same-signed anomalies from the surface to the upper stratosphere).

The two SSWs had limited surface climate impacts via dynamical downward coupling (Lee et al. 2025) but resulted in significant stratospheric ozone transport from the tropics to the Arctic and record-high total column ozone over the polar cap in March (Newman et al. 2024; Fig. 5.2a, Fig 5.4b). After the stratospheric polar vortex dissipated in the spring, this anomalous ozone then persisted in the Arctic throughout summer and into autumn, contributing to new monthly high total column ozone records in May, June, July, and October (Figs. 5.2b, 5.4b). Spatially, 2024 Arctic total column ozone anomalies from the Ozone Monitoring Instrument (OMI; 2005–24) showed large and significant enhancements, especially over Asia in March and the central Arctic/North Atlantic in July (Figs. 5.2a,b). These regions of enhanced ozone corresponded to regions with the strongest surface UV radiation reductions (up to 20%) in those months (Figs. 5.2c,d). Negative UV anomalies calculated from ground-based measurements for some stations were up to 13% larger in magnitude than those from satellite data (OMI instrument; Figs. 5.2c,d). Differences between ground- and satellite-based measurements of UV radiation at the surface are caused by variability within the satellite footprint and by the albedo climatology used in satellite retrievals, which do not always match the actual albedo (Bernhard et al. 2015).

Summer temperatures in the Arctic lowermost stratosphere (~150 hPa) set monthly record highs (Figs. 5.1a, 5.4a). This warmth in the free atmosphere may be in part related to localized absorption of sunlight by the persistent anomalously high ozone that was transported downward from the mid-to-upper stratosphere (e.g., Williams et al. 2024; Fig. 5.4b).

The stratospheric polar vortex reformed at its usual time in late August but stayed anomalously weak until mid-October, and then finally strengthened by December (Fig. 5.1a, blue shading at 10 hPa).

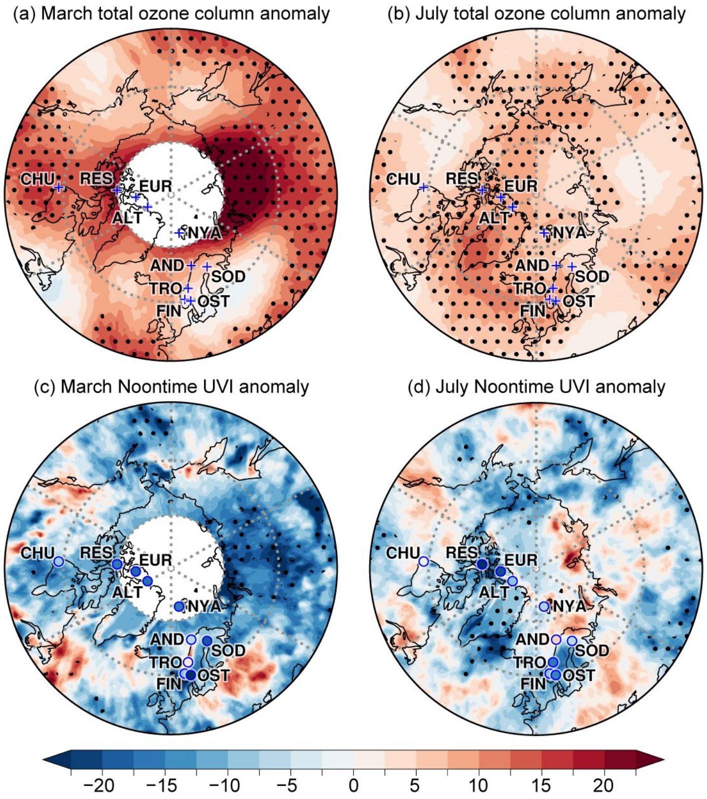

Base	Mar Noontime UVI (satellite)	Mar Noontime UVI (ground-based)	Jul Noontime UVI (satellite)	Jul Noontime UVI (ground-based)
ALT	N/A	−17%	−3%	−9%
EUR	N/A	−18%	−12%	−20%
NYA	N/A	−16%	0%	−7%
RES	N/A	−16%	−15%	−28%
AND	−8%	−6%	−1%	5%
SOD	−10%	−19%	−2%	−6%
TRO	8%	2%	−11%	−16%
FIN	−3%	−9%	−13%	−9%
OST	−19%	−29%	−16%	−15%
CHU	−16%	−8%	−3%	−1%

Fig. 5.2. Monthly mean anomaly maps of (a),(b) total ozone column (%) and (c),(d) noontime ultraviolet index (UVI; %) for Mar (a),(c) and Jul (b),(d) 2024 relative to 2005–23 means. Stippling indicates pixels where anomalies exceed 2 std. dev. Maps are based on the Ozone Monitoring Instrument (OMI) Level-2 Total Column Ozone version 3 (OMTO3) total ozone product (Bhartia and Wellemeyer 2002), which is derived from measurements of the OMI. (c),(d) also compares UVI anomalies from OMI [%] from OMI satellite with ground-based measurements at nine locations (shaded marker). Site acronyms of ground stations are ALT: Alert (83°N); EUR: Eureka (80°N); NYA: Ny-Ålesund (79°N); RES: Resolute (75°N); AND: Andøya (69°N); SOD: Sodankylä (67°N); TRO: Trondheim (63°N); FIN: Finse (61°N); OST: Østerås (60°N); and CHU: Churchill (59°N). White areas centered at the North Pole (and values of N/A in the table) indicate latitudes where OMI data are not available because of polar darkness in March.

2. THE ARCTIC TROPOSPHERE IN 2024

Winter (January–March; JFM) and spring (April–June; AMJ) were generally characterized by statistically insignificant seasonally-averaged 500-hPa geopotential height anomalies across the Arctic (Figs. 5.3a,b). However, anomalous high pressure (or “blocking”) over the Hudson Bay persisted throughout 2024, exceeding +2 std. dev. in summer (July–September; JAS) and autumn

(October–December; OND). This persistent blocking was associated with predominantly northerly upper-tropospheric winds over the Baffin Bay, and may have contributed to less Greenland Ice Sheet melt (see section 5g and Sidebar 5.3).

In addition, summer was marked by strong blocking over the Barents–Kara Seas region, coincident with record-warm August sea surface temperatures over the Barents Sea (section 5e) and anomalously low geopotential heights over the Arctic Ocean and near Iceland (Fig. 5.3c). Despite the overall positive PCH anomalies in the mid- to upper troposphere (Figs. 5.1b,c), the near-surface was characterized by strongly negative PCH anomalies (Figs. 5.1b,c) and anomalously low sea level pressure (section 5c), corresponding to a record-positive (since 1958) Arctic Oscillation for the month of August (Fig 5.4c). In other words, the lowermost Arctic atmosphere was at odds with the circulation above it through most of summer (Fig. 5.1b). A positive Arctic Oscillation pattern typically corresponds to anomalously cool temperatures over the central Arctic, the Bering Strait, and Baffin Bay, but anomalous warmth over northernmost Eurasia, Scandinavia, and North America south of the Hudson Bay (e.g., Park and Ahn 2016). This roughly corresponds to regional surface air temperature (SAT) variations seen during summer 2024 (section 5c).

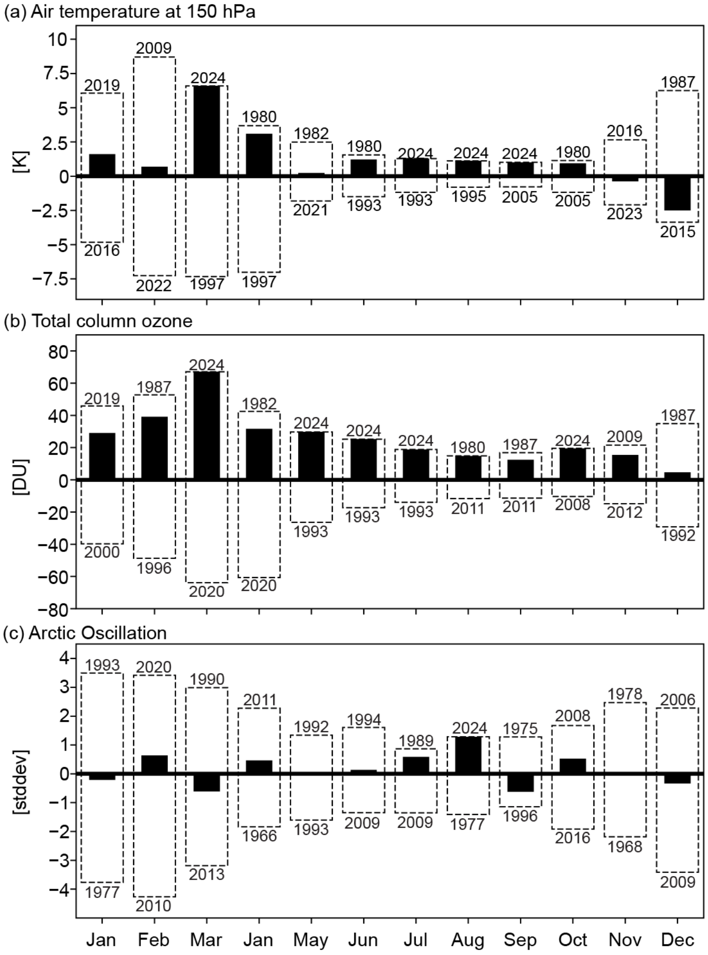

Fig. 5.4. (a) Polar cap averaged temperature anomalies at 150 hPa (~13.5 km) for each month of 2024 (black bars), compared to the previous monthly record (maximum and minimum) values over the period 1958–2024 (dashed bars). The year of the maximum/minimum monthly record is provided. Data are from ERA5 (Hersbach et al. 2020). (b) Same as (a) but for polar cap averaged total column ozone anomalies over the period 1980–2024. Data are from MERRA-2 reanalysis (Gelaro et al. 2017). (c) Same as (a) but for the Arctic Oscillation (AO) over the period 1958–2024. The AO index is from NOAA's Climate Prediction Center. All anomalies are calculated relative to the 1991–2020 climatology. Figure adapted from L'Heureux et al. (2010).

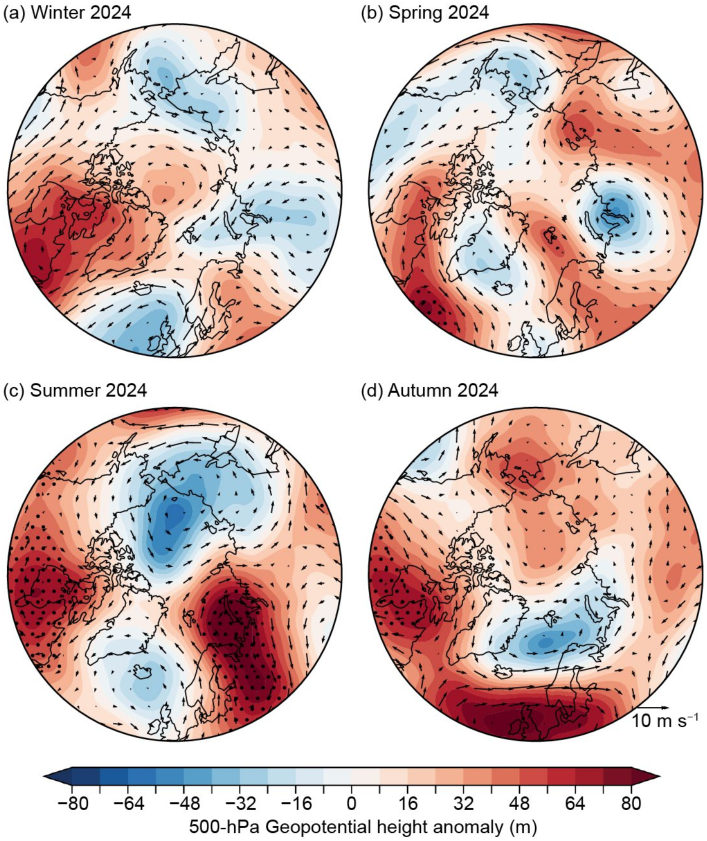

Fig. 5.3. 50-hPa geopotential height (m; shading) and 200-hPa wind (m s^{-1}; vectors) anomalies for (a) winter, (b) spring, (c) summer, and (d) autumn. Anomalies are calculated relative to the 1991–2020 climatology. Stippling indicates that the anomaly exceeds ±2 standard deviations of the 1991–2020 climate. (Data source: ERA5 [Hersbach et al. 2020].)

Autumn saw developing moderate high pressure over the North Atlantic, with anomalously strong upper-level westerly wind flow from southern Greenland to southern Scandinavia and continued strong blocking over the Hudson Bay (Fig. 5.3d).

c. Surface air temperature

—T. J. Ballinger, A. Crawford, M. C. Serreze, S. Bigalke, J. E. Walsh, B. Brettschneider, R. L. Thoman, U. S. Bhatt, E. Hanna, H. Motrøen Gjelten, S-J. Kim, J. E. Overland, and M. Wang

1. OVERVIEW

Widespread warming surface (i.e., two-meter) air and upper ocean temperatures (section 5e) characterize the changing Arctic (60°N–90°N) environment. Northern high-latitude surface air temperature changes continue to exceed global (90°S–90°N) scale changes, a phenomenon termed Arctic Amplification. After accounting for natural variability, studies have estimated that the Arctic is warming approximately three times faster than the global mean based on observational data and climate model simulations since 1980 (Sweeney et al. 2023; Zhou et al. 2024). Pervasive warming and an enhanced hydrological cycle, associated with increased precipitation (section 5d), represent key controls of Arctic environmental changes (Box et al. 2019). Daily maximum temperature extremes are both increasing and occurring more often (Polyakov et al. 2024), resulting in a surge of unprecedented extreme Arctic weather events in the last three years (Overland 2024). In this section, we place 2024 Arctic air temperatures in historical perspective and discuss notable seasonal anomaly patterns that occurred during 2024. Annual air temperatures follow the calendar year, while seasons are defined as winter (January–March), spring (April–June), summer (July–September), and autumn (October–December).

2. HISTORICAL CONTEXT TO 2024 ANNUAL AND SEASONAL TEMPERATURES

Annual Arctic and global surface air temperature anomalies from NASA's GISTEMP version 4 dataset are shown in Fig. 5.5a. During 2024, the Arctic had its second-warmest year over the period since 1900, with temperature anomalies 1.27°C above the 1991–2020 mean. This dataset indicates that 2024 was the warmest year on record globally since at least 1900; however, the relative magnitude of Arctic temperature anomalies continues to be larger. This is evidenced by air temperature warming of 2.26°C in the Arctic versus 1.26°C globally during the past 125 years (Fig. 5.5a). The year 2024 also marks the 11th consecutive year in which Arctic regional temperature departures exceeded those of Earth as a whole. Another noticeable feature of this dataset is that this past decade (2015–24) has been the Arctic's warmest, and has been characterized by several new annual and seasonal temperature records.

Arctic temperature anomalies were also comparatively higher than the global average in each season of 2024 (Figs. 5.5b–d). This is striking given that seasonal global temperature records were also set during winter and spring 2024. Seasonal temperature departures in 2024 from the 1991–2020 means were some of the highest in the Arctic since 1900, with winter at 1.14°C (sixth warmest), spring at 0.82°C (sixth warmest), and summer at 0.83°C (third warmest). Most notably, Autumn 2024 observed its highest temperatures on record at 2.28°C above the 1991–2020 mean, roughly 0.25°C higher than the next warmest autumn in 2020.

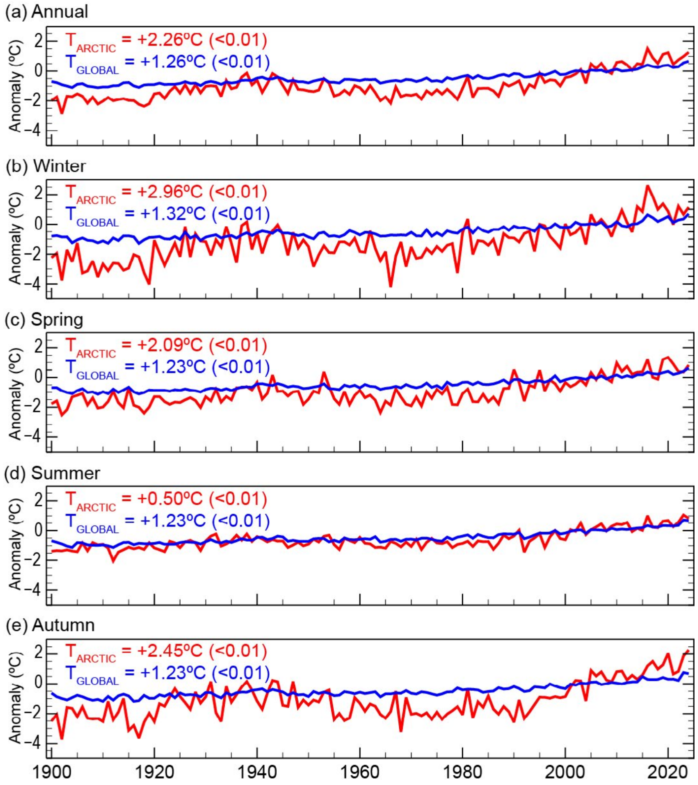

Fig. 5.5. Time series of (a) annual, (b) winter, (c) spring, (d) summer, and (e) autumn surface air temperature anomalies (°C) for 1900–2024 relative to the 1991–2020 mean and averaged across Arctic (60°N–90°N; red) and Global (90°S–90°N; blue) land and ocean areas. Annual time series in (a) reflect the Jan–Dec average. The total arctic (T_{ARCTIC}) and total global (T_{GLOBAL}) air temperature change during the full period of record, defined as the linear least-squares regression trend multiplied by the 125-year period, is shown in each panel along with the respective statistical significance (p-value) of the trends. (Data source: NASA GISTEMPv4 data obtained from the NASA Goddard Institute for Space Studies.)

The annual and seasonal air temperature anomalies display Arctic Amplification signatures (Fig. 5.5). A multitude of mechanisms and feedbacks drive Arctic Amplification at different times of the year. Meridional atmospheric circulation patterns can enhance heat and moisture transport into the Arctic and lead to more year-round warm extremes, whereas albedo feedbacks involving the amount, quality, and duration of snow and ice cover are constrained by sunlight that is prevalent in the warm season and absent at the highest northern latitudes during winter months (Cohen et al. 2020). During autumn and winter, when Arctic Amplification is strongest (Figs. 5.5b,e), the accumulation of heat in the Arctic Ocean is released to the overlying atmosphere, driving higher air temperatures (Taylor et al. 2022). Patterns of seasonal air temperature anomalies align with some of these processes that influence Arctic Amplification.

3. SEASONAL AIR TEMPERATURE ANOMALY PATTERNS IN 2024

Seasonal air temperature anomaly patterns from ERA5 reanalysis are shown in Fig. 5.6. Stippled areas indicate record seasonal warmth since 1950. Winter 2024 saw positive anomalies over the central Arctic Ocean (+3°C to +4°C) with smaller magnitude anomalies generally found over Arctic lands (Fig. 5.6a). Exceptions include the North Slope of Alaska, northern Baffin Island, northern Quebec, and Severnaya Zemlya, where the largest wintertime positive anomalies (+5°C to +6°C) were found. The latter two areas were associated with negative pressure anomalies to the west (Fig. 5.7a) that enhanced southerly winds and warm air advection. The largest cold anomalies were located over the Kamchatka Peninsula, including the Sea of Okhotsk, and the North Sea and Norwegian Sea of the Atlantic Arctic.

Similar to the preceding winter, spring 2024 featured positive anomalies of +2°C to +4°C over northern Canada and eastern Siberia (Fig. 5.5b). Record warmth is found within these areas, including over the eastern half of Hudson Bay, which also experienced record-early

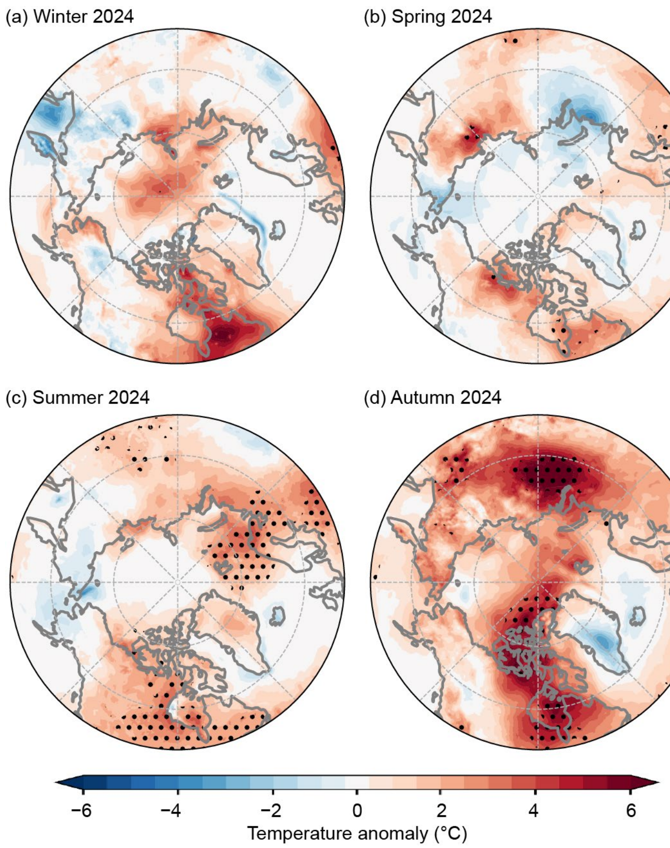

Fig. 5.6. Seasonal surface air temperature anomalies (°C) in 2024 for (a) winter, (b) spring, (c) summer, and (d) autumn. Temperature anomalies are shown relative to their 1991–2020 means. Stippled areas indicate record-high seasonal temperatures since 1950. (Data source: ERA5 air temperature data obtained from the Copernicus Climate Change Service.)

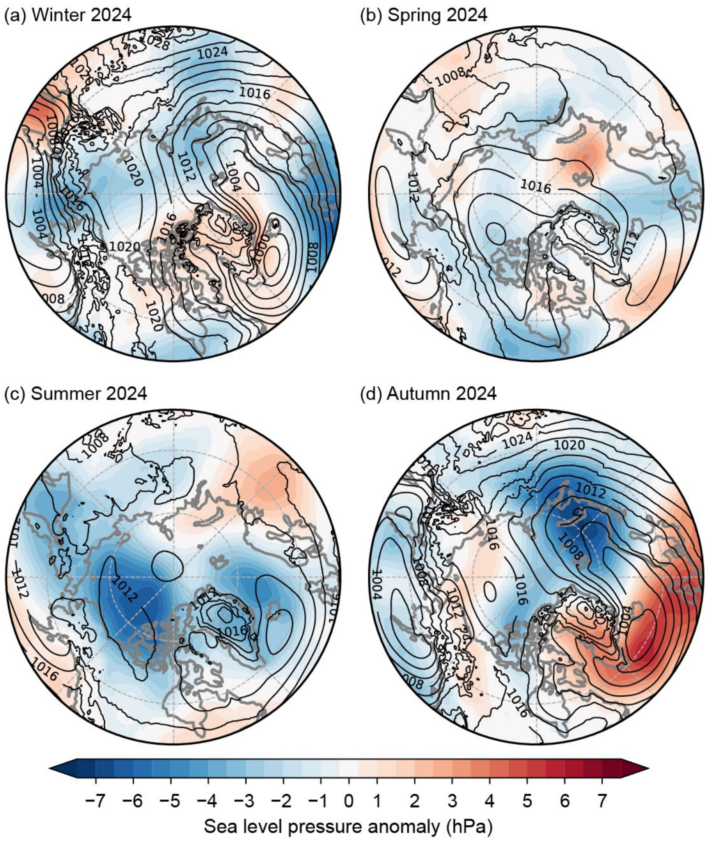

Fig. 5.7. Seasonal sea level pressure (SLP) anomalies (shading) and absolute values (isobars; both in hPa) in 2024 for (a) winter, (b) spring, (c) summer, and (d) autumn. SLP anomalies are shown relative to their 1991–2020 means. (Data source: ERA5 SLP data obtained from the Copernicus Climate Change Service.)

sea ice retreat. Small negative temperature anomalies extended offshore from the northeastern and northwestern Russian coastlines. However, unlike winter 2024, air temperatures over the Arctic Ocean during spring were average to slightly below average, linked to a relatively weak sea-level pressure (SLP) anomaly pattern over the region (Fig. 5.6b).

Continued warmth across portions of northern Canada and northern Eurasia characterized summer 2024. Record-high air temperatures since 1950 were found in Nunavut, northern portions of Manitoba, Ontario, and Quebec, and across much of southern Hudson Bay where seasonal departures were 2°C–3°C above the 1991–2020 mean (Fig. 5.6c). Areas with record temperature anomalies were also found in the eastern Arctic, extending from northern Scandinavia and across the Norwegian Sea and Barents Sea to the northern Svalbard coast. A few areas, including the western Chukchi Sea, central Bering Sea, and adjacent lands, were marked by negative temperature anomalies associated with an extensive area of lower-than-normal SLP across the western Arctic (Fig. 5.7c).

As mentioned in the previous section, a warm summer was followed by a record-warm autumn in 2024. Except for southern Greenland, Iceland, and the Chukchi Sea, most of the Arctic saw positive air temperature anomalies (Fig. 5.6d). Record spring and summer warmth continued into autumn for northern Ontario and Quebec, as well as Hudson Bay, where the record-early sea ice retreat resulted in exceptional ocean heat uptake throughout summer. This spatial pattern of warm extremes extended northward across the Canadian Archipelago and Lincoln Sea (6°C above normal). A record anomaly temperature pattern of similar magnitude was also found east of the Ural Mountains in northwestern Russia, which was supported by anomalous low pressure, suggestive of an active storm track and warm air masses frequently traversing the region (Fig. 5.7d).

Sidebar 5.1: **North American August heat**

—R. LADER AND R. L. THOMAN

Record Heat

A major heat event impacted northwest North America in early August 2024 from northeast Alaska (AK) across northern Yukon Territory (YT) and into the western Northwest Territories (NT). This same region also experienced above-normal temperatures in summer 2023 and, for parts of northwest Canada, this was the second consecutive summer with record-high temperatures. The August heat event was driven by larger-scale meridional winds enhanced through adiabatic warming during multiple mountain range crossings.

All-time record and August record-high temperatures are listed in Table SB5.1 for climate stations with at least 40 years of observations. The all-time records are particularly notable in the high latitudes because of rapidly declining solar radiation at this time of year. Maximum hourly near-surface air temperatures for the week of 4–10 August from ERA5 (Hersbach et al. 2020) indicate a broad area of temperatures of 33.0°C or higher along the Mackenzie River in NT (Fig. SB5.1a).

In addition to record maximum temperatures, this event led to extreme high minimum temperatures and precipitation patterns that exhibited clear topographical influences. An all-time record-high daily minimum temperature of 21.7°C was recorded at Delta Junction, AK (64°00′N, 145°43′W, 389 m a.s.l.) on 6 August. The highest daily minimum near-surface air temperatures from ERA5 show areas in excess of 18.0°C in interior Alaska and along the Beaufort Sea coast in Canada (Fig. SB5.1b). For reference, the average daily minimum temperature at Inuvik, NT, for this time of year is around 7°C. Total accumulated precipitation during this event was low, particularly in the Yukon Flats region of AK, and across north-central NT where less than 5 mm fell (Fig. SB5.1c). The influence of terrain height is evident as the southern coastal mountains of AK, which were inundated with over 50 mm of precipitation, effectively blocked moisture from advecting farther inland (Fig. SB5.1d). Moreover, downsloping air flow from the Alaska Range likely contributed to the local temperature maxima seen in interior Alaska, and similarly, the Yukon Ranges in NT.

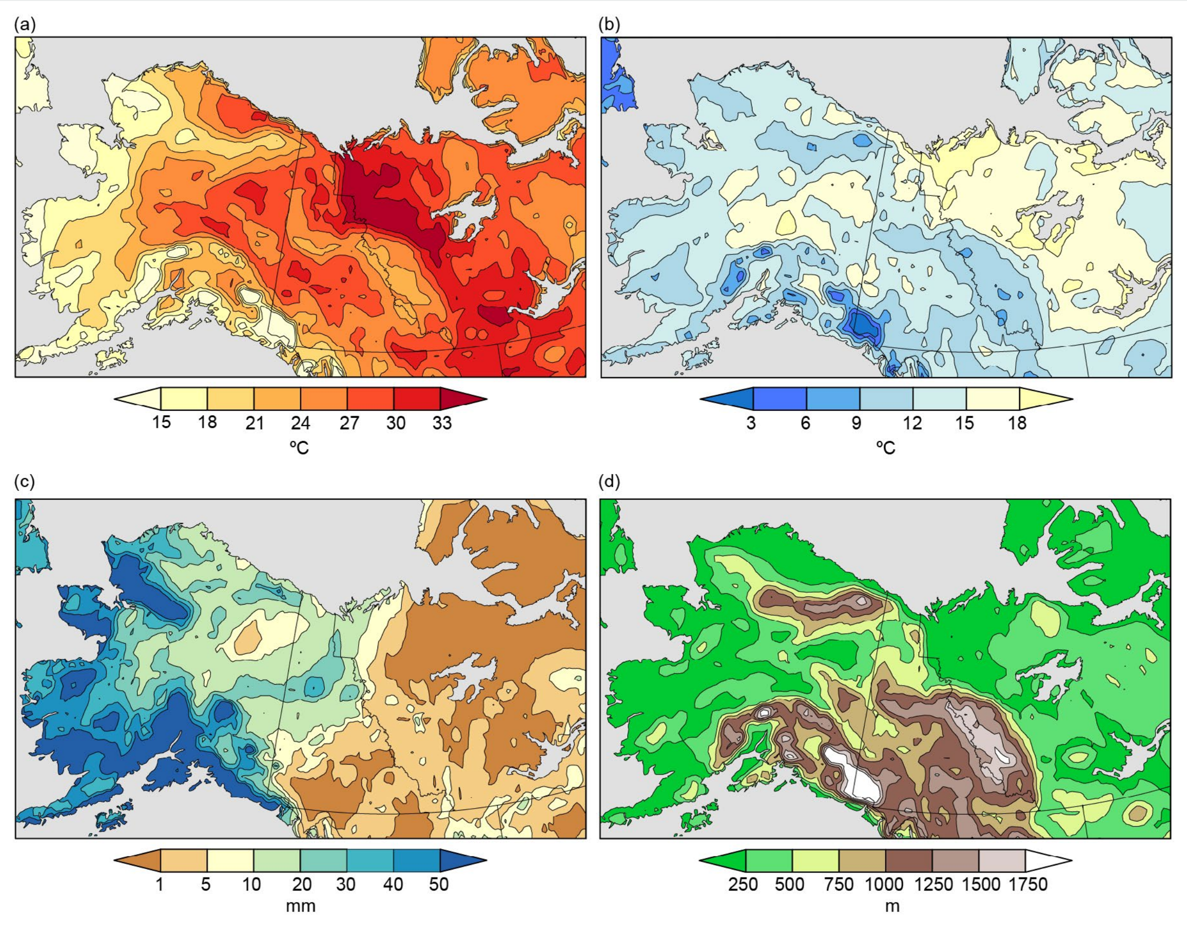

Fig. SB5.1. (a) Maximum hourly near-surface air temperature (°C), (b) maximum daily minimum near-surface air temperature (°C), and (c) total precipitation (mm) for 4–10 August 2024. Terrain height (m) is shown in (d). (Data source: ERA5.)

Large-Scale Anomalies

A mid-tropospheric ridge developed across eastern AK and YT at the beginning of the heat event, before strengthening and propagating to the east over central NT. The 500-hPa height anomalies from the National Centers for Environmental Prediction (NCEP)/National Center for Atmospheric Research (NCAR) Reanalysis version 1 (R1; Kalnay et al. 1996) exceeded 160 m over northern YT on 5 August, with low pressure farther west near the Gulf of Anadyr (Fig. SB5.2a). By 7 August, the gradient between these two features had increased as the area of low pressure moved into the Bering Sea, and the high pressure ridge strengthened across western NT. Anomalous 500-hPa heights in excess of 200 m extended from the Mackenzie River eastward (Fig. SB5.2b). By 9 August, the gradient had weakened, and the low pressure in the Bering Sea began influencing all of AK with negative 500-hPa height anomalies extending eastward. The highest departures from normal, still in excess of 200 m, covered much of the central and eastern NT (Fig. SB5.2c).

The influence of the mid-tropospheric height pattern was reflected in the near-surface air temperatures. As the 500-hPa ridge developed on 5 August, temperature anomalies of +4°C to +6°C were seen over the North Slope of AK and across the Mackenzie Delta (Fig. SB5.2d). Notably, negative air temperature anomalies were shown over south-coastal Alaska as southerly flow advected moist, cool air inland. By 7 August, the magnitude of this heat event was apparent relative to the circumpolar region, with temperature anomalies in excess of +10°C across a broad swath of far northwestern North America (Fig. SB5.2e). Negative temperature anomalies remained in southern Alaska, while downsloping winds warmed and dried the air farther north. By 9 August, the heat event reached its peak across NT, while negative temperature anomalies were seen across AK as low pressure from the west and a weakening pressure gradient no longer supported extreme heat (Fig. SB5.2f).

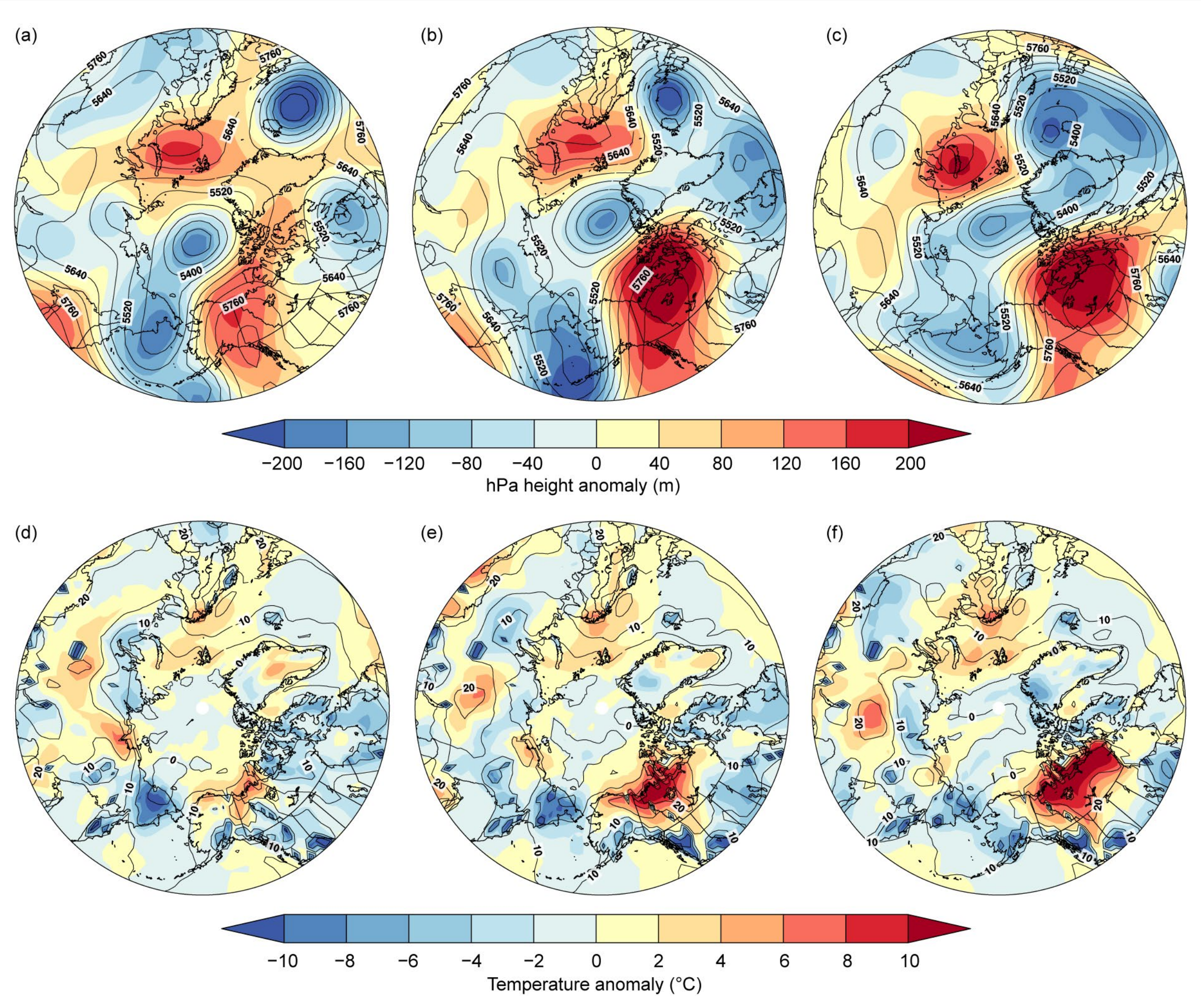

Fig. SB5.2. 500-hPa heights (contours) and anomalies (shading) on (a) 5 Aug, (b) 7 Aug, and (c) 9 Aug (m) and near-surface air temperatures (contours) and anomalies (shading) on (d) 5 Aug, (e) 7 Aug, and (f) 9 Aug (°C) during the 2024 heat event. Anomalies are relative to the 1991–2020 base period. (Data source: National Centers for Environmental Prediction (NCEP)/National Center for Atmospheric Research (NCAR) Reanalysis 1)

Discussion

The 2024 August heat marks another record-setting event to impact high-latitude North America in recent years. In 2023, Canada observed its warmest summer and autumn seasons on record, and both YT and NT recorded their warmest annual temperatures (Cheng et al. 2024). Some of the new 2024 records listed in Table SB5.1 broke records set in 2023. The hot, dry conditions supported wildfire activity across NT, where an additional 585,000 hectares burned during 1–11 August, contributing to NT's third-highest annual area burned on record; YT, which was not as hot and received more precipitation, saw minimal increases in wildfire activity (<10,000 hectares of new area burned; CIFFC 2025). This follows a record-breaking wildfire year across Canada in 2023 when approximately 15 million hectares burned, leading to community evacuations and health impacts from smoke inhalation (Jain et al. 2024). Wildfire is also increasing across permafrost regions. In 2024, permafrost temperatures across Alaska were the second highest of record, and 335 Tg of direct fire carbon emissions were observed throughout the pan-Arctic (Natali et al. 2024). These events show how compounding hazards (AghaKouchak et al. 2020) such as heat and wildfire are leading to greater impacts.

Methods and Data

Station observations are available for AK from the NOAA Applied Climate Information System online tool (https://xmacis.rcc-acis.org), and from Environment and Climate Change Canada for YT and NT (https://climate.weather.gc.ca). ERA5 data are provided by the Copernicus Climate Change Service Climate Data Store (https://doi.org/10.24381/cds.adbb2d47). NCEP/NCAR Reanalysis 1 data are provided by the NOAA Physical Sciences Laboratory (https://psl.noaa.gov). Canada wildfire information is available from the Canadian Interagency Forest Fire Centre (https://ciffc.net/).

Table SB5.1. Locations setting monthly or annual record-high temperatures during August 2024. Data sources given in the Methods and Data section.

Annual Record Temperatures

Location	Latitude	Longitude	Elevation (m)	Maximum Temperature (°C)	Date of Maximum
Deadhorse, Alaska (AK)	70°12′N	148°28′W	17	31.7	6 Aug
Kuparuk, AK	70°20′N	149°37′W	20	31.1	6 Aug
Fort McPherson, Northwest Territories (NT)	67°24′N	134°51′W	35	35.1	8 Aug
Inuvik, NT	68°19′N	133°31′W	103	34.8	7 Aug
Paulatuk, NT	69°21′N	124°04′W	6	31.0	8 Aug

August Record Temperatures

Location	Latitude	Longitude	Elevation (m)	Maximum Temperature (°C)	Date of Maximum
Tuktoyaktuk, NT	69°26′N	133°01′W	5	29.9	7 Aug
Fort Good Hope, NT	66°14′N	128°38′W	82	37.0	9 Aug
Norman Wells, NT	65°17′N	126°45′W	94	36.8	9 Aug

d. Precipitation

—M. C. Serreze, S. Bigalke, R. Lader, A. Crawford, and T. J. Ballinger

1. INTRODUCTION

Obtaining accurate measurements of Arctic precipitation to assess anomalies and change is challenged by the sparse observation network—notably over the Arctic Ocean—and observation errors due to factors such as gauge undercatch of solid precipitation (Serreze et al. 2003). Studies of Arctic precipitation have increasingly relied on output from atmospheric reanalysis projects, the most recent of these being ERA5 (Hersbach et al. 2020), which performs slightly better than other reanalyses at matching observed precipitation (Barrett et al. 2020; Loeb et al. 2022). In this section, ERA5 is used along with the gauge-based GPCC version 2022 dataset (land-only measurements; Becker et al. 2013; Schneider et al. 2022) to assess 2024 precipitation anomalies and trends. The Arctic is taken as the region poleward of 60°N. Winter, spring, summer, and autumn are defined as January–March, April–June, July–September, and October–December. A key finding is that, for the Arctic as a whole, annual precipitation based on ERA5 for 2024 was the third highest of the 1950–2024 record, consistent with the observed pattern that Arctic precipitation is increasing.

2. SUMMARY

Pan-Arctic annual precipitation for 2024 was 105% of the 1991–2020 average based on ERA5. Percent anomalies by season were 102% for winter, 101% for spring, 108% for summer, and 109% for autumn. Expressed as ranks, pan-Arctic annual precipitation for 2024 from ERA5 was the third highest over the 1950–2024 record. Corresponding ranks for winter, spring, summer, and autumn and are 17th, 20th, 1st, and 4th, respectively.

3. REGIONAL ANOMALIES

Figure 5.8 shows seasonal precipitation totals derived from ERA5 during 2024, expressed as anomalies with respect to 1991–2020 means. Prominent features of 2024 were: 1) strong negative anomalies in winter over the Alaskan Panhandle; 2) generally small anomalies during spring that were positive over the Barents Sea and part of Canada and mostly negative over Eurasia; 3) summer dryness over large parts of the Eurasian and North American continents but with wet conditions over central and northern Alaska and Scandinavia; and 4) wet conditions in autumn over the Barents Sea and coastal Norway and negative anomalies off the southeast coast of Greenland.

Precipitation along the Alaskan Panhandle is strongly driven by orographic uplift. Especially dry winter conditions here point to few cases of upslope winds. While negative summer anomalies dominated northern Canada, those over northern Eurasia were primarily found over the western side of the continent. Nevertheless, averaged over the Arctic region as a whole, summer precipitation ended up as the wettest in the record (see discussion below), in considerable part because of the positive anomalies over Alaska, the Barents Sea region, and the Canadian Arctic

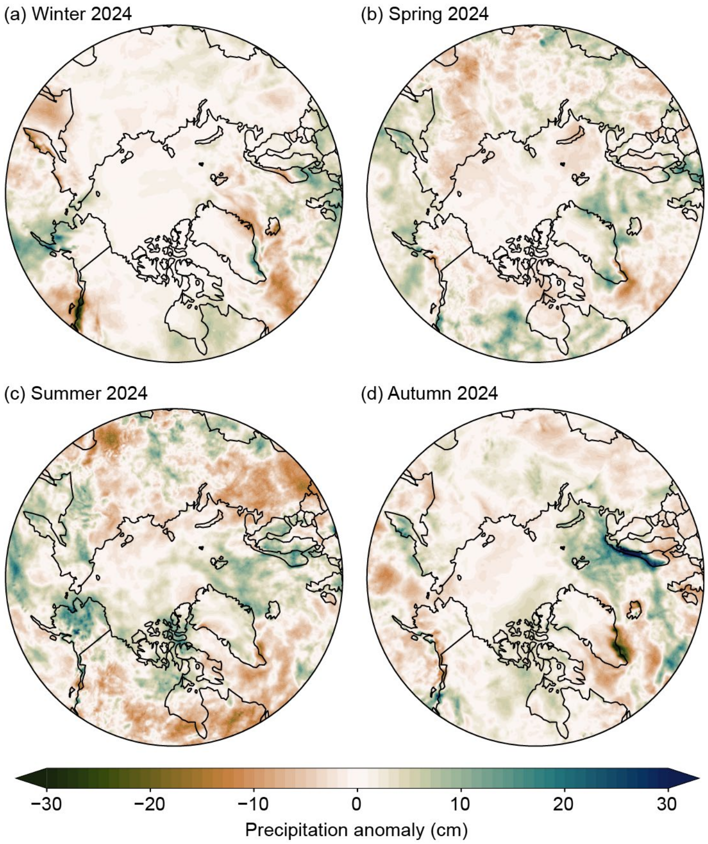

Fig. 5.8. Seasonal precipitation anomalies (1991–2020 baseline) for 2024 for (a) winter, (b) spring, (c) summer, and (d) autumn. Green shades denote above-normal precipitation; brown shades denote below-normal precipitation. (Data source: ERA5.)

Archipelago. According to ERA5, some of the high summer precipitation over Alaska was associated with convective activity (thunderstorms). Based on analysis of the cyclone detection and tracking algorithm developed by Crawford and Serreze (2016) and applied to ERA5 sea level pressure data, strong positive anomalies in the Barents Sea in autumn relate to an uptick in extratropical cyclone activity (15.3% more frequent than the 1991–2020 mean). The coast of Norway is another region where orographic uplift is important; the strongly positive autumn anomalies there point to strong moist upslope winds associated with a series of especially strong storms (averaging 14.0% stronger than the 1991–2020 mean based on the cyclone algorithm). The southeast coast of Greenland is known for exceptionally high precipitation due to orographic uplift, yet the negative anomalies here point to fewer upslope events in 2024. Anomalies from the Barents Sea, Norway, and Greenland were all connected to a general northeast shift in storm tracks.

4. HEAVY PRECIPITATION EVENTS

For any given year, there is a statistical expectation of regionally heavy precipitation events that can approach or exceed previous records, even in a stable climate. Figure 5.9 plots heavy precipitation events in 2024 by season in terms of ranks of the maximum five-day precipitation events (Rx5) in each season (relative to the 1950–2024 period). Generally, heavy precipitation events are scattered across the Arctic. A notable feature is the band of heavy events in winter stretching from south of the Aleutians northward across western Alaska into the East Siberian Sea, which is aligned with warmer-than-average conditions (section 5c; Fig. 5.9a). There were also some heavy events over the Canadian Arctic Archipelago and Lincoln Sea in summer.

5. HISTORICAL PERSPECTIVE

Climate models project increased Arctic precipitation and more frequent heavy precipitation events as the climate warms, as well as an increase in the proportion of precipitation falling as rain. There is observational evidence of a transition to liquid precipitation in the warmer parts of the Arctic (Box et al. 2021), although the coldest areas are expected to see snowfall increases through the twenty-first century (McCrystall et al. 2021; Bigalke and Walsh 2022). Past studies have revealed large spatial variability in trends (Yu and Zhong 2021). However, as discussed in the arctic precipitation section of the 2023 *BAMS State of the Climate* report (Serreze et al. 2024) and presented here with updates, pan-Arctic precipitation assessed since 1950 now has detectable upward trends in all seasons, as well as in the annual mean.

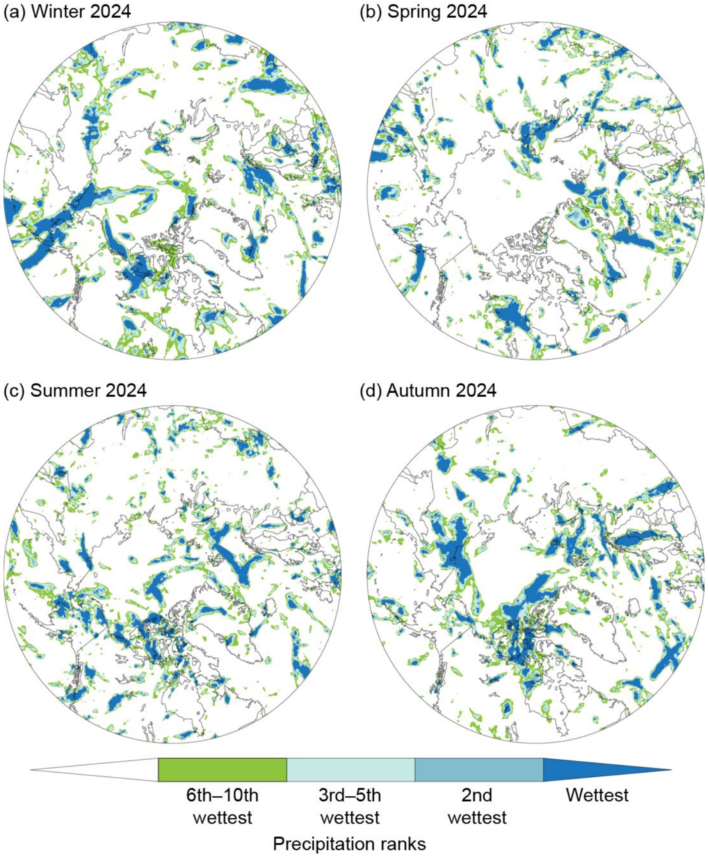

Fig. 5.9. Ranks of maximum five-day precipitation for 2024 for (a) winter, (b) spring, (c) summer, and (d) autumn. (Data source: ERA5, 1950–present.)

In Fig. 5.10, the Arctic precipitation time series from ERA5 (as a percentage of 1991–2020 averages for the region poleward of 60°N) is plotted along with the corresponding time series from the station-based GPCC dataset for the period 1950–2024. The GPCC dataset is for land only, while ERA5 covers ocean areas as well as land. While the percent anomaly time series are generally similar, there are substantial differences for individual years due to the absence of coverage over the Arctic Ocean in GPCC and inherent uncertainties in each data source. Nevertheless, the time series agree with respect to a positive annual trend and record-high precipitation for summer 2024.

Based on ERA5, the trend in annual mean precipitation stands at +0.68 cm decade^{-1}, or a 14.1% percent change since 1950. Corresponding seasonal changes are +0.23 cm decade^{-1} for winter, +0.09 cm decade^{-1} for spring, +0.13 cm decade^{-1} for summer, and +0.23 cm decade^{-1} for autumn.

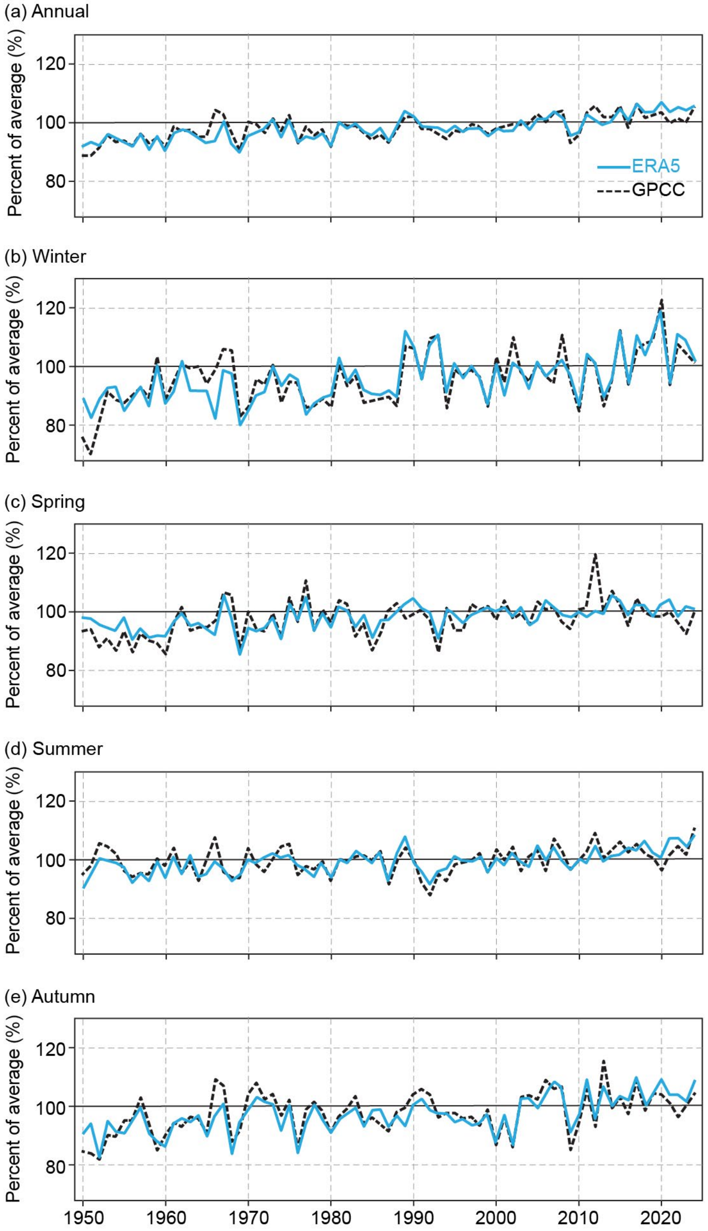

Fig. 5.10. Time series of Arctic (60°N–90°N) precipitation from 1950 through 2024 expressed as a percentage of the 1991–2020 average (shown by the horizontal black lines at 100%). Results are from ERA5 (blue lines) and GPCC 1.0° data (black lines). GPCC values are for land only; ERA5 values are for land plus ocean.

e. Sea surface temperature

—M.-L. Timmermans and Z. Labe

Arctic Ocean sea surface temperatures (SSTs) in the summer are primarily influenced by the amount of incoming solar radiation absorbed by the sea surface and by the flow of warm waters into the Arctic from the North Atlantic and North Pacific Oceans. Solar warming of the Arctic Ocean surface is influenced by the sea ice distribution (with greater warming occurring in ice-free regions), cloud cover, and upper-ocean stratification. Inflows of relatively warm Arctic river waters can provide an additional heat source in coastal regions.

Arctic SST is an essential indicator of the strength of the ice–albedo feedback cycle in any given summer sea ice melt season. As the brighter sea ice cover decreases, more incoming solar radiation is absorbed by the darker ocean surface and, in turn, the warmer ocean melts more sea ice. Marine ecosystems are also influenced by SSTs, which affect the timing and development of primary production cycles, available habitat, and other factors, such as the occurrence of harmful algal blooms. In addition, higher SSTs are associated with delayed autumn sea ice freeze-up and increased ocean heat storage throughout the year.

The SST data presented here are from the 0.25° × 0.25° NOAA OISST version 2.1 product (Reynolds et al. 2002, 2007; Huang et al. 2021). The period of our analysis spans June 1982 through September 2024, with 1991–2020 used as the climatological reference period. Here, we focus most closely on August 2024 mean SSTs in context with the climatological record. August mean SSTs provide the most appropriate representation of Arctic Ocean summer SSTs because sea ice extent is near a seasonal low at this time of year, and there is not yet the influence of surface cooling and subsequent sea ice growth that typically takes place in the latter half of September (Timmermans and Labe 2024).

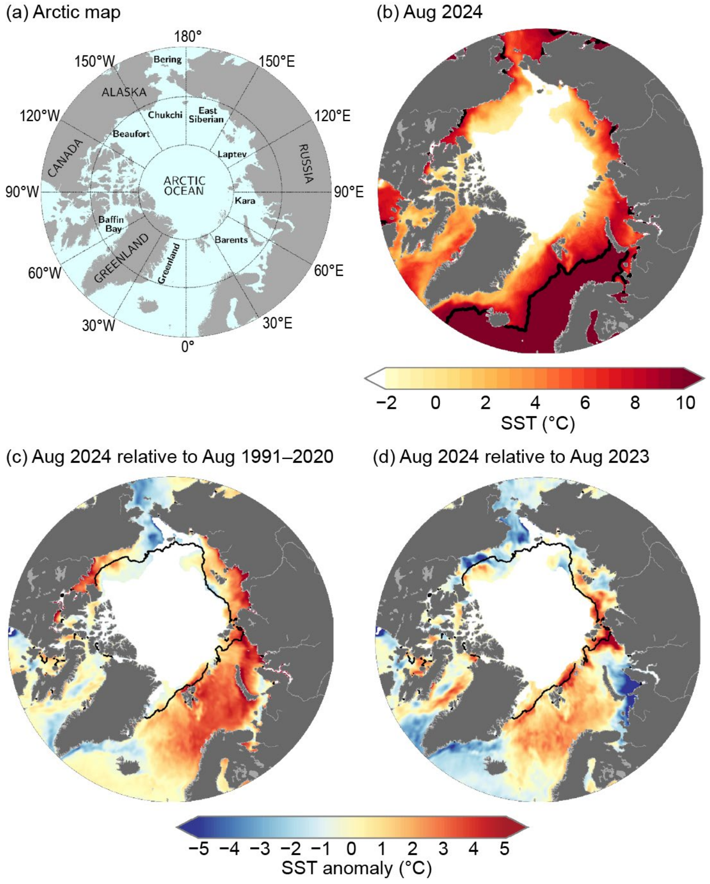

Fig. 5.11. (a) Arctic Ocean map showing relevant marginal sea locations and geographic features. (b) Mean sea surface temperature (SST; °C) in Aug 2024. Black contours indicate the 10°C-SST isotherm. (c) SST anomalies (°C) in Aug 2024 relative to the Aug 1991–2020 mean. (d) Difference between Aug 2024 SSTs and Aug 2023 SSTs (negative values indicate where 2024 was cooler). White shading in all panels is the Aug 2024 mean sea ice extent. Black lines in (c) and (d) indicate the Aug 1991–2020 median ice edge. Sea ice concentration data are the NOAA National Snow and Ice Data Center Climate Data Record of Passive Microwave Sea Ice Concentration, version 2 and version 4 (Peng et al. 2013; Meier et al. 2021a,b).

August 2024 mean SSTs were as high as ~12°C in the southern Barents Sea and reached values as high as ~7°C in other Arctic basin marginal regions (Figs. 5.11a,b). August 2024 mean SSTs were anomalously high compared to the 1991–2020 August mean (around 1°C–4°C higher) in the Barents, Kara, Laptev and southern Beaufort Seas, and anomalously low (around 0.5°C–4.0°C below the 1991–2020 mean; Fig. 5.11c) in the East Siberian, Chukchi, and northern Beaufort Seas. The cold SSTs in the Arctic Pacific sector also extended through the Bering Sea (Fig. 5.12). The general pattern of August 2024 SSTs is consistent with regional patterns of anomalously warm and cold surface-air temperatures in summer 2024 (section 5c). Regional SST variations differ significantly from year to year. For example, there were considerably higher SSTs in the northern Barents Sea in August 2024 compared to August 2023, with differences of up to 2°C, and mostly lower 2024 SSTs in the Kara and southern Beaufort Seas (Fig. 5.11d).

Below-normal August 2024 SSTs in the Chukchi Sea were also observed in June, July, and September, as well as in the eastern sector of the Bering Sea (Fig. 5.12). This is consistent with relatively cold spring and summer 2024 surface air temperatures in the region (section 5c) and persistent areas of above-normal sea ice extent (Fig. 5.11c). Above-normal August 2024 SSTs in the Kara and Laptev Seas were also observed in July (Figs. 5.12b,c) as sea ice began to retreat from those regions, suggesting that the ice–albedo feedback was playing a role in ice retreat and SST warming. The transition from below-normal to above-normal August SSTs from June to August in the Barents Sea corresponded with the transition from anomalously cool surface air temperatures in spring to warm ones in summer (section 5c). A similar spatial pattern of SST anomalies persisted from August through the end of the melt season in September (Fig. 5.12d), although with generally reduced warm anomalies in the marginal seas, signifying cooling in the latter half of September.

The Arctic Ocean has experienced mean August SST warming trends from 1982 to 2024, with statistically significant (at the 95% confidence interval) linear warming trends in almost all regions (Fig. 5.13). Mean August SSTs for the entire region of the Arctic Ocean north of 65°N exhibit a linear warming trend of 0.03±0.01°C yr^{-1} (Fig. 5.14a). For context, both the North Pacific and North Atlantic (between 50°N and 65°N) show linear warming trends over this same period of 0.04±0.01°C yr^{-1}.

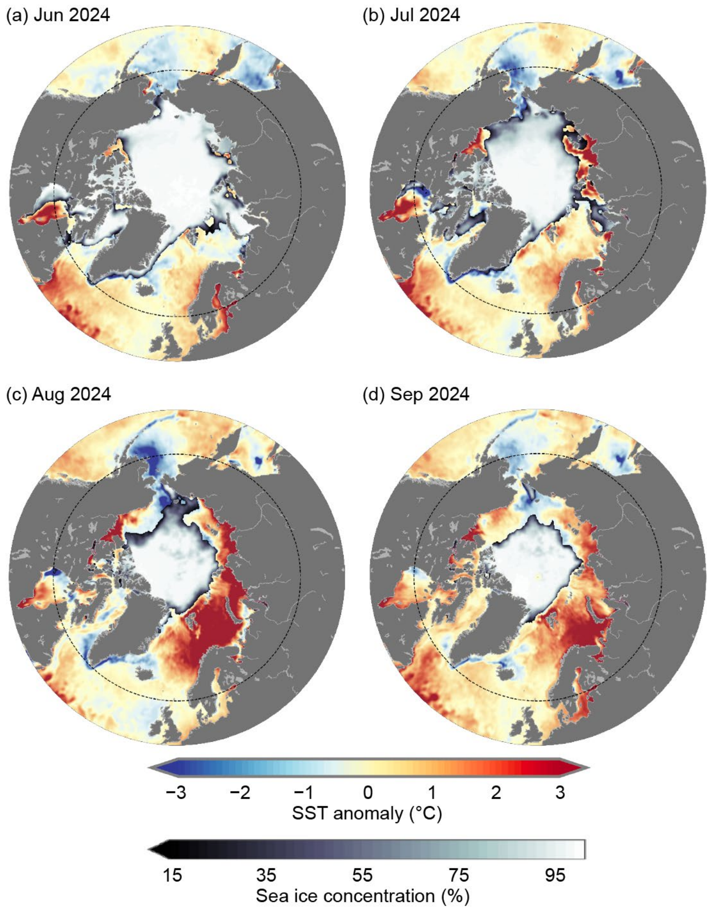

Fig. 5.12. Sea surface temperature (SST) anomalies (°C) for (a) Jun 2024, (b) Jul 2024, (c) Aug 2024, and (d) Sep 2024 relative to the 1991–2020 mean for the respective months. The mean sea ice concentration for the corresponding month is also shown. While sea ice extent is lowest in Sep, SSTs cool in the latter part of the month. The dashed circle indicates the latitudinal bound of the maps in Fig. 5.11. See Fig. 5.11 caption for sea ice dataset information.

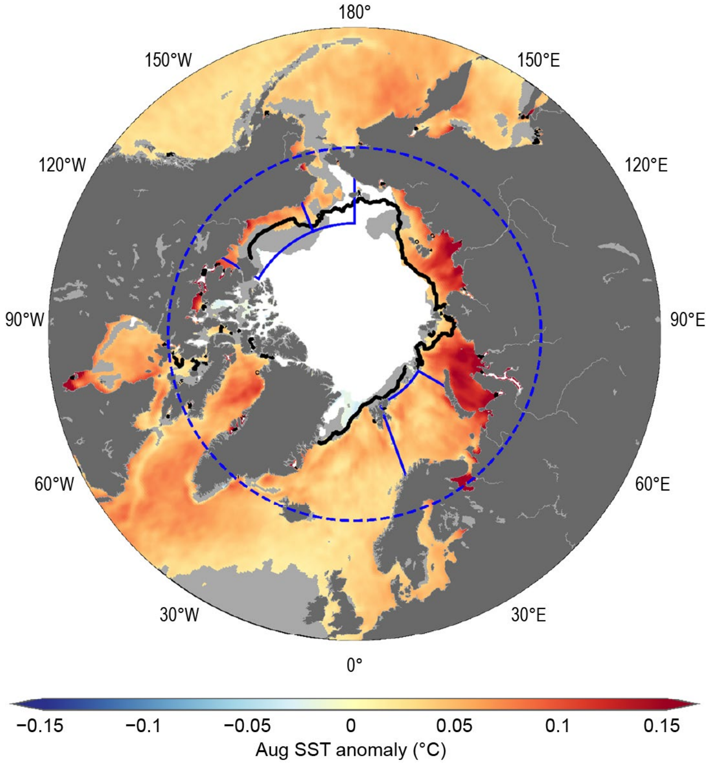

Fig. 5.13. Linear sea surface temperature (SST) trend (°C yr^{-1}) for Aug of each year from 1982 through 2024. The trend is only shown for values that are statistically significant at the 95% confidence interval; the region is shaded light gray otherwise. White shading is the Aug 2024 mean sea ice extent, and the black line indicates the Aug 1991–2020 median ice edge. The dashed blue circle marks 65°N (the Arctic Ocean region), and solid blue line boundaries delineate the Barents, Beaufort, and Chukchi Seas.

Regionally, the Kara and Laptev Seas show the strongest warming trends in the Arctic Ocean, with August SST linear trends in these seas of around 0.12°C yr^{-1} (Fig. 5.13). This is consistent with trends to earlier melt onset in these regions (section 5f). Statistically significant linear trends in August SST are also observed in the Barents Sea (0.06±0.02°C yr^{-1}), where August 2024 mean SSTs were the highest on record (Fig. 5.14b). On the other hand, there is no statistically significant trend in August SSTs in the Beaufort and Chukchi Seas (Figs. 5.14c,d), although the southernmost portion of the Beaufort Sea does show a statistically significant warming trend (Fig. 5.13). The Beaufort Sea shows considerable interannual variability in mean August SST values (Fig. 5.14c), while Chukchi Sea trends are notably influenced by anomalously cool SSTs in the region in recent years with record-low August 2024 mean SSTs (Fig. 5.14d).

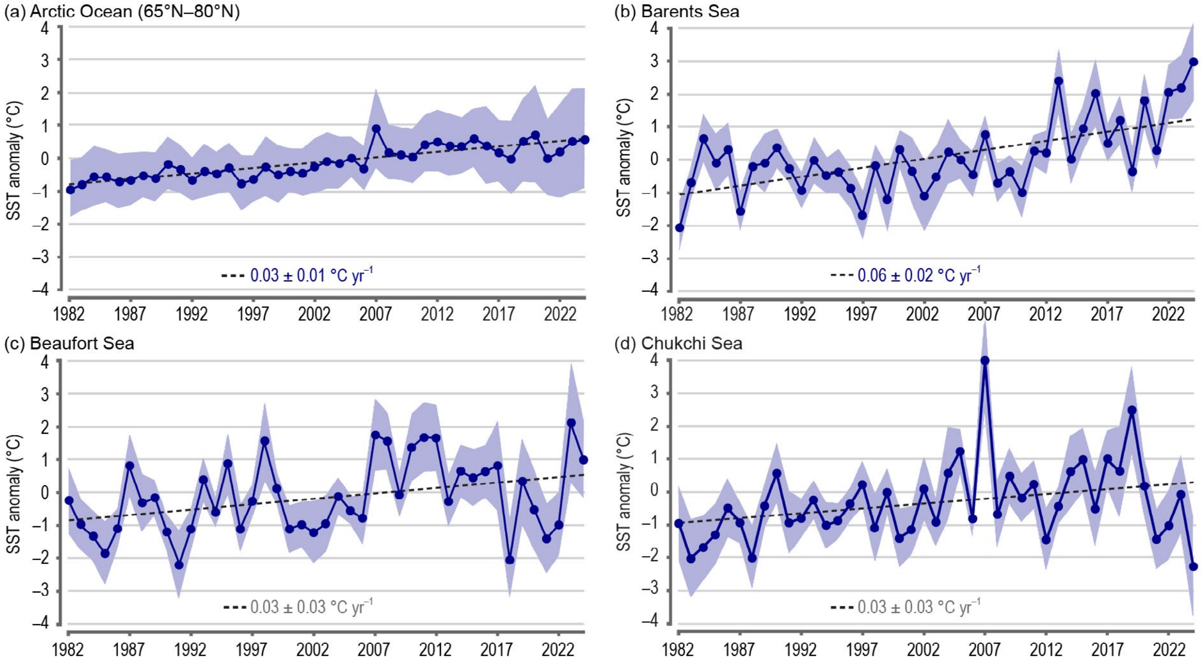

Fig. 5.14. Area-averaged SST anomalies (°C) for Aug of each year (1982–2024) relative to the 1991–2020 Aug mean for (a) the Arctic Ocean (65°N–80°N; indicated by the dashed blue circle in Fig. 5.13), (b) the Barents Sea, (c) the Beaufort Sea, and (d) the Chukchi Sea regions shown by blue boundaries in Fig. 5.13. The dotted lines show the linear SST anomaly trends over 1982–2024, and numbers in the legends indicate the trends in °C yr^{-1} (with 95% confidence intervals; trends that are not statistically significant are labeled in gray). Blue shading indicates ±1 standard deviation of the regional mean SST anomaly fields.

f. Sea ice

—W. N. Meier, A. Petty, S. Hendricks, D. Perovich, S. Farrell, M. Webster, D. Divine, S. Gerland, L. Kaleschke, R. Ricker, X. Tian-Kunze, and A. Bliss

Sea ice is the frozen interface between the ocean and atmosphere in the Arctic. It limits ocean–atmosphere exchanges of energy and moisture and plays a critical role in Arctic ecosystems and Earth's climate. The presence of sea ice affects human activities in the Arctic, including Indigenous hunting and transportation as well as marine navigation. Arctic September sea ice extent has declined 46% over 1979–2024, and 2024 sea ice conditions continued to illustrate the profound and ongoing changes in the region.

1. SEA ICE EXTENT

Arctic sea ice extent (defined as the total area covered by at least 15% ice concentration) in 2024 was generally on par with extents of the last 15 years, but much lower than those of all earlier decades within the observational record. For comparisons in this section, a climatological period of 1991–2020 is used. Extent during winter (January–March) 2024 was higher than in 2023 and fell within the lowest 10% of the climatological range. Extent values are from the National Snow and Ice Data Center's Sea Ice Index (Fetterer et al. 2017), one of several extent products (Ivanova et al. 2014; Lavergne et al. 2019) derived from satellite-borne passive microwave sensors operating since 1979. Extent was lower than average in the Barents Sea, Bering Sea, and the Gulf of St. Lawrence.

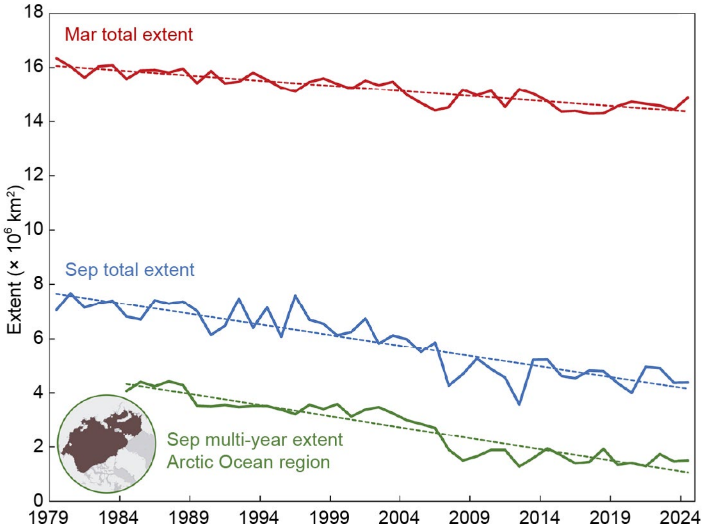

Fig. 5.15. Mar (red) and Sep (blue) total extent for 1979–2024; multi-year Sep extent (green) for 1984–2024 and linear trend lines (dashed lines). The Arctic Ocean region map is inset in the bottom left.

By March, the month with the most extensive coverage, the total sea ice extent of 14.87×10^6 km^2 was 0.16×10^6 km^2 (1.1%) lower than average and the 15th lowest March extent in the 46-year record. The March 2024 pan-Arctic extent continued the statistically significant downward trend of –2.5% decade^{-1} over the 1979–2024 record (Fig. 5.15). On a regional basis, March 2024 was characterized by near-average extent across most of the Arctic, with slightly lower-than-average extent in the Barents Sea and Gulf of St. Lawrence (Fig. 5.16a).

After March, the seasonal retreat of sea ice began. The 2024 and 2023 extents were similar during the spring and summer melt seasons (April–September), with extents at or just below the interdecile range during spring before dropping well below the lower interdecile after June. A notable feature of spring 2024 was a very early opening of the eastern Hudson Bay, resulting in record-low extent in the region from mid-May through June.

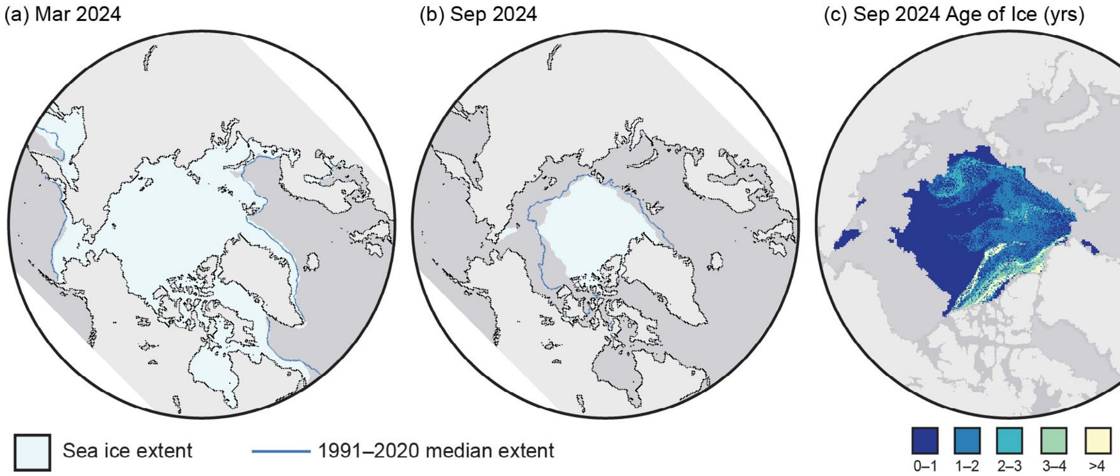

Fig. 5.16. Monthly average sea ice extent (light blue) for (a) Mar 2024 and (b) Sep 2024; the median extent for 1991–2020 is shown by the dark blue contour. (c) Sep 2024 sea ice age extent.

The Northern Sea Route along the northern Russian coast was relatively slow to open, with sea ice extending southward to the coast in the East Siberian Sea until late August. Afterward, an ice-free passage did open up, but a large remnant of ice between Wrangel Island and mainland Siberia survived through the melt season. The northern Northwest Passage route through the Canadian Archipelago reached a record-low sea ice extent in early October, briefly becoming virtually ice-free (Sidebar 5.2).

September, the month of the annual minimum sea ice extent, was characterized by below-average coverage in the Pacific sector with open water extending far northward from the coast in the Beaufort, Chukchi, and Siberian Seas (Fig. 5.16b). The September 2024 sea ice extent of 4.38 × 10^6 km^2 was 1.20 × 10^6 km^2 (21.6%) lower than the 1991–2020 average and the sixth-lowest September extent on record. The September trend from 1979 through 2024 is –13.9% $decade^{-1}$, and like all other months, is statistically significant. The 18 lowest September extents in the satellite record have all occurred in the last 18 years (2007–24). The 2024 freeze-up period (October–December) was slower than that of 2023 with much lower-than-average extent, particularly in Hudson Bay.

2. SEA ICE AGE, THICKNESS, AND VOLUME

Sea ice age is a rough proxy for thickness as multiyear ice (ice that survives at least one summer melt season) grows thicker over successive winters. Multiyear ice age based on Tschudi et al. (2019a,b) is presented here for the period 1984–2024 (Fig. 5.15). One week before the 2024 annual minimum extent, when the age values of the remaining sea ice are incremented by one year, the amount of multiyear ice remaining in the Arctic continued to be far lower than during the 1980s and 1990s (Fig. 5.16). Since 2012, the Arctic has been nearly devoid of the oldest ice (>4 years old); this continued in 2024 (Fig. 5.16c), with an end-of-summer old ice extent of 118,000 km^2 compared to ~1.5 × 10^6 km^2 in the 1980s. In the 41 years since ice-age records began in 1984, the Arctic has changed from a region dominated by multiyear sea ice to one where first-year sea ice prevails. A younger ice cover implies a thinner, less voluminous ice pack that is more sensitive to atmospheric and oceanic changes.

Sea ice drifts with winds and ocean currents while growing and melting thermodynamically. Ice divergence creates leads where, in freezing conditions, new ice forms while ice convergence leads to dynamic thickening. Sea ice thickness provides a record of the cumulative effect of dynamic and thermodynamic processes and thus is an important indicator of overall ice conditions. The European Space Administration's (ESA) CryoSat-2/Soil Moisture Ocean Salinity (SMOS) satellites have provided a record of seasonal (October–April) ice thickness and volume (Ricker et al. 2017; ESA 2023) since the 2010/11 winter. Since 2018, the NASA ICESat-2 satellite has also provided thickness estimates (Petty et al. 2020, 2023a,b). Some differences between these two products are seen in the monthly average winter Arctic thickness (Fig. 5.17a), but both products show monthly thicknesses from the 2023/24 winter similar to the mean of this short overlapping period (2018 onwards, see Fig. 5.17a). April

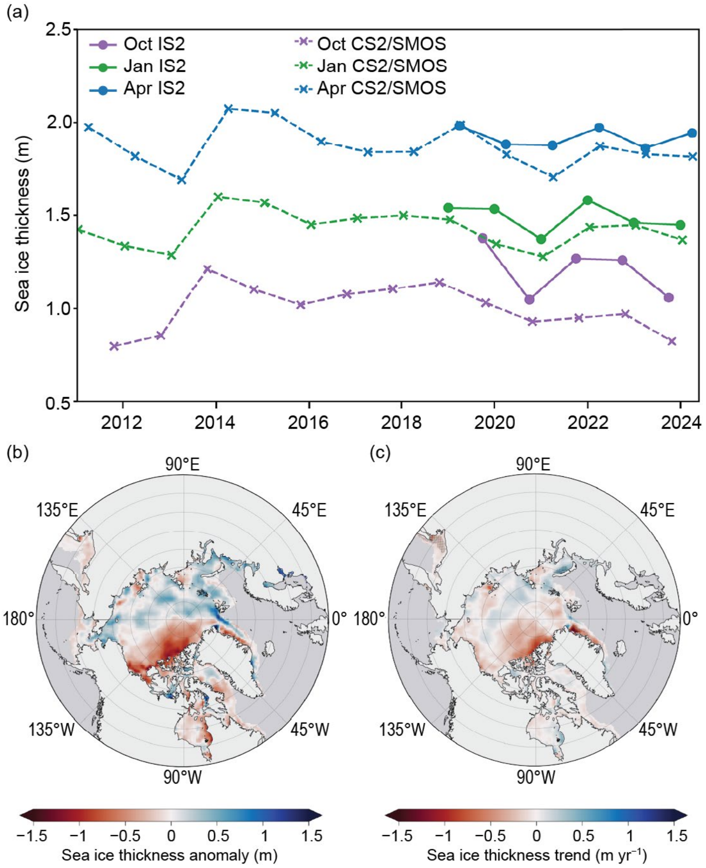

Fig. 5.17. (a) 2011–24 Oct (purple), Jan (green), and Apr (blue) monthly average sea ice thickness (m), calculated over an inner Arctic Ocean domain, same as the Arctic Ocean region in Fig. 5.14, from ICESat-2 (circles) and CryoSat-2/Soil Moisture Ocean Salinity (SMOS; crosses). (b) Apr 2024 sea ice thickness anomaly (m) map from CryoSat-2/SMOS (relative to the 2011–23 average); (c) CryoSat-2/SMOS Mar thickness trend map over the period 2011–24.

2024 thickness (Fig. 5.17b) from CryoSat-2/SMOS relative to the 2011–23 April mean shows that the Eurasian sector of the Arctic Ocean had relatively thicker sea ice than the 2011–23 mean. Sea ice was thinner than average in much of the North American sector, particularly in the Beaufort Sea and north of Greenland, as well as in the Canadian Archipelago. There is no significant trend in overall sea ice thickness since 2011 (Fig. 5.17a), which is consistent with the lack of a trend in multiyear ice extent during the same time period. However, there is substantial regional variability in the trends (Fig. 5.17c); thinning sea ice across much of the Eurasian side of the Arctic, particularly the Kara Sea, contrasts with thickening ice across the North American side, particularly north of the Canadian Archipelago and the East Greenland Sea. Sea ice thickness from CryoSat-2/SMOS integrated with ice concentration to provide winter volume estimates for 2011–24 also shows no substantial trend over the relatively short 14-year time series.

Sidebar 5.2: **Record-low sea ice conditions in the Northwest Passage in 2024**

—S. HOWELL AND M. BRADY

The Northwest Passage through the Canadian Arctic Archipelago (CAA) provides a shorter transit connecting the Atlantic and Pacific Oceans compared to the Northern Sea Route, Panama Canal, Suez Canal, or transiting around Cape Horn. The Northwest Passage has two primary routes: a preferred, shorter deepwater northern route directly through the Parry Channel, and a shallow-water southern route south of Victoria Island. The Northwest Passage was discovered by Sir Robert McClure in the 1850s, but ever-present sea ice has always prevented practical navigation. The recent loss of sea ice from climate change has challenged this notion.

Based on the 1991–2020 mean, sea ice area in the northern route of the Northwest Passage decreases gradually during the spring and summer months of May–September to about 73×10^3 km^2, then increases in mid-September with the onset of freeze-up (Fig. SB5.3). In 2024, sea ice area gradually declined below the 1991–2020 mean until August. It then declined rapidly until the end of September, reaching the lowest observed sea ice area since 1968 at 4×10^3 km^2 (Fig. SB5.3). The 2024 low eclipsed the previous record-low ice area of 9×10^3 km^2 set in September 2011 (Fig. SB5.3). Remarkably, there was virtually no sea ice present in and to the south of the Parry Channel at the end of September 2024 (Fig. SB5.4).

Low ice years within the Northwest Passage routes are driven by rapid sea ice melt associated with anomalously warm air temperatures, together with an atmospheric circulation pattern that prevents sea ice from being exported southward from higher-latitude regions (Howell et al. 2009, 2013). Air temperatures over the CAA were anomalously high during

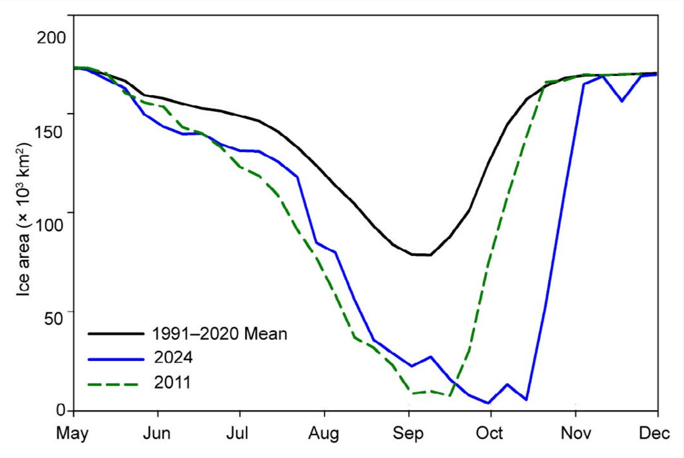

Fig. SB5.3. Time series of total sea ice area (× 10^3 km^2) within the Northwest Passage northern route for 2024 (solid blue line), 2011 (dashed green line), and the 1991–2020 mean (solid black line). (Data source: Canadian Ice Service.)

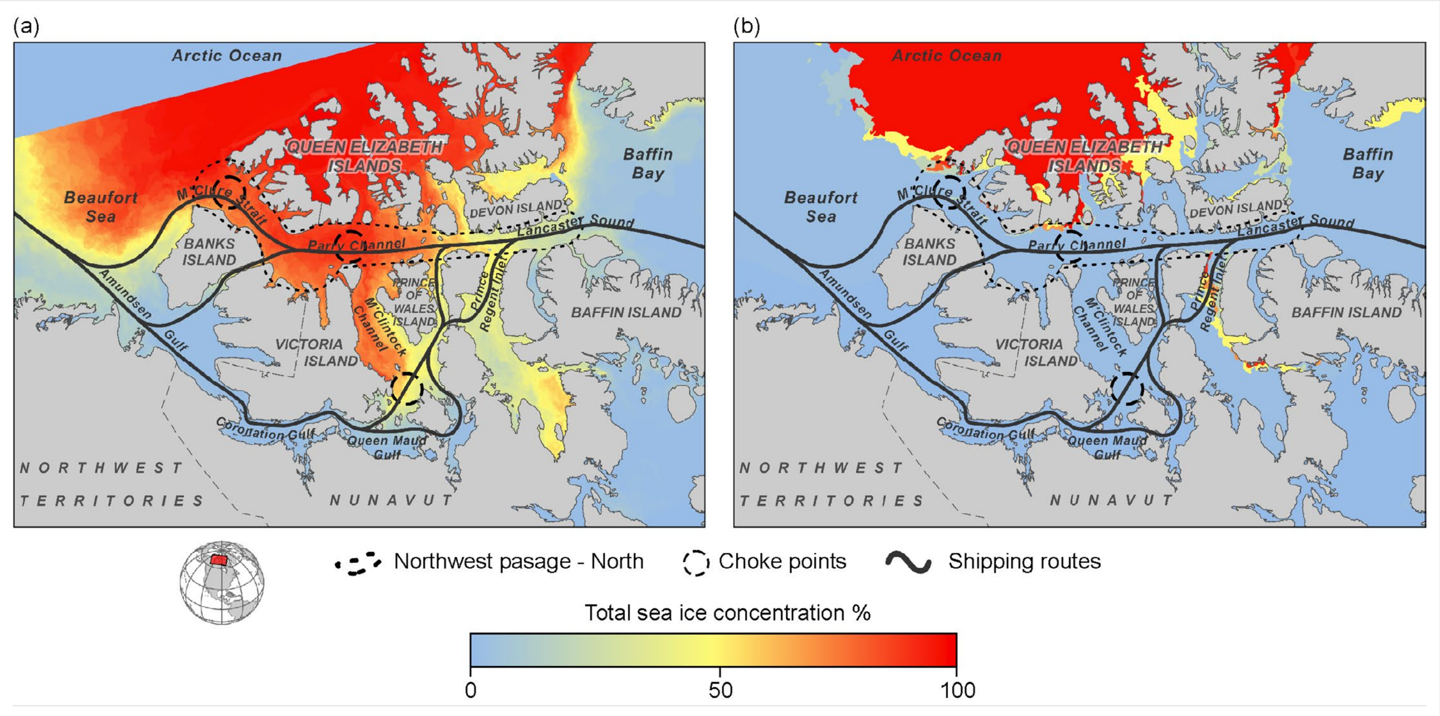

Fig. SB5.4. Spatial distribution of sea ice concentration (%) in the Canadian Arctic on 30 Sep for (a) the 1991–2020 mean and (b) 2024. (Data source: Canadian Ice Service.)

summer 2024 (see section 5c) and only ~2 × 10^3 km^2 of sea ice was exported southward from the Queen Elizabeth Islands into the northern route of the Northwest Passage during the melt season compared to a longer-term average of 27 × 10^3 km^2 (Howell et al. 2024). In addition, at the start of the 2024 melt season, the Northwest Passage northern route only contained about 10% multi-year ice, with the remaining 90% being made up of seasonal first-year ice. For the 1991–2020 mean, the Northwest Passage northern route contained 36% multi-year ice and 64% seasonal first-year ice. Since 2007, low-ice years in the Northwest Passage routes have been a more common occurrence as a result of less multi-year ice, which is thicker and more resilient to melt (Howell et al. 2023; see section 5f).

Although sea ice conditions in the Northwest Passage have been low since 2007, it is important to note that the process of Arctic Ocean sea ice export that transports thick multi-year ice southward from higher-latitude regions into the channels of the Northwest Passage still continues to operate (Howell et al. 2023). Specifically, the southward advection of Arctic Ocean sea ice creates or sustains "choke points", which are regions that almost always contain thick multi-year ice. These choke points are the most hazardous to maritime navigation and create barriers to a complete transit of the Northwest Passage (Fig. SB5.4). It has long been known that because of this process of sea ice transport, climate warming may not ease navigation conditions in the Northwest Passage (Melling 2002). Climate models have difficulty resolving the processes that create choke points within narrow Northwest Passage channels and may present a false sense of optimism regarding the feasibility of future navigation (Mudryk et al. 2021).

When warming does clear the Northwest Passage of sea ice, this is only temporary as sea ice returns most rapidly to the choke point regions, resulting in only a moderate increase in the shipping season. Cook et al. (2024) demonstrated that even during the recent low ice period from 2007 to 2021, the Northwest Passage shipping season length was reduced in several choke point regions. Sea ice is able to return to the choke points because it is sourced from the reservoir of the Arctic's oldest and thickest ice situated north of the CAA. As long as this multi-year sea ice reservoir remains and acts as an ice source for the choke points, climate change is unlikely to result in sustained shipping season increases in many Northwest Passage regions. The reservoir of multi-year ice to the north of the CAA is expected to persist even when the Arctic Ocean is classified as sea ice-free during the summer months (Sigmond et al. 2018; Notz and SIMIP Community 2020; Jahn et al. 2024; Fol et al. 2025). Overall, consistent lengthening of the shipping season along the entirety of all Northwest Passage routes as a result of climate change will be highly variable, and assumptions that less sea ice will enable safe transit should be avoided.

g. Greenland Ice Sheet

—K. Poinar, J. E. Box, T. L. Mote, X. Fettweis, B. D. Loomis, B. E. Smith, B. C. Medley, K. D. Mankoff, T. G. Askjaer, J. H. Scheller, R. S. Fausto, and M. Tedesco

The Greenland Ice Sheet loses mass when the sum of surface melt, surface water vapor flux, submarine melt, and discharge of solid ice exceeds the accumulated snowfall and rainfall. Net mass loss has occurred annually since the 1990s (Mouginot et al. 2019; Mankoff et al. 2021). Three independent estimates of the mass balance of the ice sheet over the 2024 mass balance year (1 September 2023 to 31 August 2024) are presented: input–output-derived mass balance of −76±48 Gt, gravity-derived mass balance of −55±35 Gt, and elevation-derived mass balance of −98±63 Gt. These three independent values agree within measurement uncertainties. All three measurements indicate that the Greenland Ice Sheet lost mass; however, the loss was 50%–80% less than the 2002–23 annual average.

Surface mass balance (SMB) comprises mass input from net snow accumulation and rainfall, and mass loss from melt, sublimation, and evaporation. These quantities are influenced by turbulent heat and water vapor energy fluxes, snow cover, and albedo, for which we summarize observations over the 2024 mass balance year.

Meteorological data from land-based weather stations (operated by the Danish Meteorological Institute) and on-ice weather stations operated by the Programme for Monitoring of the Greenland Ice Sheet (PROMICE; Fausto et al. 2021) across Greenland indicate that air temperatures were near the 1991–2020 average. During autumn (September–November 2023) and winter (December–February 2023/24), temperatures were above average. Spring (March–May 2024) temperatures were average, with above-average temperatures only in the far west and north. Summer (June–August 2024) temperatures were slightly above the 1999–2020 average at stations in the north and northeast, while Summit Station (+1.9°C anomaly) had its fourth-highest temperature on record (Fig. 5.18; section 5c). Summer temperatures were as much as 2.6°C below average in the south and west (Fig. 5.18), consistent with results from the Copernicus Arctic Regional Reanalysis (CARRA; Schyberg 2020; not shown). Thus, in situ data and CARRA suggest that the ERA5 summer 2024 anomaly is too positive for the west and south (Fig. 5.6c). Snow accumulation on the ice sheet (Vandecrux et al. 2023) during September 2023 through June 2024 was slightly below the 1991–2020 average in the north and northeast and substantially above average in the south and west (Fig. 5.18). The results from

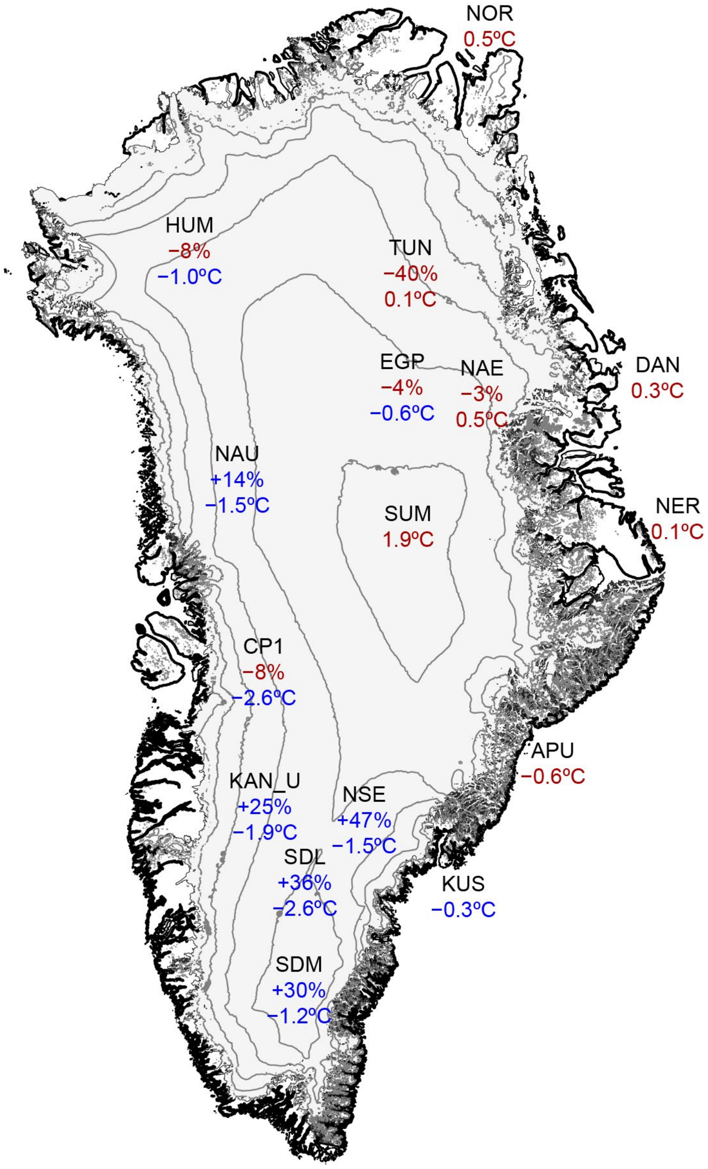

Fig. 5.18. Snowfall accumulation anomalies observed at 10 on-ice Programme for Monitoring of the Greenland Ice Sheet (PROMICE)/Greenland Climate Network (GC-Net) automated weather stations from Sep 2023 through Jun 2024 compared to 1991–2020 (top number, %) and near-surface air temperature anomalies from Jun through Aug 2024 compared to 1999–2020 (bottom number, °C). Summit Station (SUM) and Danish Meteorological Institute stations along the coast show air temperature anomalies compared to 1991–2020. Contours illustrate elevation above sea level. Red text indicates a warm temperature anomaly or a negative accumulation anomaly, while blue text indicates a cold temperature anomaly or a positive accumulation anomaly.

ERA5 (Fig. 5.8) are integrated over three-month seasons while the in situ data are integrated over the hydrological season from end-of-summer 2023 to end-of-summer 2024. The in situ data both for air temperature and snowfall have added credibility in their spatial coherence of the anomalies.

The average albedo during the melt season across the Greenland Ice Sheet was recorded by Sentinel-3 (Wehrlé et al. 2021) and found to be higher (brighter) than average (Fig. 5.19a). This was largely because of anomalously low air temperatures and excess snow cover, especially across the western ice sheet. Snow cover on the ice sheet in May and June slowed the onset of melt (Fig. 5.19b), especially in the west, where surface melt extent remained largely below the 1991–2020 mean all summer. This resulted in a below-average number of melt days observed across much of the western ice sheet (Fig. 5.19c; Sidebar 5.2). Across the eastern ice sheet, however, the melt season saw above-average duration.

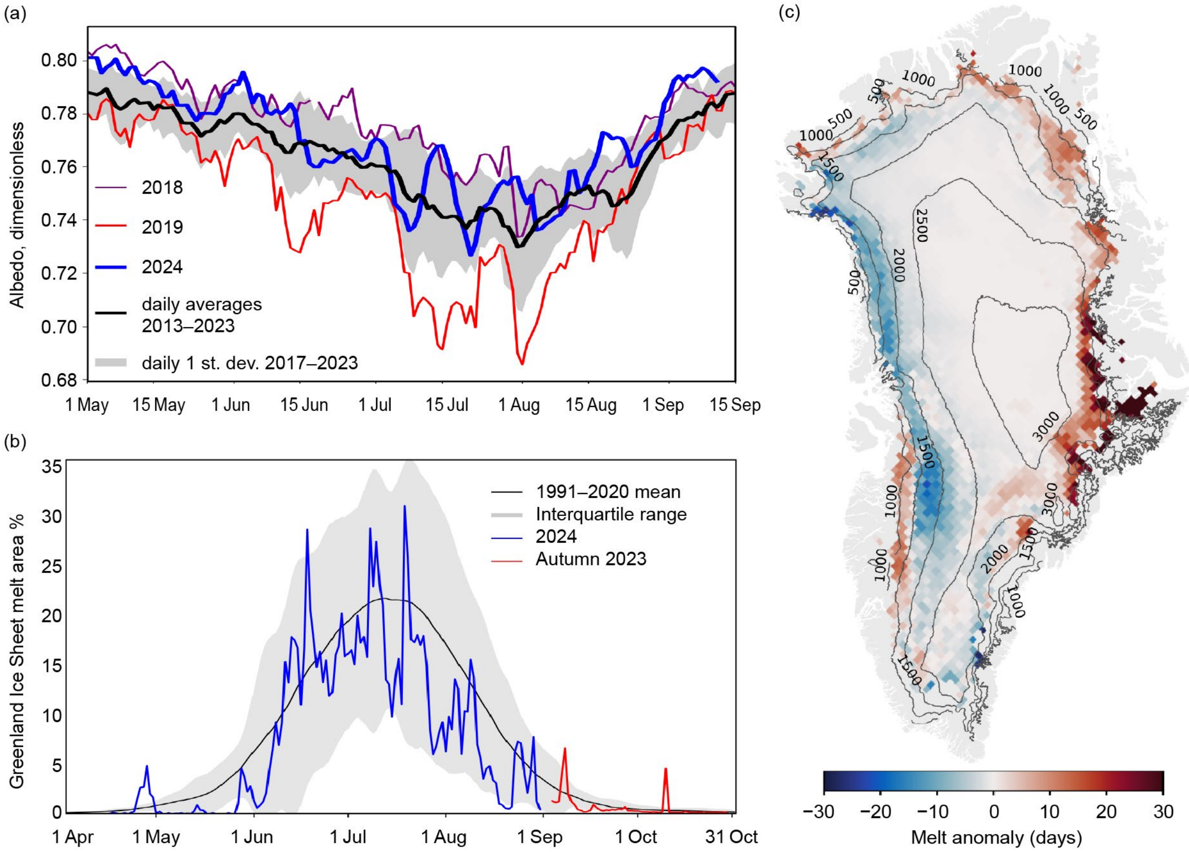

Fig. 5.19. (a) Greenland daily snow and ice albedo from Sentinel-3 for the 2024 melt season, alongside the 2017–23 average and recent bright-albedo (2018) and dark-albedo (2019) years. (b) Surface melt extent as a percentage (%) of ice sheet area during autumn 2023 (red) and spring/summer 2024 (blue), derived from passive microwave satellite observations (Mote 2007). (c) Number of surface melt days from 1 Apr to 31 Aug 2024, expressed as an anomaly with respect to 1991–2020, also derived from passive microwave.

The Modèle Atmosphérique Régionale version 3.14.1 regional climate model (MAR; Fettweis et al. 2020) forced by ERA5 (Hersbach et al. 2020) provides SMB values at 5-km horizontal resolution. The ice-sheet-wide total SMB over the 2024 mass balance year was 433±39 Gt, which is 17% above the 1991–2020 mean of 372±124 Gt yr^{-1}. This above-average SMB resulted from precipitation that was 7% higher than the 1991–2020 mean (6% higher snowfall, 21% higher rainfall), as well as runoff that was 5% lower. These anomalies do not exceed the 1991–2020 standard deviation and are thus statistically insignificant.

Tidewater glaciers contribute to ice mass loss by discharging icebergs into the ocean and through submarine melt. PROMICE estimates the sum of iceberg discharge and submarine melt from mass flow rate measurements collected near, but not precisely at, glacier calving fronts (Mankoff et al. 2020). Because the calving undergoes short-term advance and retreat, this is an approximation of terminus mass loss. For the 2024 mass balance year, estimated terminus mass loss was 488±46 Gt. This is 7% above the 1991–2020 mean and continues a period of increased loss that began in 2005 and peaked over 2020/21.

The terminus mass loss (488±46 Gt output) and basal melt (23±6 Gt output, Karlsson et al. 2021) is subtracted from the net SMB (431±39 Gt input) to obtain an input–output mass balance of –76±48 Gt over the 2024 mass balance year (Fig. 5.20). This is just 51% of the average input–output-derived annual mass loss over 1991–2020 of –156±80 Gt.

The Gravity Recovery and Climate Experiment (GRACE; 2002–17) and GRACE Follow-On (GRACE-FO; 2018–present) satellite missions measure gravity anomalies to observe changes in total ice mass (Tapley et al. 2019). We follow Colgan et al. (2015) to eliminate peripheral non-ice-sheet ice from these observations, yielding –55±35 Gt over the 2024 mass balance year (Fig. 5.20). This is just 21% of the average annual loss of –266±16 Gt over the 2002–23 GRACE/GRACE-FO record.

ICESat-2 measures ice sheet surface height. Changes in this value reflect changes in ice mass and firn air content; thus, model-based estimates of the latter (Gardner et al. 2023; Medley et al. 2022) were subtracted from ICESat-2 observations (Smith et al. 2023) to report mass change. We quantify uncertainty from the difference between models and from uncertainties in the height measurement and the air content. ICESat-2-derived mass change over the 2024 mass balance year was –98±56 Gt (Fig. 5.20).

The ICESat-2, GRACE-FO, and input–output mass balances agree within 43 Gt (56%) and give an average 2024 mass balance across all three methods of –77±50 Gt. This below-average ice loss occurred due to above-average precipitation, below-average melt, and despite glacier flow rates that were higher than the 1991–2020 average.

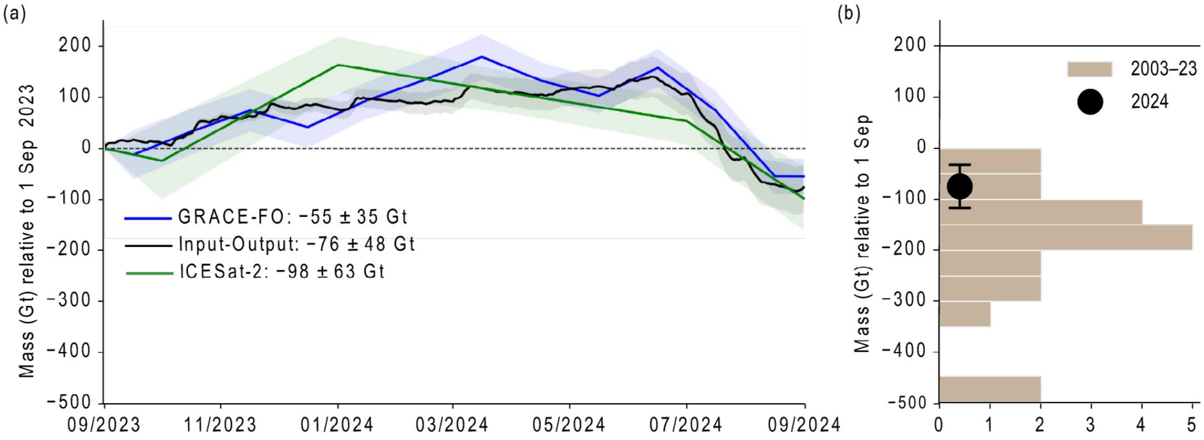

Fig. 5.20. (a) Observed mass balance (Gt) of the Greenland Ice Sheet over the 2024 mass balance year from the Gravity Recovery and Climate Experiment Follow-On (GRACE-FO), ICESat-2, and input–output, with uncertainties shaded. (b) Histogram of annual mass balance in years from 2003 to 2023, with full mass balance year observations by more than one method, shown as the average of the methods; and the multi-method averaged 2024 mass balance of –77±50 Gt.

Sidebar 5.3: Why Greenland Ice Sheet melt was so low in 2024

—J. BOX

Greenland Ice Sheet mass loss was muted in summer 2024 by the combined effect of anomalously north polar air influx and snowfall. The summer 2024 Greenland low melt anomaly was part of an Arctic-wide extreme in atmospheric circulation characterized by an extremely positive Arctic Oscillation Index (AOI). When the AOI is in its positive phase, a ring of strong winds circulating around the North Pole acts to confine colder air across the Arctic. This atmospheric state shielded Greenland from warm south air. The downstream air–sea exchange over near-record-warm North Atlantic sea surface temperatures (Timmermans and Labe 2024; see section 3b) instead entered the Barents Sea, producing record-high air temperatures and glacial melt on Svalbard to the east of Greenland (Arctic Council 2024; NASA 2024).

Here, additional details are provided on this low mass loss year for Greenland. Ice sheet automatic weather station data (Fausto et al. 2021; Vandecrux et al. 2023) recorded below-average June–August near-surface air temperatures and above-average snow accumulation (see section 5g, Fig. 5.18). A survey of Greenland and Arctic atmospheric circulation explains the situation. The June–August Greenland Blocking Index (GBI), which is useful in indicating south-to-north atmospheric heat and moisture transport for Greenland, (Hanna et al. 2016), ranked 2024 as the eighth lowest since 1961 (z-score of −1.1), consistent with projections for the GBI to have a negative tendency under anthropogenic climate change (Delhasse et al. 2021). Atmospheric circulation during July, and even more so in August (Fig. SB5.5), drew cold polar air down the western ice sheet where melting is normally concentrated. The typical southern summer warm air masses were deflected away from Greenland, as indicated by the second-highest AOI (z-score of +1.95) since 1961 (Fig. SB5.6). When the AOI is in its positive phase, a ring of strong winds circulating around the North Pole reduces north–south air exchanges between the polar region and the midlatitudes. The AOI was especially positive in August and moderately positive in July, but essentially neutral in June. The reduced summer temperatures over Greenland as compared with northern Canada (see section 5c, Fig. 5.6c) may have also been influenced by additional northerly advection due to the strong blocking high pressure over Canada (see section 5b, Fig. 5.3c).

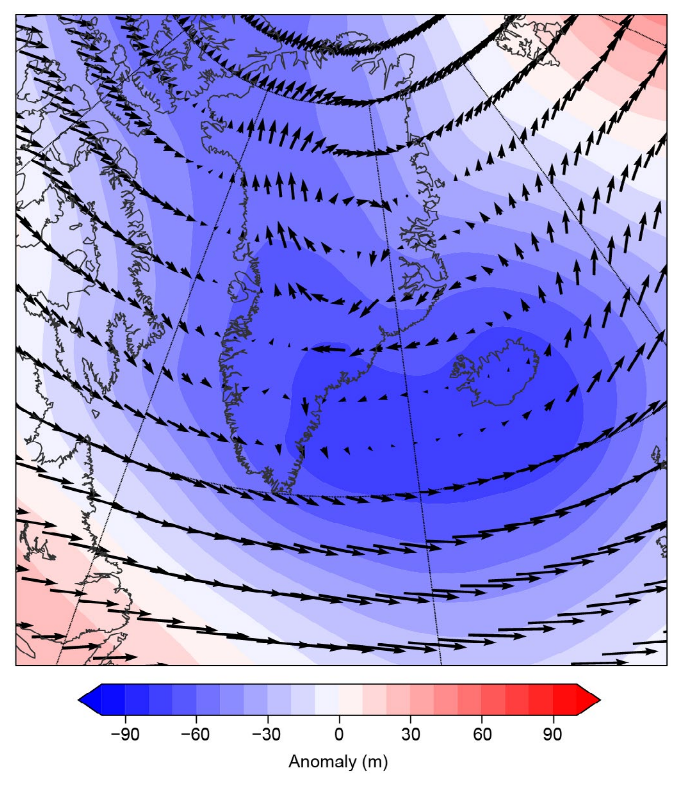

Fig. SB5.5. Jul–Aug 2024 ERA5 (Hersbach et al. 2020) wind vectors (arrows, m s^{-1}) at 700 hPa and geopotential height anomalies (m) at that level, approximately 3000 m above sea level, indicate the prevailing pattern during mid-to-late melt season. The 2024 season was marked by suppressed melt that resulted from cold polar air flowing southward along the western ice sheet where most surface melting typically occurs.

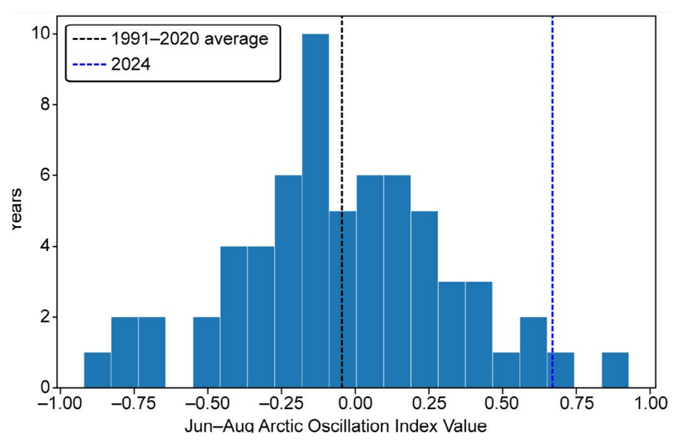

Fig. SB5.6. A highly anomalous summer 2024 Arctic Oscillation Index (AOI) relative to historical conditions since 1961 and the 1991–2020 average. Vertical lines indicate the June–August (JJA) 1991–2020 average (black) and the JJA 2024 AOI (blue). The bars indicate the number of years since 1961 within AOI intervals of 0.0924. The Arctic Oscillation is a weather pattern that involves the shifting of air pressure between the Arctic and midlatitudes (NCEP 2025; Zhou et al. 2001). The AOI is obtained from the 2024 pattern relative to the leading mode of empirical orthogonal function (EOF) analysis of monthly mean 1000-mb heights during the 1979–2000 period.

h. Arctic river discharge

—J. W. McClelland, A. I. Shiklomanov, A. Suslova, M. Tretiakov, R. G. M. Spence, S. E. Tank, and S. Zolkos

The Arctic Ocean accounts for approximately 1% of the global ocean's volume, yet receives more than 10% of global river discharge (McClelland et al. 2012). Consequently, effects of river inputs on ocean processes are more pronounced in the Arctic, and changes in river inputs have greater potential to impact physics, chemistry, and biology than in other oceans. Because rivers naturally integrate the processes that are occurring throughout their watersheds, trends in the discharge and chemistry of Arctic rivers can also be indicative of widespread changes in precipitation, permafrost thaw, and other anthropogenic impacts on land (Holmes et al. 2013; Tank et al. 2023).

Multiple studies over the past 20 years have demonstrated that discharge from Arctic rivers is increasing. Evidence first emerged from long-term Russian datasets (Peterson et al. 2002) and more recently from shorter U.S. and Canadian datasets (Durocher et al. 2019). While uncertainty remains around drivers of this trend, it is consistent with intensification of the Arctic hydrologic cycle (Rawlins et al. 2010). Warming is driving increased atmospheric moisture transport into the Arctic, resulting in greater precipitation (section 5d). This is particularly evident during colder months of the year. For example, snowfall has increased during autumn and early winter in western Siberia (Wegmann et al. 2015) and in the Canadian Arctic (Kopec et al. 2016; Yu and Zhong 2021). Evaporation is also increasing with warming, but the river discharge trend aligns with an overall increase in net precipitation.

River discharge was last included in the 2022 *State of the Climate* report, so discharge data for 2023 and 2024 are presented here. Data analysis and presentation focus on eight rivers that collectively drain much of the pan-Arctic watershed (Fig. 5.21). Six of these rivers are in Eurasia and two are in North America. Discharge measurements for the Eurasian rivers were initiated during different years, with discharge being tracked on all six by 1936. Discharge measurements did not begin until 1973 for the Mackenzie River and 1976 for the Yukon River in North America. Years are presented as "water years", 1 October–30 September, a common practice in hydrology to align runoff and associated precipitation within the same year. Thus, water year 2024 covers the period 1 October 2023 through 30 September 2024. The data used in this analysis are freely available through the Arctic Great Rivers Observatory (arcticgreatrivers.org).

Combined annual discharge for the eight rivers was 2387 km^3 for 2023 and 2447 km^3 for 2024 (Table 5.1). These values were similar to

SOURCE: HTTPS://ARCTICGREATRIVERS.ORG/DATA/

Fig. 5.21. Watersheds of the eight largest Arctic rivers included in this analysis. Collectively, these rivers drain approximately 70% of the 16.8 million km^2 pan-Arctic watershed (indicated by the red boundary line). The red dots show the location of the discharge monitoring stations.

Table 5.1. Annual discharge (km^3) for the eight largest Arctic rivers. Results are shown for 2023 and 2024 along with mean values for the 1991–2020 reference period. Values for years 2024 and 2023 are provisional data and are subject to modification until official data are published.

Water Year	Yukon	Mackenzie	S. Dvina	Pechora	Ob′	Yenisey	Lena	Kolyma	Total
2024	242	192	102	118	471	743	491	88	2447
2023	273	233	70	84	337	731	578	80	2387
1991–2020	215	297	108	119	424	618	582	80	2442

average discharge for the 1991–2020 reference period, differing by less than 3% from the reference average for both years. There were, however, notable departures from reference averages for some individual rivers. For example, Yenisey discharge was much higher (+18% in 2023, +20% in 2024) and Mackenzie discharge was much lower (–22% in 2023, –35% in 2024) than the reference during both years. The Yenisey values continued a pattern of higher-than-reference discharge that was highlighted in the 2022 *State of the Climate* report, but these values should be viewed with caution as data accuracy for the Yenisey has declined significantly since 2003 due to a lack of direct discharge measurements for rating curve updates (Tretiyakov et al. 2022). In contrast with the Yenisey, discharge values for the Mackenzie swung from remarkable highs in the 2022 report to record lows in this report. The low Mackenzie discharge values during 2023, and even more so during 2024, were driven by extreme drought conditions in southerly portions of the watershed (Government of Northwest Territories 2025; section 5d).

Average monthly discharge values for the Eurasian rivers during 2023 and 2024 were similar to average reference values throughout the year (Fig. 5.22a). The North American rivers, on the other hand, showed substantial departures from reference averages during some months (Fig. 5.22b). Average discharge for the North American rivers was particularly low during May, June, and July 2024. This effect was driven by very low discharge in the Mackenzie River. Discharge was also below average in the Mackenzie during all other months of 2024, but these lows were opposed by above-average discharge in the Yukon. Monthly discharge values were lower in the Mackenzie and higher in the Yukon (relative to reference) during 2023 as well, but the Mackenzie lows were less extreme during 2023 than during 2024 for most months. Exceptions were July, August, and September, when discharge in the Mackenzie was far below average during both years.

The 89-year time series available for the Eurasian Arctic rivers demonstrates a continuing, and perhaps accelerating, increase in their combined discharge (Fig. 5.23a). There is a positive linear trend across the entire time series showing that average annual discharge of Eurasian Arctic rivers is increasing by 2.5 km^3 per year. When data are considered from 1976 through 2024 (the period of record for North American rivers), the average annual increase in discharge for Eurasian Arctic rivers is 3.9 km^3 per year. For the North American Arctic rivers, the average discharge increase over the 1976–2024 timeframe is 1.1 km^3 per year (Fig. 5.23b). These observations show that, although river discharge varies widely over interannual to decadal timeframes, longer-term increases in river discharge are a pan-Arctic phenomenon. Evidence of increasing Arctic river discharge is strongest for Eurasian rivers where datasets are longest, but the signal of change in North American rivers is becoming increasingly robust as discharge measurements

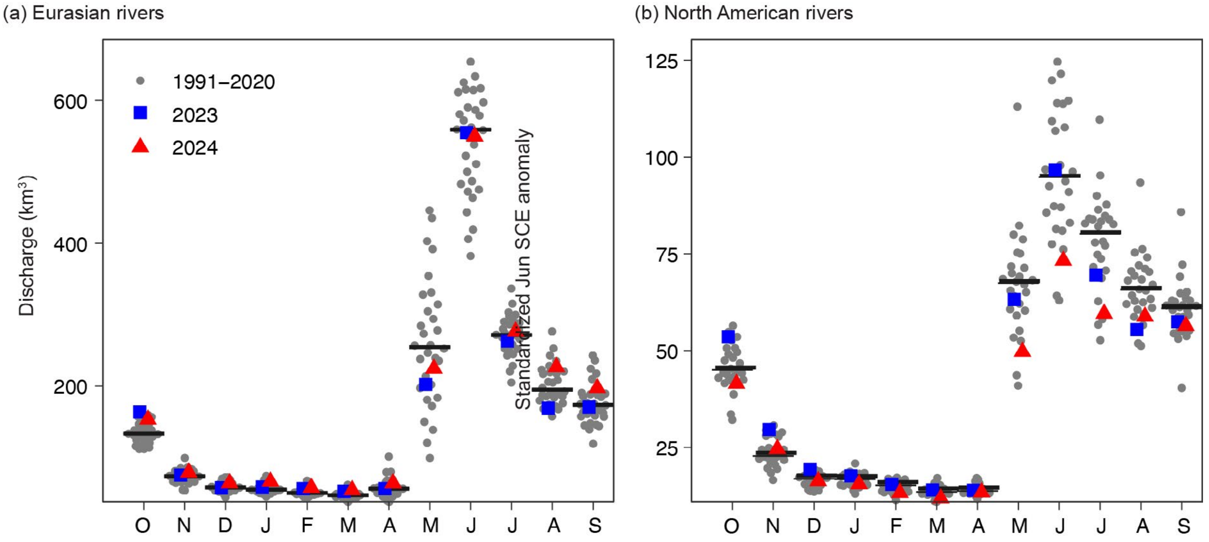

Fig. 5.22. Monthly discharge (km^3) in (a) Eurasian and (b) North American rivers for 2023 and 2024 compared to monthly discharge throughout the 1991–2020 reference period. Gray dots mark the combined monthly discharge of contributing rivers during individual years, and black bars mark the average monthly discharge of combined rivers over the reference period. Note the different magnitudes of discharge between the Eurasian and North American rivers (see y-axes).

continue and the overall observational period becomes longer.

The timing of the spring freshet, when discharge rapidly shifts from low to high flow conditions, is also changing across the pan-Arctic domain (Fig. 5.23c). The spring freshet is starting earlier in Eurasia and North America, showing a linear change of approximately nine days over the 1976–2024 timeframe. This seasonal shift is associated with earlier snowmelt in the Arctic (Derksen and Mudryk 2023; section 5g), which is driven by warming air temperatures as well as more frequent rain-on-snow events during the spring (Shrestha et al. 2021; Dou et al. 2021).

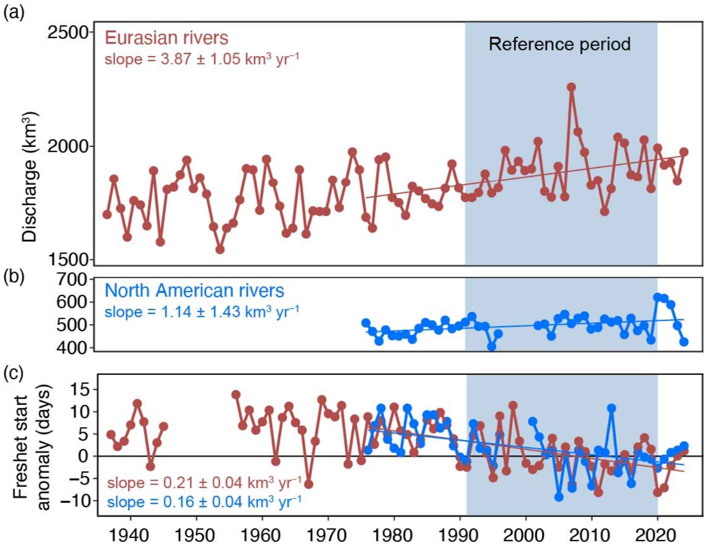

Fig. 5.23. Long-term trends in annual discharge (km^3) for (a) Eurasian (dark red) and (b) North American (blue) Arctic rivers, and (c) freshet start day anomalies relative to the 1991–2020 reference period average for both. Freshet start day anomalies were calculated for individual rivers and then averaged by continent. Time series gaps reflect insufficient monthly (North American river discharge) and daily (Eurasian river freshet start day anomalies) data for calculations during some timeframes. Reported slopes are for 1976–2024 ($p<0.05$ in all cases).

i. Terrestrial snow cover

—L. Mudryk, A. Elias Chereque, C. Derksen, K. Luojus, and B. Decharme

Many components of the Arctic land surface are directly influenced by snow cover, including the surface energy budget, permafrost, terrestrial and freshwater ecosystems, and the ground thermal regime, with implications for the carbon cycle (Brown et al. 2017; Meredith et al. 2019; and references therein). Even following the snow cover season, the influence of spring snowmelt timing persists through impacts on river discharge timing and magnitude, surface water, soil moisture, vegetation phenology, and fire risk (Meredith et al. 2019).

Snow cover extent (SCE) anomalies during 1967 to 2024 are illustrated for both the North American and Eurasian sectors of the Arctic in Fig. 5.24 (relative to the 1991–2020 baseline; data from the NOAA snow chart climate data record; Robinson et al. 2012). In May 2024, Eurasian Arctic SCE was slightly above normal (20th-lowest May value in the 58-year record), related to cold spring conditions over northern Europe and western Russia (section 5c, Fig. 5.6b); however, by June, Eurasian SCE had dropped below normal (14th-lowest June value in the 58-year record). North American Arctic SCE during 2024 was below normal throughout May and June (SCE values for each month ranked seventh lowest in the 58-year record). See section 2c5 for more details.

Snow cover duration (SCD) anomalies for the 2023/24 snow season (difference from the average number of days with snow cover) are shown in Fig. 5.25 (data from the NOAA daily Interactive Multisensor Snow and Ice Mapping System [IMS] snow cover product; U.S. National Ice Center 2008). SCD anomalies are computed separately for each half of the snow season: the "onset period" of August 2023 to January 2024 (relative to a 25-year baseline starting in August 1998; Fig. 5.25a), and the "melt period" of February 2024 to July 2024 (relative to a 25-year baseline starting in February 1999; Fig. 5.25b). During the 2023/24 snow season in Eurasia, broad portions of the continent experienced either early snow onset (northern Europe and parts of eastern Siberia) or delayed snow melt (western Russia and easternmost Siberia). This combination of early onset and delayed melt led to one of the longer snow seasons of the past 26 years across the majority of the Eurasian Arctic (rank of season length shown in Fig. 5.25c). For North America,

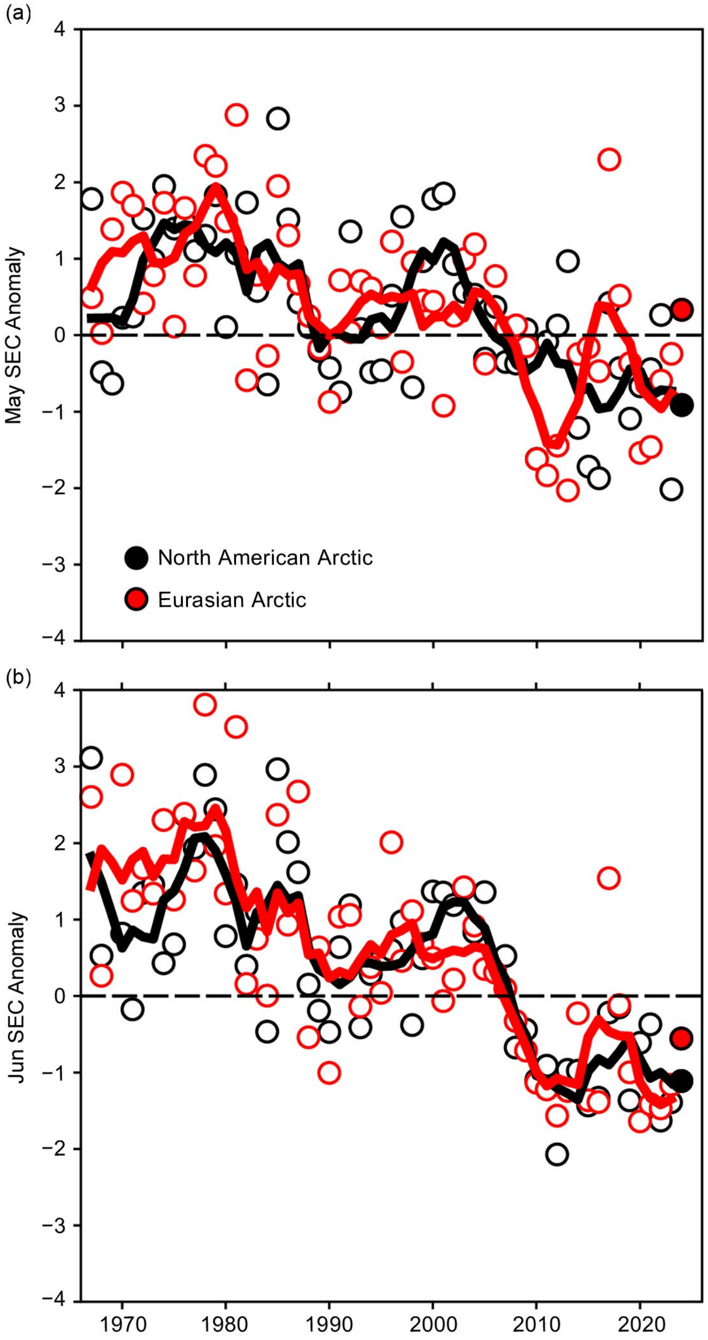

Fig. 5.24. Monthly snow cover extent (SCE) anomalies for Arctic terrestrial land areas (poleward of 60°N) for (a) May and (b) Jun from 1967 to 2024. Anomalies are relative to the average for 1991–2020 and standardized (each observation differenced from the mean and divided by the standard deviation, and thus unitless). Solid black and red lines depict five-year running means for North America and Eurasia, respectively. Filled circles highlight 2024 anomalies. (Data source: Robinson et al. [2012].)

a combination of late onset and early spring melt resulted in one of the shortest snow seasons of the last 26 years across portions of northern Canada (Fig. 5.25c).

Finally, snow water equivalent (SWE), a measure of water contained within the snowpack, is used to characterize Arctic snow accumulation over the 2023/24 season. Maps of SWE anomalies are shown in Fig. 5.26 (anomaly shown for each month is the average of four products relative to their respective 1991–2020 baselines: Snow Climate Change Initiative [CCI; Luojus et al. 2022], MERRA-2 [GMAO 2015], ERA5-Land [Muñoz Sabater 2019], and Crocus-ERA5 [Decharme et al. 2024]). Four datasets are considered because averaging multiple SWE products has been shown to be more accurate than individual datasets when validated with in situ observations (Mortimer et al. 2020). In April 2024, the majority of Arctic land areas on both continents had positive SWE anomalies, indicating higher-than-normal snowfall accumulations since the preceding autumn (April is the approximate month that total snow mass across the terrestrial pan-Arctic region peaks, before increasing May and June temperatures lead to melt). Strong reductions in the relative amount of SWE occurred over the North American Arctic during May, while over Eurasia large regions of above-normal SWE still existed. By June, the amount and extent of Eurasian snow cover was also greatly reduced, consistent with the anomalies in Fig. 5.24b. However, SWE anomalies between the Ob and Yenisei Rivers and at the far eastern tip of the continent were still

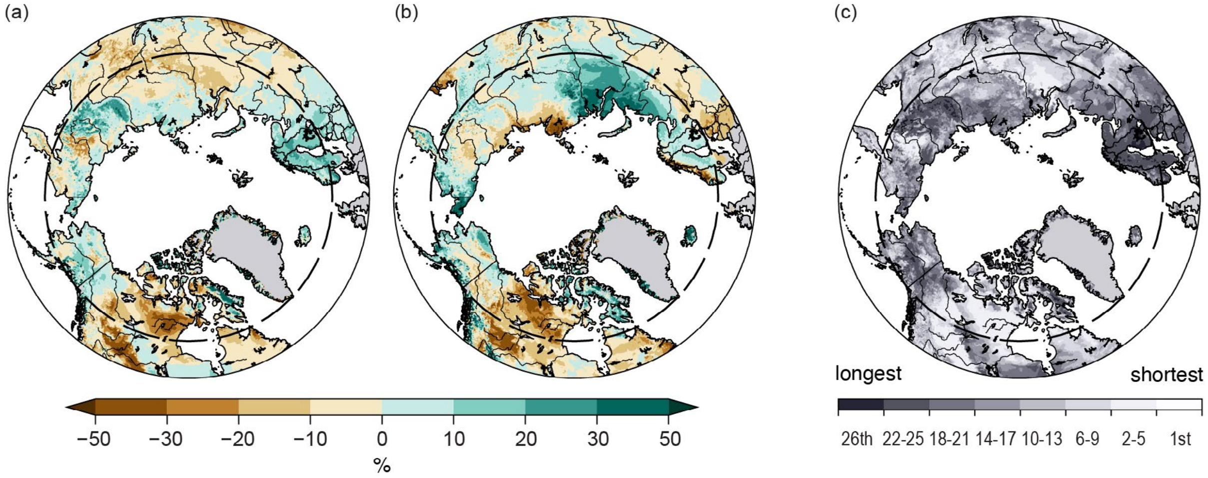

Fig. 5.25. Snow cover duration (SCD) anomalies (% difference relative to climatological number of snow-free days for the 1998/99–2022/23 baseline) for the 2023/24 snow year: (a) snow onset period (Aug 2023–Jan 2024) and (b) snow melt period (Feb–Jul 2024). (c) Rank of the 2023/24 snow season length within the past 26 years of observation. Brown (green) indicates more (fewer) snow-free days than average. Latitude 60°N is marked by the gray dashed circle. (Data source: U.S. National Ice Center [2008].)

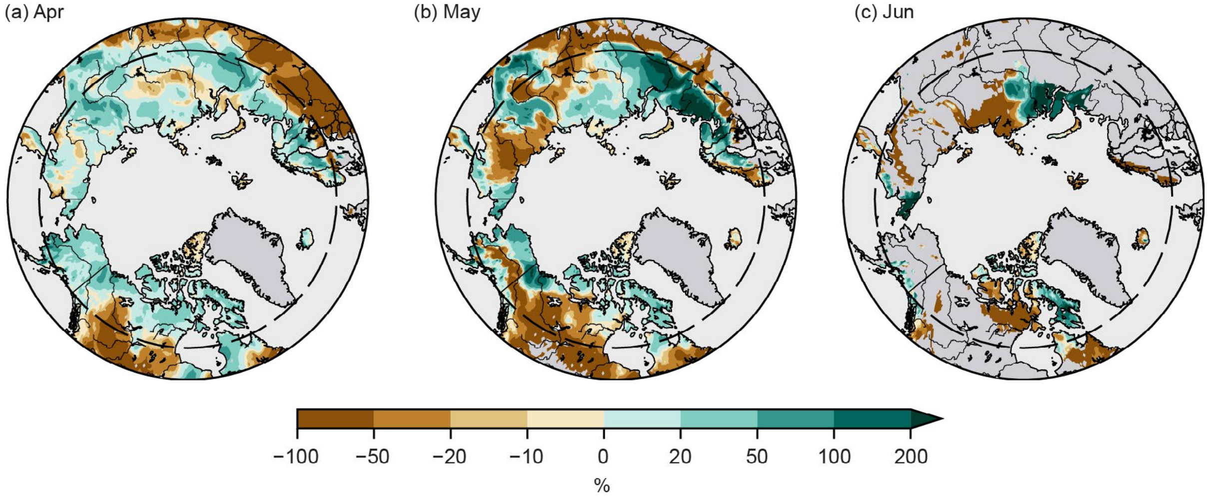

Fig. 5.26. Snow water equivalent (SWE) anomalies (% difference from the 1991–2020 baseline) in 2024 for (a) Apr, (b) May, and (c) Jun. Brown (green) indicates lower (higher) snow amounts than average. Latitude 60°N is marked by the gray dashed circle. (Data source: selection of four SWE products from Snow Climate Change Initiative [CCI; Luojus et al. 2022]; MERRA-2 [GMAO 2015]; ERA5-Land [Muñoz Sabater 2019]; and Crocus [Decharme et al. 2024].)

above normal, consistent with the longer-than-normal melt season observed in those regions (Fig 5.25b). Over North America, most of the Canadian Arctic Archipelago had below-normal SWE during June except for Baffin Island.

In summary, snow accumulation during the 2023/24 winter was above average across both continents; however, the duration of the snow season contrasted strongly between them. Over much of northern Canada, warm spring temperatures resulted in a shorter-than-normal snow season, consistent with or even shorter than what has typically been observed over the last 15 years (Fig. 5.25c). Over broad portions of Eurasia and Alaska, early snow onset and above-normal SWE during most of May resulted in a longer-than-normal snow season (Fig. 5.25c) and higher-than-average May SCE (Fig 5.24a). However, by June, Eurasian SCE was back down to values consistent with those seen over the past 15 years.

j. Permafrost

—S. L. Smith, V. E. Romanovsky, K. Isaksen, K. E. Nyland, N. I. Shiklomanov, D. A. Streletskiy, and H. H. Christiansen

Permafrost refers to earth materials (e.g., bedrock, mineral soil, organic matter) that remain at or below 0°C for at least two consecutive years, although most permafrost has existed for centuries to many millennia. Extensive regions of high-latitude landscapes are underlain by permafrost. The active layer, which thaws and refreezes annually, overlies the permafrost. Warming of permafrost (especially if ice-rich), active-layer thickening, and ground ice melt cause changes in surface topography, hydrology, and landscape stability, with implications for Arctic infrastructure, ecosystem integrity, and human livelihoods (Smith et al. 2022; Hjort et al. 2022; Wolken et al. 2021). Changes in permafrost conditions also affect the rate of release of greenhouse gases into the atmosphere, potentially accelerating global warming (Miner et al. 2022; Schuur et al. 2022).

Permafrost conditions respond to shifts in the surface energy balance through interrelated changes in ground temperature and active-layer thickness (ALT). Ground temperatures fluctuate seasonally near the surface, while below the depth of seasonal temperature variation, they reflect longer-term climate. Long-term changes in permafrost temperatures are driven by changes in air temperature but also reflect local variability due to influences such as snow cover, vegetation characteristics, and soil moisture (Romanovsky et al. 2017; Smith et al. 2022). Monitoring sites across the Arctic (Fig. 5.27) have been recording ground temperature in the upper 30 m for up to five decades, providing critical data on changes in permafrost conditions. Observed changes in ALT are more reflective of shorter-term (year-to-year) fluctuations in climate and are especially sensitive to changes in summer air temperature and precipitation.

Since the 1980s, permafrost temperatures have continued to increase on a decadal time scale across the Arctic. Greater increases are generally observed in colder permafrost (temperature <–2°C) at higher latitudes (Smith et al. 2022, 2024a), partly due to greater increases in air temperature (Figs. 5.27, 5.28). Over the last 30 years, positive ALT trends (Fig. 5.29) are evident from all permafrost regions examined, but trends are more muted for the Alaskan North Slope, northwestern Canada, and East Siberia (Smith et al. 2024a).

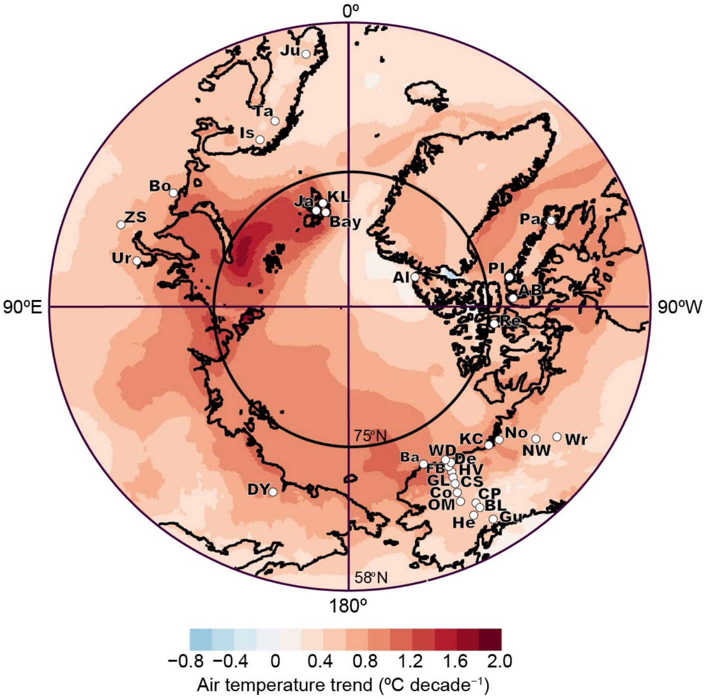

Fig. 5.27. Locations of the permafrost temperature monitoring sites (for which data are shown in Fig. 5.28), superimposed on annual average surface air temperature trends (°C decade^{-1}) during 1981–2024 from ERA5 (Hersbach et al. 2020; data available at https://cds.climate.copernicus.eu), which largely covers the period of record for permafrost monitoring. See Table 5.2 for site names. Information about these sites is available at http://gtnpdatabase.org/ and https://permafrost.gi.alaska.edu/sites_map.

1. PERMAFROST TEMPERATURE

Permafrost temperatures in 2024 were the highest on record at 8 of the 25 reporting sites; all of the record sites were in North America except for one on Svalbard (Table 5.2). Temperatures were higher in 2024 compared to 2023 at 13 of 21 North American sites (Figs. 5.28a,b). In the Beaufort–Chukchi region, permafrost temperatures in 2024 were the same or up to 0.2°C higher than those in 2023 at seven of eight sites (Fig. 5.28a). The higher temperatures reflect the increase in air temperatures that occurred in 2023 following a period of cooling that started in 2019/20. For discontinuous permafrost in Alaska and northwestern Canada, the 2024 permafrost temperatures were higher than those in 2023 at 5 of the 10 of sites, three of which reported record-high temperatures (Fig. 5.28b). Record-high temperatures were also observed at all three sites reporting in the eastern and high Canadian Arctic (Fig. 5.28c). The high Arctic cold permafrost of Svalbard was warmer in 2024 at the two sites reporting compared to 2023 (Fig. 5.28d). In warmer permafrost at one of two other reporting Nordic sites, temperatures in 2024 were higher than in 2023 (Fig. 5.28d; Table 5.2).

Throughout the Arctic, warming of permafrost with temperatures near 0°C (temperatures >–2°C) is slower (generally <0.3°C decade^{-1}) than colder permafrost sites due to latent heat effects related to melting ground ice. At cold continuous permafrost sites in the Beaufort–Chukchi region, permafrost temperatures have increased by 0.4°C decade^{-1} to 0.8°C decade^{-1} with similar increases (0.3°C decade^{-1} to 0.8°C decade^{-1}) for the three sites reporting in 2024 in the eastern and high Canadian Arctic (Figs. 5.28a,c; Table 5.2). Permafrost in Svalbard has warmed by up to 0.7°C decade^{-1} (Fig. 5.28d; Table 5.2), and significant permafrost warming has been detected down to 100-m depth (Isaksen et al. 2022). In the discontinuous permafrost regions of Scandinavia (Juvvasshøe and Iskoras), warming is continuing at rates of about 0.1°C decade^{-1} to 0.2°C decade^{-1}, with thawing occurring at Iskoras (Fig. 5.28d; Isaksen et al. 2022). Similar rates (Figs. 5.28b,d) are observed in the warm permafrost of northwestern North America (e.g., Smith et al. 2024b).

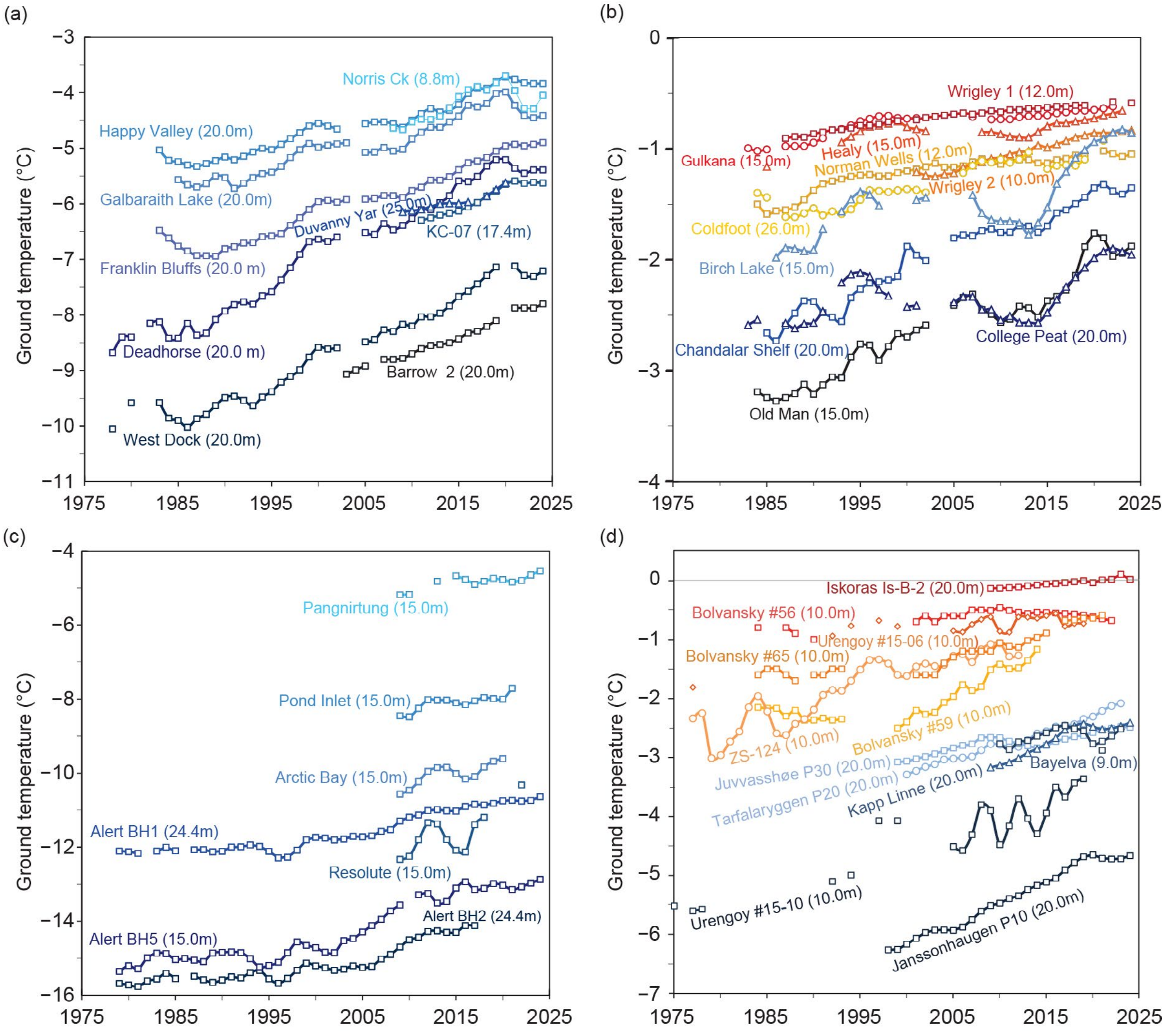

Fig. 5.28. Time series of mean annual ground temperature (°C) at depths of 9 m–26 m below the surface at selected measurement sites that fall roughly into Adaptation Actions for a Changing Arctic priority regions (see Romanovsky et al. 2017): (a) cold continuous permafrost of northwestern North America and northeastern East Siberia (Beaufort–Chukchi region); (b) discontinuous permafrost in Alaska and northwestern Canada; (c) cold continuous permafrost of eastern and high Arctic Canada (Baffin Davis Strait); and (d) continuous to discontinuous permafrost in Scandinavia, Svalbard, and Russia/Siberia (Barents region). Temperatures are measured at or near the depth of zero annual amplitude, where the seasonal ground temperature variations are less than 0.1°C. Note differences in y-axis value ranges. Borehole locations are shown in Fig. 5.27 (data are updated from Smith et al. 2024a).

Table 5.2. Rate of change in mean annual ground temperature (°C decade^{-1}) for permafrost monitoring sites shown in Fig. 5.28. The periods of record are shown in parentheses below the rates of change. For sites where measurements began prior to 2000, the rate of change for the entire available record and the period after 2000 are provided. Stations with record-high 2024 temperatures are indicated with a thermometer icon (🌡) and are underlined. Asterisks denote sites not reporting in 2024. Regions correspond to those shown in Fig. 5.28.

Region	Site	Entire Record	Since 2000
Northeast Siberia *(Beaufort–Chukchi Region)*	Duvany Yar (DY)*	NA	+0.4 (2009–20)
Alaskan Arctic plain *(Beaufort–Chukchi Region)*	West Dock (WD), Deadhorse (De), Franklin Bluffs (FB) 🌡, Barrow (Ba) 🌡	+0.5 to +0.8 (1978–2024)	+0.5 to +0.7 (2000–24)
Northern foothills of the Brooks Range, Alaska *(Beaufort–Chukchi Region)*	Happy Valley (HV), Galbraith Lake (GL)	+0.4 (1983–2024)	+0.4 (2000–24)
Northern Mackenzie Valley *(Beaufort–Chukchi Region)*	Norris Ck (No)*, KC-07 (KC)	NA	+0.4 to +0.6 (2008–24)
Southern foothills of the Brooks Range, Alaska *(Discontinuous Permafrost: Alaska and Northwestern Canada)*	Coldfoot (Co) 🌡, Chandalar Shelf (CS), Old Man (OM)	+0.2 to +0.4 (1983–2024)	+0.2 to +0.3 (2000–24)
Interior Alaska *(Discontinuous Permafrost: Alaska and Northwestern Canada)*	College Peat (CP), Birch Lake (BL), Gulkana (Gu)*, Healy (He)*	+0.1 to +0.3 (1983–2024)	<+0.05 to +0.4 (2000–24)
Central Mackenzie Valley *(Discontinuous Permafrost: Alaska and Northwestern Canada)*	Norman Wells (NW), Wrigley (Wr1, Wr2 🌡)	+0.1 (1984–2024)	+0.1 to +0.2 (2000–24)
Baffin Island *(Baffin Davis Strait Region)*	Pangnirtung (Pa) 🌡, Pond Inlet (PI)*	NA	+0.3 (2009–24)
High Canadian Arctic *(Baffin Davis Strait Region)*	Resolute (Re)*	NA	+1.1 (2009–22)
High Canadian Arctic *(Baffin Davis Strait Region)*	Alert (Al) @ 15 m 🌡, Alert (Al) @ 24 m 🌡	+0.6, +0.4 (1979–2024)	+0.8, +0.6 (2000–24)
Northwest Siberia *(Barents Region)*	Urengoy 15-06* and 15-08* (Ur)	+0.2 to +0.5 (1974–2021)	+0.1 to +0.8 (2005–21)
Russian European North *(Barents Region)*	Bolvansky 56* and 65* (Bo)	+0.1 to +0.3 (1984–2022)	0 to +0.5 (2001–22)
Svalbard *(Barents Region)*	Janssonhaugen (Ja), Bayelva (Bay)*, Kapp Linne 1 (KL) 🌡	+0.7 (1998–2024)	+0.1 to +0.7 (2000–24)
Northern Scandinavia *(Barents Region)*	Tarfalarggen (Ta)*, Iskoras Is-B-2 (Is) 🌡	NA	+0.1 to +0.5 (2000–24)
Southern Norway *(Barents Region)*	Juvvasshøe (Ju)	+0.2 (1999–2024)	+0.2 (2000–24)

2. ACTIVE-LAYER THICKNESS

Active-layer thickness is measured either directly using thaw tubes or inferred from the end-of-season thaw depth measurements by mechanical probing or from the maximum seasonal depth of the 0°C isotherm interpolated from borehole temperature records. The ALT trends shown in Fig. 5.29 are based primarily on spatially distributed mechanical probing across representative landscapes to determine the depth to the top of permafrost.

The highest long-term (1999–2024) rates of ALT increases of 0.4 m decade^{-1} and 0.2 m decade^{-1} are observed in the Alaskan Interior and West Siberia, respectively, with 2024 ALT values well above the 2009–18 mean for both regions. A record-high 2024 ALT anomaly was observed on Svalbard in response to exceptionally high summer air temperatures, especially in August.

Sites on the North Slope of Alaska, Greenland, northwestern Canada (2023 data), and East Siberia (2023 data) indicate no significant ALT changes over the last five years. This can be partially attributed to climatic influences, such as a lack of recent pronounced summer warming in northern Alaska and the Russian European North (Kaverin et al. 2021; Nyland et al. 2021). However, thaw propagation into ice-rich ground layers can cause surface subsidence that is not accounted for in thaw depth measurements, as manual probing obscures the relation between atmospheric climate and permafrost thaw. Widespread subsidence has been documented across northwestern Canada (O'Neill et al. 2023) and reported from a few sites in Alaska (Nyland et al. 2021), suggesting the underestimation of ice-rich permafrost thaw inferred from ALT records. Presently, the absence of standardized, long-term observations of ground surface displacement precludes the analysis of subsidence contribution to permafrost thaw at a broad geographic scale (Streletskiy et al. 2025).

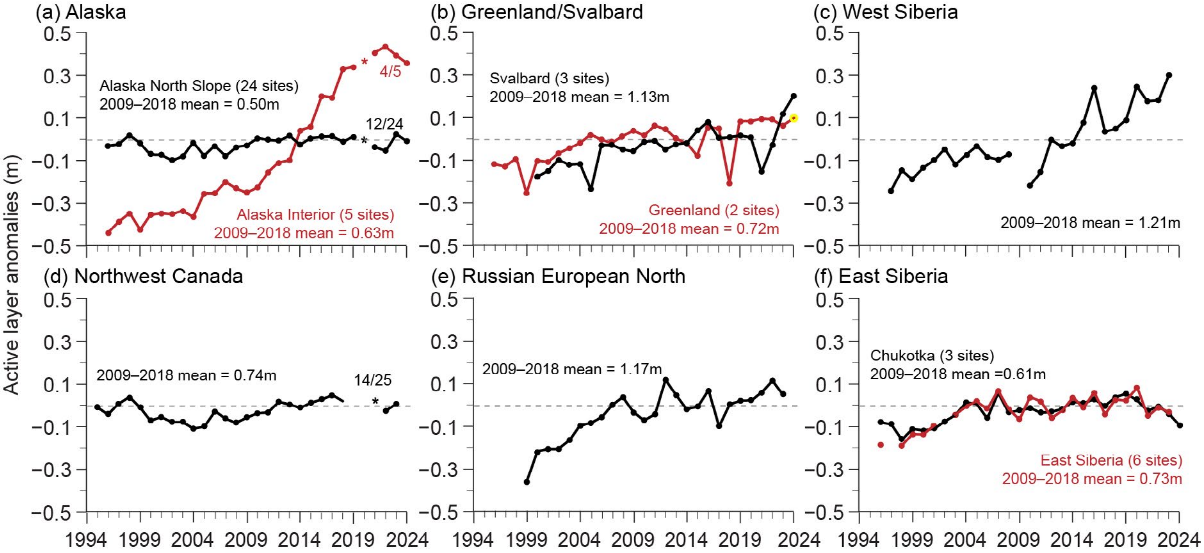

Fig. 5.29. Average annual active-layer thickness (ALT) anomalies (m), relative to the 2009–18 mean, for six Arctic regions observed by the Circumpolar Active Layer Monitoring program. Positive and negative anomalies indicate thicker or thinner ALT than the 10-year reference, respectively. Numbers of sites vary by region because only sites with >20 years of continuous thaw depth observations from the end of the thaw season are included. Asterisks represent atypical observations, for example, due to pandemic-related restrictions (fraction of sites for these years are provided on graph). Canadian ALT is derived from thaw tubes that record the maximum thaw depth over the previous year. Since Canadian sites were not visited in 2020 and 2021, the maximum thaw depth recorded during the 2022 visit could have occurred during any summer between 2019 and 2021, although the data point is plotted in 2021. Site-specific data and metadata are available at https://www2.gwu.edu/~calm/.

k. Tundra greenness

—G. V. Frost, M. J. Macander, U. S. Bhatt, L. T. Berner, J. W. Bjerke, H. E. Epstein, B. C. Forbes, G. Jia, M. J. Lara, P. M. Montesano, R. Í. Magnússon, C. S. R. Neigh, G. K. Phoenix, H. Tømmervik, C. Waigl, D. A. Walker, and D. Yang

The Arctic tundra biome occupies Earth's northernmost lands, collectively encompassing a 5.1 million km^2 region bounded by the Arctic Ocean to the north and the boreal forest biome to the south (Raynolds et al. 2019). While Arctic tundra ecosystems are treeless and lack the vertical structure of forests, they are heterogeneous across spatial scales, ranging from broad latitudinal climate gradients to landscape-scale variations in soil, hydrological, and permafrost conditions (Fig. 5.30). During past millennia, Arctic ecosystems have accumulated large amounts of carbon, as a large proportion of the carbon fixed by living plants became preserved in permafrost (Schuur et al. 2022; See et al. 2024). In recent decades, the Arctic has warmed dramatically, far exceeding the global rate of warming (section 5c) and placing the circumpolar region at the forefront of global climate and environmental change. Today, the circumpolar region lies at the crossroads of multiple feedback mechanisms that connect the living Arctic with a warming climate, declining nearshore sea ice extent, changes in seasonal snow cover, and thawing permafrost soils that contain large amounts of carbon (section 5f). Some of the most compelling evidence of broad scale changes in this remote region come from long-term satellite observations that began in 1982. By the late 1990s, Earth-observing satellites began to detect a sharp increase in the productivity of tundra vegetation, a phenomenon known today as "the greening of the Arctic."

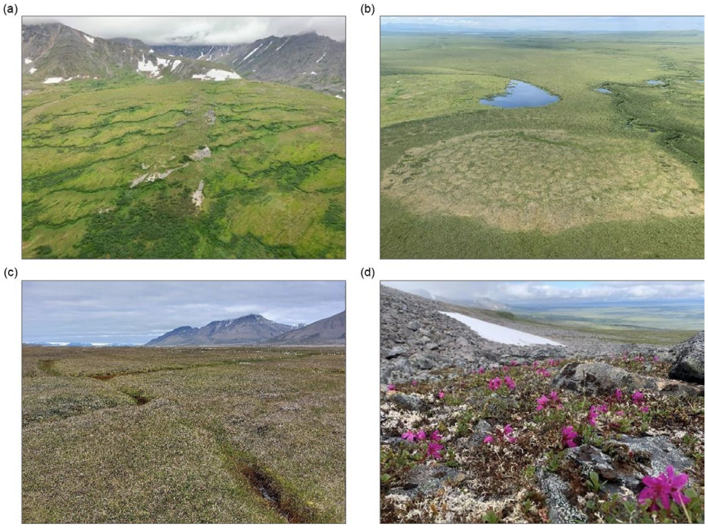

Fig. 5.30. Arctic tundra landscapes exhibit a variety of striking geomorphic landforms and vegetation patterns that arise from permafrost processes, such as (a) solifluction on hillslopes and (b) ice-wedge development in polygonal ground (both Seward Peninsula, Alaska). Many of these features are sensitive to climate warming; (c) thawing of ice-rich permafrost can lead to surface subsidence (thermokarst) and changes in soil moisture, as seen in polygonal ground in Svalbard. (d) Changes in the amount and persistence of seasonal snow can also affect the productivity and phenology of tundra vegetation.

Global vegetation has been continuously monitored from space since late 1981 by a series of satellites equipped with the Advanced Very High-Resolution Radiometer (AVHRR), providing a record that has entered its 44th year. Beginning in 2000, the circumpolar AVHRR record has been complemented by newer sensors that provide surface reflectance products with improved calibration and higher spatial resolution, including the Moderate Resolution Imaging Spectroradiometer (MODIS) and a constellation of several Landsat satellites. While both AVHRR and MODIS are nearing the end of service, continuity of these records will be maintained by Landsat and the Visible Infrared Imaging Radiometer Suite (VIIRS) sensor, first launched in 2011 (Román et al. 2024). All of these spaceborne sensors monitor global vegetation greenness using the Normalized Difference Vegetation Index (NDVI), a spectral metric that exploits the unique way in which green vegetation absorbs and reflects visible and infrared light, respectively. Here, the ongoing phenomenon of Arctic greening based on the legacy AVHRR, MODIS, and Landsat datasets is reported upon.

The long-term AVHRR NDVI dataset is the Global Inventory Modeling and Mapping Studies third generation version 1.2 dataset (GIMMS-3g+) with a spatial resolution of about 8 km (Pinzon et al. 2023). For MODIS, trends were computed by combining 16-day NDVI products from the *Terra* (MOD13A1, version 6.1) and *Aqua* (MYD13A1, version 6.1) satellites (Didan 2021a,b), referred to as MODIS MCD13A1, at a much higher spatial resolution of 500 m. Landsat provides tundra greenness data at a much higher spatial resolution of 30 m; a time series of greenness from Landsat Collection 2 (Crawford et al. 2023) was computed using the methods of Berner et al. (2023). All data were masked to the extent of the Circumpolar Arctic Vegetation Map (Raynolds et al. 2019) and exclude permanent ice and water. For all records, the annual maximum NDVI (MaxNDVI), the peak greenness value observed in midsummer (late July or early August in most of the Arctic), is summarized.

In 2024, the circumpolar average MaxNDVI value from GIMMS-3g+ was the fifth highest in the 43 years of record for that sensor, but nonetheless represented a 2.6% decline compared to 2023 (Fig. 5.31). The MODIS-observed circumpolar average MaxNDVI value in 2024 was the second highest in the 25-year record for that sensor, continuing a sequence of record or near-record values that began in 2020. Based on the MODIS record, tundra greenness reached a new record-high value in the North American Arctic, and was much higher than normal in northern Alaska, central and eastern Canada, and Greenland (Fig. 5.32). Localized areas of lower-than-normal greenness in Canada's Northwest Territories were likely the result of intense wildfire activity in 2023 and 2024. The Eurasian Arctic, however, featured a mixture of positive and negative departures from normal, a pattern that was also evident in summer 2023. Interestingly, while some of the Eurasian regions with below-normal MaxNDVI also experienced cooler-than-normal summer temperatures (e.g., the easternmost Chukchi Peninsula), others experienced very warm conditions (e.g., north-central Siberia), complicating the degree to which greening can be attributed simply to warmer summer temperatures (section 5c). Negative anomalies in northeastern Siberia could partly reflect the highly active fire season in that region. Nonetheless, the long-term trend in both AVHRR- and MODIS-observed tundra greenness is strongly positive (greening) for most of the circumpolar region (Fig. 5.33). Trends in Landsat-observed MaxNDVI are relatively subdued, but like the other legacy records, recent MaxNDVI values have exceeded the long-term average following the record-high value observed in 2020.

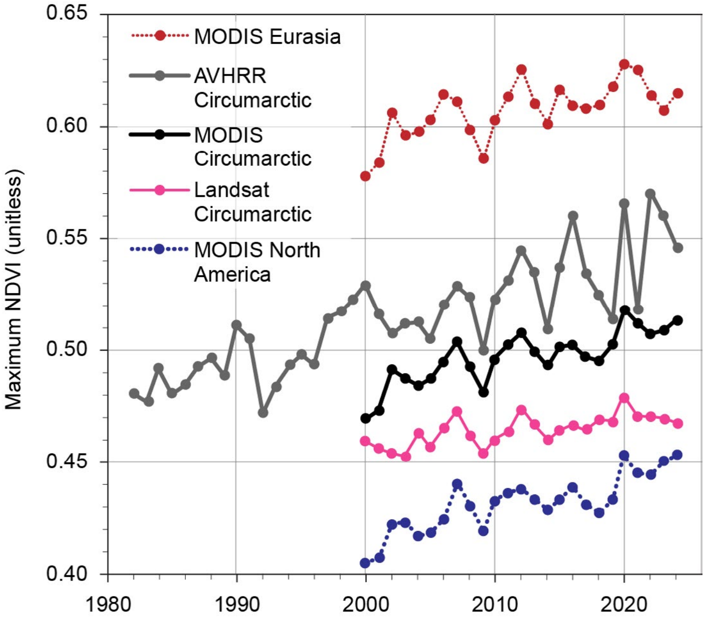

Fig. 5.31. Time series of circumpolar mean Maximum Normalized Difference Vegetation Index (MaxNDVI) from Advanced Very High-Resolution Radiometer (AVHRR) Global Inventory Modeling and Mapping Studies third generation (GIMMS-3g+; 1982–2024; gray), Moderate Resolution Imaging Spectroradiometer (MODIS) MCD13A1 (2000–2024; black), and Landsat Collection 2 (2000–23; pink). The MODIS record is further divided by continent for Arctic Eurasia (red) and North America (blue).

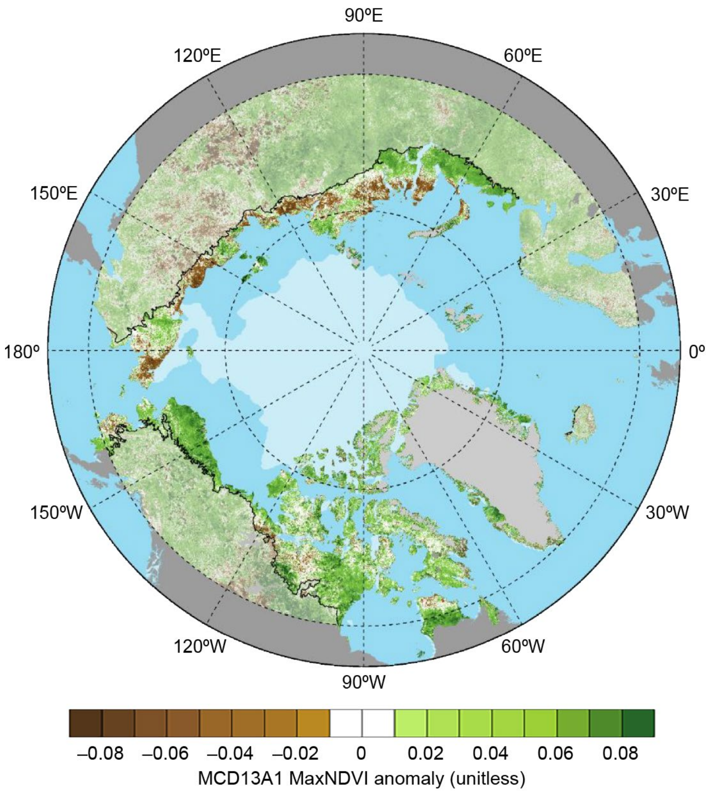

Fig. 5.32. Circumpolar Maximum Normalized Difference Vegetation Index (MaxNDVI) anomalies for the 2024 growing season relative to mean values (2000–24) for Arctic tundra (solid colors) and boreal forest (muted colors) north of 60° latitude from the Moderate Resolution Imaging Spectroradiometer (MODIS) MCD13A1 dataset. The circumpolar tree line is indicated by the black lines, and the 2024 minimum sea ice extent is indicated by light shading.

Earth-observing satellites provide foundational datasets for monitoring Arctic environmental change, and help to overcome the long-standing access barriers posed by the region's remoteness, as well as new ones arising from the Russian invasion of Ukraine (López-Blanco et al. 2024) and uncertainties in long-standing funding and logistical support for Arctic research in the United States. Nonetheless, field studies provide crucial information needed to connect spaceborne observations with patterns of change (or stability) on the ground. Increases in the abundance, distribution, and height of Arctic shrubs are a major driver of Arctic greening and have important impacts on biodiversity, surface energy balance, permafrost temperatures, and biogeochemical cycling, particularly in the Low Arctic (Mekonnen et al. 2021). However, while changes to the Arctic climate have generally favored greening, ecological disturbances, extreme events, and other causes of browning are also increasing in frequency (Parmentier et al. 2024; Phoenix et al. 2025). For example, greening trends in many parts of the Arctic have been partially offset by increasing wildfires during the past two decades, especially during 2019–21 (Zhu et al. 2024). Understanding the regional variability of complex Arctic greening trends and attributing its drivers continues to be a subject of multidisciplinary scientific research.

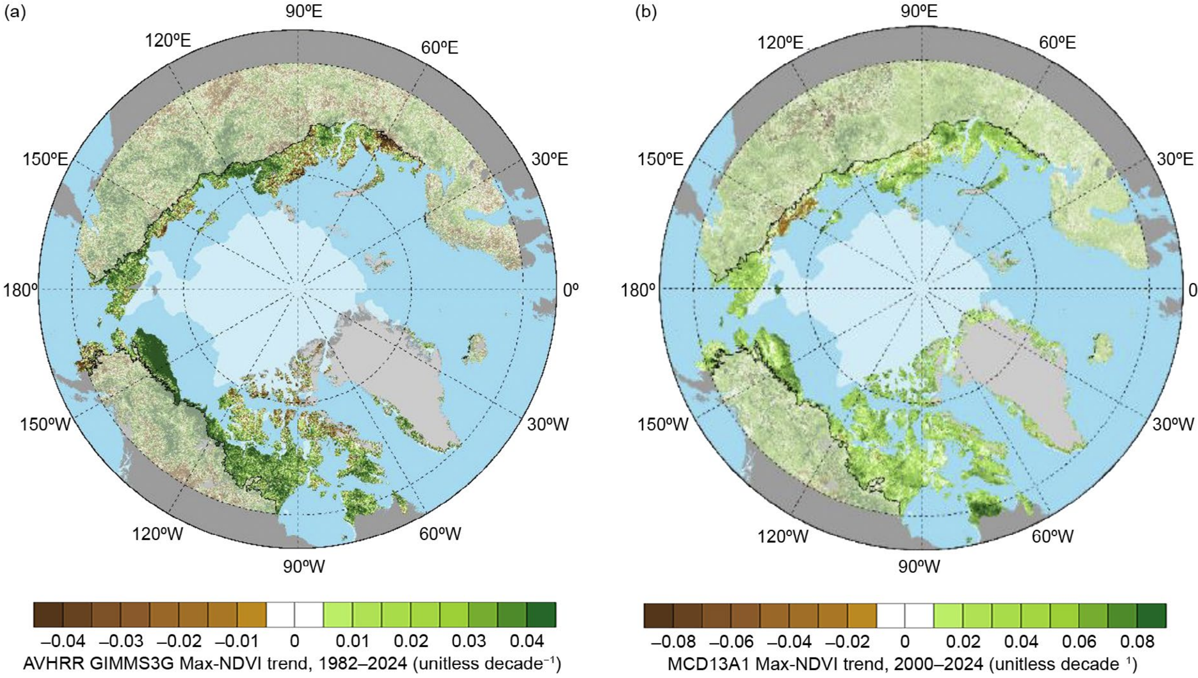

Fig. 5.33. Magnitude of the Maximum Normalized Difference Vegetation Index (MaxNDVI) trend calculated as the change decade^{-1} via ordinary least-squares regression for Arctic tundra (solid colors) and boreal forest (muted colors) north of 60° latitude during (a) 1982–2024 based on the Advanced Very High-Resolution Radiometer (AVHRR) Global Inventory Modeling and Mapping Studies third generation (GIMMS-3g+) dataset, and (b) 2000–24 based on the Moderate Resolution Imaging Spectroradiometer (MODIS) MCD13A1 dataset. The circumpolar tree line is indicated by black lines, and the 2024 minimum sea ice extent is indicated by light shading in each panel.

Acknowledgments

a. Overview

The authors and chapter editors appreciate support provided by NOAA's Global Ocean Monitoring and Observing Arctic Research Program, including content editing funded through the Cooperative Institute for Earth System Research and Data Science (CIESRDS) via NOAA Cooperative Agreement NA22OAR4320151 (M. Druckenmiller and T. Moon) and by the Cooperative Institute for Climate, Ocean, and Ecosystem Studies (CICOES) under NOAA Cooperative Agreement NA20OAR4320271 (R. Thoman).

b. Atmosphere

The authors thank the Academy of Finland for supporting ultraviolet measurements through the FARPOCC, SAARA, and CHAMPS (grant no. 329225) projects.

e. Sea surface temperature

M.-L. Timmermans acknowledges support from the National Science Foundation (NSF) Office of Polar Programs and the Office of Naval Research. Z.M. Labe acknowledges support from NOAA and its Geophysical Fluid Dynamics Laboratory (GFDL).

h. Arctic river discharge

James McClelland and coauthors acknowledge NSF support for the Arctic Great Rivers Observatory (NSF 1913888, 1914081, 1914215, 1913962, 2230812). Discharge data for the Mackenzie River are courtesy of Environment and Climate Change Canada.

Appendix 1: Acronyms

ALT	active-layer thickness
AO	Arctic Oscillation
AOI	Arctic Oscillation Index
AVHRR	Advanced Very High-Resolution Radiometer
CAA	Canadian Arctic Archipelago
CARRA	Copernicus Arctic Regional Reanalysis
CCI	Climate Change Initiative
EOF	empirical orthogonal function
ESA	European Space Administration
GBI	Greenland Blocking Index
GC-Net	Greenland Climate Network
GIMMS-3g+	Global Inventory Modeling and Mapping Studies third generation
GRACE	Gravity Recovery and Climate Experiment
GRACE-FO	Gravity Recovery and Climate Experiment Follow-On
IMS	Interactive Multisensor Snow and Ice Mapping System
MAR	Modèle Atmosphérique Régionale
MaxNDVI	Maximum Normalized Difference Vegetation Index
MODIS	Moderate Resolution Imaging Spectroradiometer
NDVI	Normalized Difference Vegetation Index
OMI	Ozone Monitoring Instrument
OMTO3	Ozone Monitoring Instrument Level-2 Total Column Ozone version 3
PCH	polar cap averaged geopotential height
PROMICE	Programme for Monitoring of the Greenland Ice Sheet
SAT	surface air temperature
SCD	snow cover duration
SCE	snow cover extent
SLP	sea level pressure
SMB	surface mass balance
SMOS	Soil Moisture Ocean Salinity
SST	sea surface temperature
SSW	sudden stratospheric warming
SWE	snow water equivalent
T_{ARCTIC}	total arctic
T_{GLOBAL}	total global
UV	ultraviolet
VIIRS	Visible Infrared Imaging Radiometer Suite

Appendix 2: Datasets and sources

Section 5b Atmosphere

Sub-section	General Variable or Phenomenon	Specific Dataset or Variable	Source
5b, 5b1, 5b2	Geopotential Height	ERA5	https://www.ecmwf.int/en/forecasts/dataset/ecmwf-reanalysis-v5
5b2	Ozone, Total Column and Stratospheric	Aura Ozone Monitoring Instrument (OMI)/ Microwave Limb Sounder (MLS)	https://disc.gsfc.nasa.gov/datasets/ML2O3_004/summary
5b2	Ozone, Total Column and Stratospheric	OMI/Aura Level-2 Total Column Ozone (OMTO3) Version 3	https://disc.gsfc.nasa.gov/datasets/OMTO3_003/summary

Section 5c Surface air temperature

Sub-section	General Variable or Phenomenon	Specific Dataset or Variable	Source
5c3	Pressure, Sea Level or Near-Surface	ERA5	https://www.ecmwf.int/en/forecasts/dataset/ecmwf-reanalysis-v5
5c2	Temperature, [Near] Surface	NASA GISTEMPv4	https://data.giss.nasa.gov/gistemp/
5c3	Temperature, [Near] Surface	ERA5	https://www.ecmwf.int/en/forecasts/dataset/ecmwf-reanalysis-v5

Section 5d Precipitation

Sub-section	General Variable or Phenomenon	Specific Dataset or Variable	Source
5d	Precipitation	ERA5	https://www.ecmwf.int/en/forecasts/dataset/ecmwf-reanalysis-v5
5d4	Precipitation	GPCC	https://opendata.dwd.de/climate_environment/GPCC/html/download_gate.html

Section 5e Sea surface temperature

Sub-section	General Variable or Phenomenon	Specific Dataset or Variable	Source
5e	Sea Surface Temperature	OISSTv2.1	https://www.ncei.noaa.gov/products/optimum-interpolation-sst

Section 5f Sea ice

Sub-section	General Variable or Phenomenon	Specific Dataset or Variable	Source
5f1	Sea Ice Extent	National Snow and Ice Data Center (NSIDC) Sea Ice Extent	https://nsidc.org/data/g02135
5f2	Sea Ice Thickness	European Space Agency (ESA) Cryosat-2/ Soil Moisture and Ocean Salinity (SMOS)	https://earth.esa.int/eogateway/catalog/smos-cryosat-l4-sea-ice-thickness
5f2	Sea Ice Thickness	NASA Ice, Cloud, and land Elevation Satellite 2 (ICESat-2)	https://icesat-2.gsfc.nasa.gov/icesat-2-data

Section 5g Greenland Ice Sheet

Sub-section	General Variable or Phenomenon	Specific Dataset or Variable	Source
5g	Air Temperature	Danish Meteorological Institute (DMI)/ Programme for Monitoring the Greenland Ice Sheet (PROMICE) Weather	https://eng.geus.dk/products-services-facilities/data-and-maps/glaciological-data-from-greenland-promice
5g	Glacier Ablation	PROMICE Glacier Front Line (Greenland)	https://doi.org/10.22008/promice/data/calving_front_lines
5g	Glacier Mass, Area or Volume	Gravity Recovery and Climate Experiment (GRACE) /GRACE Follow-On (GRACE-FO)	https://grace.jpl.nasa.gov/data/get-data/
5g	Ice Sheet Albedo	Sentinel-3 Snow and Ice Products (SICE)	https://eo4society.esa.int/projects/pre-operational-sentinel-3-snow-and-ice-products-sice/
5g	Ice Sheet Discharge	Ice Discharge (Greenland)	https://doi.org/10.22008/promice/data/ice_discharge/d/v02
5g	Ice Sheet Melt	Special Sensor Microwave Imager/Sounder (SSMIS)	https://nsidc.org/data/nsidc-0001
5g	Ice Sheet Surface-Height	Ice, Cloud, and land Elevation Satellite 2 (ICESat-2)	https://icesat-2.gsfc.nasa.gov/icesat-2-data
5g	Air Temperature	Copernicus Climate Change Service (C3S) Arctic Regional Reanalysis	https://cds.climate.copernicus.eu/datasets/reanalysis-carra-single-levels?tab=overview

Section 5h Arctic river discharge

Sub-section	General Variable or Phenomenon	Specific Dataset or Variable	Source
5h	River Discharge	Arctic Great Rivers Observatory	https//:arcticgreatrivers.org/

Section 5i Terrestrial snow cover

Sub-section	General Variable or Phenomenon	Specific Dataset or Variable	Source
5i	Snow Properties	Crocus Snowpack Model	http://www.umr-cnrm.fr/spip.php?article265
5i	Snow Properties	ERA5	https://www.ecmwf.int/en/forecasts/dataset/ecmwf-reanalysis-v5
5i	Snow Properties	MERRA-2	http://gmao.gsfc.nasa.gov/reanalysis/MERRA-2/
5i	Snow Properties	European Space Agency Snow CCI SWE	https://snow-cci.enveo.at/
5i	Snow Properties	NOAA Interactive Multi-sensor Snow and Ice Mapping System (Snow Cover Duration)	https://usicecenter.gov/Products/ImsHome
5i	Snow Properties	NOAA Snow Chart Climate Data Record	https://www.ncei.noaa.gov/products/climate-data-records/snow-cover-extent

Section 5j Permafrost

Sub-section	General Variable or Phenomenon	Specific Dataset or Variable	Source
5i1	Permafrost	Global Terrestrial Network for Permafrost (GTN-P)	http://gtnpdatabase.org/
5i1	Permafrost	Permafrost Temperature	http://permafrost.gi.alaska.edu/sites_map
5i1	Temperature, [Near] Surface	ERA5	https://www.ecmwf.int/en/forecasts/dataset/ecmwf-reanalysis-v5
5i2	Permafrost	Circumpolar Active Layer Monitoring Program (CALM) Active-Layer Thickness	https://www2.gwu.edu/~calm/

Section 5k Tundra greenness

Sub-section	General Variable or Phenomenon	Specific Dataset or Variable	Source
5k	Vegetative Index	Global Inventory Modeling and Mapping Studies third generation (GIMMS-3g+) Version 1	https://daac.ornl.gov/VEGETATION/guides/Global_Veg_Greenness_GIMMS_3G.html
5k	Vegetative Index	MODIS MCD13A1 and MYD13A1 Normalized Difference Vegetative Index (NDVI)	https://lpdaac.usgs.gov/products/mod13a1v006/
5k	Vegetative Index	Landsat Collection 2 Normalized Difference Vegetative Index (NDVI)	https://www.usgs.gov/landsat-missions/landsat-collection-2

Sidebar 5.1: North American August heat

Sub-section	General Variable or Phenomenon	Specific Dataset or Variable	Source
SB5.1	Geopotential Height	National Centers for Environmental Prediction (NCEP)/National Center for Atmospheric Research (NCAR) Reanalysis 1	https://psl.noaa.gov/data/gridded/data.ncep.reanalysis.html
SB5.1	Temperature, [Near] Surface	ERA5	https://www.ecmwf.int/en/forecasts/dataset/ecmwf-reanalysis-v5
SB5.1	Temperature, [Near] Surface	NOAA Applied Climate Information System Online Tool	https://xmacis.rcc-acis.org
SB5.1	Temperature, [Near] Surface	Environment and Climate Change Canada	https://climate.weather.gc.ca
SB5.1	Temperature, [Near] Surface	NCEP/NCAR Reanalysis 1	https://psl.noaa.gov/data/gridded/data.ncep.reanalysis.html
SB5.1	Wildfire Properties	Canadian Interagency Forest Fire Centre	https://ciffc.net/

Sidebar 5.2: Record-low sea ice conditions in the Northwest Passage in 2024

Sub-section	General Variable or Phenomenon	Specific Dataset or Variable	Source
SB5.2	Sea Ice Area	Canadian Ice Service	https://www.canada.ca/en/environment-climate-change/services/ice-forecasts-observations/latest-conditions/archive-overview.html

Sidebar 5.3: Why Greenland Ice Sheet melt was so low in 2024

Sub-section	General Variable or Phenomenon	Specific Dataset orVariable	Source
SB5.3	Geopotential Height	ERA5	https://www.ecmwf.int/en/forecasts/dataset/ecmwf-reanalysis-v5
SB5.3	Teleconnections	Arctic Oscillation Index	https://www.cpc.ncep.noaa.gov/products/precip/CWlink/daily_ao_index/ao.shtml
SB5.3	Winds, Upper Air	ERA5	https://www.ecmwf.int/en/forecasts/dataset/ecmwf-reanalysis-v5

References

AghaKouchak, A., and Coauthors, 2020: Climate extremes and compound hazards in a warming world. *Annu. Rev. Earth Planet. Sci.*, **48**, 519–548, https://doi.org/10.1146/annurev-earth-071719-055228.

Arctic Council, 2024: An archipelago in transformation: Climate scientist Ketil Isaksen on record-breaking changes on Svalbard. Arctic Council, accessed 13 February 2025, https://arctic-council.org/news/an-archipelago-in-transformation-climate-scientist-ketil-isaksen-on-record-breaking-changes-on-svalbard/.

Baldwin, M. P., and Coauthors, 2021: Sudden stratospheric warmings. *Rev. Geophys.*, **59**, e2020RG000708, https://doi.org/10.1029/2020RG000708.

Barrett, A. P., J. C. Stroeve, and M. C. Serreze, 2020: Arctic Ocean precipitation from atmospheric reanalyses and comparisons with North Pole drifting stations. *J. Geophys. Res. Oceans*, **125**, e2019JC015415, https://doi.org/10.1029/2019JC015415.

Becker, A., P. Finger, A. Meyer-Christoffer, B. Rudolf, K. Schamm, U. Schneider, and M. Ziese, 2013: A description of the global land-surface precipitation data products of the Global Precipitation Climatology Centre with sample applications including centennial (trend) analysis from 1901–present. *Earth Syst. Sci. Data*, **5**, 71–99, https://doi.org/10.5194/essd-5-71-2013.

Benestad, R., and Coauthors, 2023: Extreme weather and climate events in 2022 [in "State of the Climate in 2022"]. *Bull. Amer. Meteor. Soc.*, **104** (8), S15–S17, https://doi.org/10.1175/BAMS-D-23-0079.1.

Berner, L. T., J. J. Assmann, S. Normand, and S. J. Goetz, 2023: 'LandsatTS': an R package to facilitate retrieval, cleaning, cross-calibration, and phenological modeling of Landsat time series data. *Ecography*, **2023**, e06768, https://doi.org/10.1111/ecog.06768.

Bernhard, G., and Coauthors, 2015: Comparison of OMI UV observations with ground-based measurements at high northern latitudes. *Atmos. Chem. Phys.*, **15**, 7391–7412, https://doi.org/10.5194/acp-15-7391-2015.

Bhartia, P. K., and C. W. Wellemeyer, 2002: TOMS-V8 total O3 algorithm. OMI Algorithm Theoretical Basis Document Volume II. NASA Goddard Space Flight Center Tech. Doc. ATBD-OMI-02, 91 pp., https://eospso.gsfc.nasa.gov/sites/default/files/atbd/ATBD-OMI-02.pdf.

Bigalke, S., and J. E. Walsh, 2022: Future changes of snow in Alaska and the Arctic under stabilized global warming scenarios. *Atmosphere*, **13**, 541, https://doi.org/10.3390/atmos13040541.

Box, J. E., and Coauthors, 2019: Key indicators of Arctic climate change: 1971–2017. *Environ. Res. Lett.*, **14**, 045010, https://doi.org/10.1088/1748-9326/aafc1b.

——, and Coauthors, 2021: Recent developments in Arctic climate observation indicators. AMAP Arctic Climate Change Update 2021: Key Trends and Impacts, Arctic Monitoring and Assessment Programme, 7–29, https://www.amap.no/documents/doc/amap-arctic-climate-change-update-2021-key-trends-and-impacts/3594.

Brown, R., and Coauthors, 2017: Arctic terrestrial snow cover. Snow, Water, Ice and Permafrost in the Arctic (SWIPA) 2017, Arctic Monitoring and Assessment Programme (AMAP), 25–64, https://www.amap.no/documents/doc/snow-water-ice-and-permafrost-in-the-arctic-swipa-2017/1610.

Cheng, V. Y. S., F. Wu, M. Beauchemin, and L. Chisholm, 2024: Canada [in "State of the Climate in 2023"]. *Bull. Amer. Meteor. Soc.*, **105** (8), S380–S382, https://doi.org/10.1175/2024BAMSStateoftheClimate_Chapter7.1.

CIFFC, 2025: Canadian Interagency Forest Fire Centre. Accessed 5 February 2025, https://ciffc.net/.

Cohen, J., and Coauthors, 2020: Divergent consensuses on Arctic amplification influence on midlatitude severe winter weather. *Nat. Climate Change*, **10**, 20–29, https://doi.org/10.1038/s41558-019-0662-y.

Colgan, W., and Coauthors, 2015: Hybrid glacier Inventory, Gravimetry and Altimetry (HIGA) mass balance product for Greenland and the Canadian Arctic. *Remote Sens. Environ.*, **168**, 24–39, https://doi.org/10.1016/j.rse.2015.06.016.

Cook, A. J., J. Dawson, S. E. L. Howell, J. E. Holloway, and M. Brady, 2024: Sea ice choke points reduce the length of the shipping season in the Northwest Passage. *Commun. Earth Environ.*, **5**, 362, https://doi.org/10.1038/s43247-024-01477-6.

Crawford, A. D., and M. C. Serreze, 2016: Does the summer Arctic frontal zone influence Arctic Ocean cyclone activity? *J. Climate*, **29**, 4977–4993, https://doi.org/10.1175/JCLI-D-15-0755.1.

Crawford, C. J., and Coauthors, 2023: The 50-year Landsat collection 2 archive. *Sci. Remote Sens.*, **8**, 100103, https://doi.org/10.1016/j.srs.2023.100103.

Dai, A., D. Luo, M. Song, and J. Liu, 2019: Arctic amplification is caused by sea-ice loss under increasing CO_2. *Nat. Commun.*, **10**, 121, https://doi.org/10.1038/s41467-018-07954-9.

Decharme, B., A. Barbu, and S. R. Buarque, 2024: Crocus-ERA5 daily snow product over the Northern Hemisphere at 0.25° resolution, 2023v2. Zenodo, accessed 3 September 2024, https://doi.org/10.5281/zenodo.14513248.

Delhasse, A., E. Hanna, C. Kittel, and X. Fettweis, 2021: Brief communication: CMIP6 does not suggest any atmospheric blocking increase in summer over Greenland by 2100. *Int. J. Climatol.*, **41**, 2589–2596, https://doi.org/10.1002/joc.6977.

Derksen, C., and L. Mudryk, 2023: Assessment of Arctic seasonal snow cover rates of change. *Cryosphere*, **17**, 1431–1443, https://doi.org/10.5194/tc-17-1431-2023.

Didan, K., 2021a: MODIS/Terra vegetation indices 16-day L3 global 500m SIN grid V061. Accessed 19 May 2025, https://doi.org/10.5067/MODIS/MOD13A1.061.

——, 2021b: MODIS/Aqua vegetation indices 16-day L3 global 500m SIN grid V061. Accessed 19 May 2025, https://doi.org/10.5067/MODIS/MYD13A1.061.

Dou, T., and Coauthors, 2021: Trends and spatial variation in rain-on-snow events over the Arctic Ocean during the early melt season. *Cryosphere*, **15**, 883–895, https://doi.org/10.5194/tc-15-883-2021.

Durocher, M., A. I. Requena, D. H. Burn, and J. Pellerin, 2019: Analysis of trends in annual streamflow to the Arctic Ocean. *Hydrol. Processes*, **33**, 1143–1151, https://doi.org/10.1002/hyp.13392.

ESA, 2023: European Space Agency SMOS-CryoSat L4 sea ice thickness, version 206. Accessed 1 September 2024, https://doi.org/10.57780/sm1-4f787c3.

Fausto, R. S., and Coauthors, 2021: Programme for Monitoring of the Greenland Ice Sheet (PROMICE) automatic weather station data. *Earth Syst. Sci. Data*, **13**, 3819–3845, https://doi.org/10.5194/essd-13-3819-2021.

Fetterer, F., K. Knowles, W. N. Meier, M. Savoie, and A. K. Windnagel, 2017: Sea Ice Index, version 3 (updated daily). National Snow and Ice Data Center, accessed 4 October 2024, https://doi.org/10.7265/N5K072F8.

Fettweis, X., and Coauthors, 2020: GrSMBMIP: Intercomparison of the modelled 1980–2012 surface mass balance over the Greenland Ice Sheet. *Cryosphere*, **14**, 3935–3958, https://doi.org/10.5194/tc-14-3935-2020.

Fol, M., B. Tremblay, S., Pfirman, R. Newton, S. Howell, and J.-F. Lemieux, 2025: Revisiting the Last Ice Area projections from a high-resolution Global Earth System Model. *Commun. Earth Environ.*, **6**, 46, https://doi.org/10.1038/s43247-025-02034-5

Gardner, A. S., N.-J. Schlegel, and E. Larour, 2023: Glacier Energy and Mass Balance (GEMB): A model of firn processes for cryosphere research. *Geosci. Model Dev.*, **16**, 2277–2302, https://doi.org/10.5194/gmd-16-2277-2023.

Gelaro, R., and Coauthors, 2017: The Modern-Era Retrospective Analysis for Research and Applications, version 2 (MERRA-2). *J. Climate*, **30**, 5419–5454, https://doi.org/10.1175/JCLI-D-16-0758.1.

GMAO, 2015: MERRA-2tavg1_2d_lnd_Nx:2d, 1-hourly, time-averaged, single-level, assimilation, land surface diagnostics V5.12.4. Goddard Earth Sciences Data and Information Services Center, accessed 3 August 2024, https://doi.org/10.5067/RKPHT8KC1Y1T.

Government of Northwest Territories, 2025: *NWT Water Monitoring Bulletin*—June 9, 2025. Tech. Data, 31 pp., https://www.gov.nt.ca/ecc/en/newsroom/nwt-water-monitoring-bulletin-january-17-2025.

Hanna, E., T. E. Cropper, R. J. Hall, and J. Cappelen, 2016: Greenland Blocking Index 1851–2015: A regional climate change signal. *Int. J. Climatol.*, **36**, 4847–4861, https://doi.org/10.1002/joc.4673.

He, S., H. Drange, T. Furevik, H. Wang, K. Fan, L. S. Graff, and Y. J. Orsolini, 2024: Relative impacts of sea ice loss and atmospheric internal variability on the winter Arctic to East Asian surface air temperature based on large-ensemble simulations with NorESM2. *Adv. Atmos. Sci.*, **41**, 1511–1526, https://doi.org/10.1007/s00376-023-3006-9.

Hersbach, H., and Coauthors, 2020: The ERA5 global reanalysis. *Quart. J. Roy. Meteor. Soc.*, **146**, 1999–2049, https://doi.org/10.1002/qj.3803.

Hjort, J., D. Streletskiy, G. Doré, Q. Wu, K. Bjella, and M. Luoto, 2022: Impacts of permafrost degradation on infrastructure. *Nat. Rev. Earth Environ.*, **3**, 24–38, https://doi.org/10.1038/s43017-021-00247-8.

Holmes, R. M., and Coauthors, 2013: Climate change impacts on the hydrology and biogeochemistry of Arctic rivers. *Climactic Change and Global Warming of Inland Waters: Impacts and Mitigation for Ecosystems and Societies*, C. R. Goldman, M. Kumagai, and R. D. Robarts, Eds., Wiley, 3–26.

Howell, S. E. L., C. R. Duguay, and T. Markus, 2009: Sea ice conditions and melt season duration variability within the Canadian Arctic Archipelago: 1979–2008. *Geophys. Res. Lett.*, **36**, L10502, https://doi.org/10.1029/2009GL037681.

——, T. Wohlleben, A. Komarov, L. Pizzolato, and C. Derksen, 2013: Recent extreme light sea ice years in the Canadian Arctic Archipelago: 2011 and 2012 eclipse 1998 and 2007. *Cryosphere*, **7**, 1753–1768, https://doi.org/10.5194/tc-7-1753-2013.

——., D. G. Babb, J. C. Landy, and M. Brady, 2023: Multi-year sea ice conditions in the Northwest Passage: 1968–2020. *Atmos.–Ocean*, **61**, 202–216, https://doi.org/10.1080/07055900.2022.2136061.

——, ——, ——, I. A. Glissenaar, K. McNeil, B. Montpetit, and M. Brady, 2024: Sea ice transport and replenishment across and within the Canadian Arctic Archipelago, 2016–2022. *Cryosphere*, **18**, 2321–2333, https://doi.org/10.5194/tc-18-2321-2024.

Huang, B., C. Liu, V. Banzon, E. Freeman, G. Graham, B. Hankins, T. Smith, and H. Zhang, 2021: Improvements of the Daily Optimum Interpolation Sea Surface Temperature (DOISST) version 2.1. *J. Climate*, **34**, 2923–2939, https://doi.org/10.1175/JCLI-D-20-0166.1.

Isaksen, K., J. Lutz, A. M. Sorensen, O. Godoy, L. Ferrighi, S. Eastwood, and S. Aaboe, 2022: Advances in operational permafrost monitoring on Svalbard and in Norway. *Environ. Res. Lett.*, **17**, 095012, https://doi.org/10.1088/1748-9326/ac8e1c.

Ivanova, N., O. M. Johannessen, L. T. Pedersen, and R. T. Tonboe, 2014: Retrieval of Arctic sea ice parameters by satellite passive microwave sensors: A comparison of eleven sea ice concentration algorithms. *IEEE Trans. Geosci. Remote Sens.*, **52**, 7233–7246, https://doi.org/10.1109/TGRS.2014.2310136.

Jahn, A., M. M. Holland, and J. E. Kay, 2024: Projections of an ice-free Arctic Ocean. *Nat. Rev. Earth Environ.*, **5**, 164–176, https://doi.org/10.1038/s43017-023-00515-9.

Jain, P., and Coauthors, 2024: Drivers and impacts of the record-breaking 2023 wildfire season in Canada. *Nat. Commun.*, **15**, 6764, https://doi.org/10.1038/s41467-024-51154-7.

Kalnay, E., and Coauthors, 1996: The NCEP/NCAR 40-Year Reanalysis Project. *Bull. Amer. Meteor. Soc.*, **77**, 437–471, https://doi.org/10.1175/1520-0477(1996)077<0437:TNYRP>2.0.CO;2.

Karlsson, N. B., and Coauthors, 2021: A first constraint on basal melt-water production of the Greenland ice sheet. *Nat Commun.*, **12**, 3461, https://doi.org/10.1038/s41467-021-23739-z.

Kaverin, D., and Coauthors, 2021: Long-term active layer monitoring at CALM sites in the Russian European North. *Polar Geogr.*, **44**, 203–216, https://doi.org/10.1080/1088937X.2021.1981476.

Kopec, B., X. Feng, F. A. Michel, and E. Posmentier, 2016: Influence of sea ice on Arctic precipitation. *Proc. Natl. Acad. Sci. USA*, **113**, 46–51, https://doi.org/10.1073/pnas.1504633113.

Lavergne, T. and Coauthors, 2019: Version 2 of the EUMETSAT OSI SAF and ESA CCI sea-ice concentration climate data records, *Cryosphere*, **13**, 49–78, https://doi.org/10.5194/tc-13-49-2019.

Lee, S. H., A. H. Butler, and G. L. Manney, 2025: Two major sudden stratospheric warmings during winter 2023/2024. *Weather*, **80**, 45–53, https://doi.org/10.1002/wea.7656.

L'Heureux, M., A. H. Butler, B. Jha, A. Kumar, and W. Wang, 2010: Unusual extremes in the negative phase of the Arctic Oscillation during 2009. *Geophys. Res. Lett.*, **37**, L10704, https://doi.org/10.1029/2010GL043338.

Loeb, N. A., A. Crawford, J. C. Stroeve, and J. Hanesiak, 2022: Extreme precipitation in the eastern Canadian Arctic and Greenland: An evaluation of atmospheric reanalyses. *Front. Environ. Sci.*, **10**, 866929, https://doi.org/10.3389/fenvs.2022.866929.

López-Blanco, E., and Coauthors, 2024: Towards an increasingly biased view on Arctic change. *Nat. Clim. Chang.*, **14**, 152–155, https://doi.org/10.1038/s41558-023-01903-1.

Luojus, K., and Coauthors, 2022: ESA Snow Climate Change Initiative (Snow_cci): Snow Water Equivalent (SWE) level 3C daily global climate research data package (CRDP) (1979–2020), version 2.0. NERC EDS Centre for Environmental Data Analysis, accessed 3 September 2024, https://doi.org/10.5285/4647c-c9ad3c044439d6c643208d3c494.

Mankoff, K. D., A. Solgaard, W. Colgan, A. P. Ahlstrøm, S. A. Khan, and R. S. Fausto, 2020: Greenland Ice Sheet solid ice discharge from 1986 through March 2020. *Earth Syst. Sci. Data*, **12**, 1367–1383, https://doi.org/10.5194/essd-12-1367-2020.

——, and Coauthors, 2021: Greenland Ice Sheet mass balance from 1840 through next week. *Earth Syst. Sci. Data*, **13**, 5001–5025, https://doi.org/10.5194/essd-13-5001-2021.

McClelland, J. W., R. M. Holmes, K. H. Dunton, and R. Macdonald, 2012: The Arctic Ocean estuary. *Estuaries Coasts*, **35**, 353–368, https://doi.org/10.1007/s12237-010-9357-3.

McCrystall, M., J. Stroeve, M. C. Serreze, B. C. Forbes, and J. Screen, 2021: New climate models reveal faster and larger increases in Arctic precipitation than previously projected. *Nat. Commun.*, **12**, 6765, https://doi.org/10.1038/s41467-021-27031-y.

Medley, B., T. A. Neumann, H. J. Zwally, B. E. Smith, and C. M. Stevens, 2022: Simulations of firn processes over the Greenland and Antarctic ice sheets: 1980–2021. *Cryosphere*, **16**, 3971–4011, https://doi.org/10.5194/tc-16-3971-2022.

Meier, W. N., F. Fetterer, A. K. Windnagel, and J. S. Stewart, 2021a: NOAA/NSIDC climate data record of passive microwave sea ice concentration, version 4. [1982-2021]. National Snow and Ice Data Center, accessed 2 February 2025, https://doi.org/10.7265/efmz-2t65.

——, ——, ——, and ——, 2021b: Near-real-time NOAA/NSIDC climate data record of passive microwave sea ice concentration, version 2 [1982–2021]. Accessed 2 February 2025, https://doi.org/10.7265/tgam-yv28.

Mekonnen, Z. A., and Coauthors, 2021: Arctic tundra shrubification: A review of mechanisms and impacts on ecosystem carbon balance. *Environ. Res. Lett.*, **16**, 053001, https://doi.org/10.1088/1748-9326/abf28b.

Melling, H., 2002: Sea ice of the northern Canadian Arctic Archipelago. *J. Geophys. Res.*, **107**, 3181, https://doi.org/10.1029/2001JC001102.

Meredith, M., and Coauthors, 2019: Polar regions. The Ocean and Cryosphere in a Changing Climate, H.-O. Pörtner et al., Eds., Cambridge University Press, 203–320, https://doi.org/10.1017/9781009157964.005.

Miner, K. R., and Coauthors, 2022: Permafrost carbon emissions in a changing Arctic. *Nat. Rev. Earth Environ.*, **3**, 55–67, https://doi.org/10.1038/s43017-021-00230-3.

Mortimer, C., L. Mudryk, C. Derksen, K. Luojus, R. Brown, R. Kelly, and M. Tedesco, 2020: Evaluation of long-term Northern Hemisphere snow water equivalent products. *Cryosphere*, **14**, 1579–1594, https://doi.org/10.5194/tc-14-1579-2020.

Mote, T., 2007: Greenland surface melt trends 1973–2007: Evidence of a large increase in 2007. *Geophys. Res. Lett.*, **34**, L22507, https://doi.org/10.1029/2007GL031976.

Mouginot, J., and Coauthors, 2019: Forty-six years of Greenland Ice Sheet mass balance from 1972 to 2018. *Proc. Natl. Acad. Sci. USA*, **116**, 9239–9244, https://doi.org/10.1073/pnas.1904242116.

Mudryk, L. R., J. Dawson, S. E. L. Howell, C. Derksen, T. A. Zagon, and M. Brady, 2021: Impact of 1, 2 and 4°C of global warming on ship navigation in the Canadian Arctic. *Nat. Climate Change*, **11**, 673–679, https://doi.org/10.1038/s41558-021-01087-6.

Muñoz Sabater, J., 2019: ERA5-Land hourly data from 1950 to present. Copernicus Climate Change Service (C3S) Climate Data Store (CDS), accessed 3 September 2024, https://doi.org/10.24381/cds.e2161bac.

NASA, 2024: Svalbard melts. Accessed 13 February 2024, https://earthobservatory.nasa.gov/images/153189/svalbard-melts.

Natali, S. M., and Coauthors, 2024: Arctic terrestrial carbon cycling. Arctic Report Card 2024, T. A. Moon, M. L. Druckenmiller, and R. L. Thoman, Eds., NOAA Tech. Rep. OAR ARC 24-11, 8 pp., https://doi.org/10.25923/0GPP-MN10.

NCEP, 2025: Arctic Oscillation Index. Accessed 13 February 2025, https://www.cpc.ncep.noaa.gov/products/precip/CWlink/daily_ao_index/ao.shtml.

Newman, P. A., L. R. Lait, N. A. Kramarova, L. Coy, S. M. Frith, L. D. Oman, and S. S. Dhomse, 2024: Record high March 2024 Arctic total column ozone. *Geophys. Res. Lett.*, **51**, e2024GL110924, https://doi.org/10.1029/2024GL110924.

Notz, D., and SIMIP Community, 2020: Arctic sea ice in CMIP6. *Geophys. Res. Lett.*, **47**, e2019GL086749, https://doi.org/10.1029/2019GL086749.

Nyland, K. E., N. I. Shiklomanov, D. A. Streletskiy, F. E. Nelson, A. E. Klene, and A. L. Kholodov, 2021: Long-term Circumpolar Active Layer Monitoring (CALM) program observations in Northern Alaskan tundra. *Polar Geogr.*, **44**, 167–185, https://doi.org/10.1080/1088937X.2021.1988000.

O'Neill, H. B., S. L. Smith, C. R. Burn, C. Duchesne, and Y. Zhang, 2023: Widespread permafrost degradation and thaw subsidence in northwest Canada. *J. Geophys. Res. Earth Surf.*, **128**, e2023JF007262, https://doi.org/10.1029/2023JF007262.

Overland, J. E., 2024: Emergence of Arctic extremes. *Climate*, **12**, 109, https://doi.org/10.3390/cli12080109.

Park, H. J., and J. B. Ahn, 2016: Combined effect of the Arctic Oscillation and the western Pacific pattern on East Asia winter temperature. *Climate Dyn.*, **46**, 3205–3221, https://doi.org/10.1007/s00382-015-2763-2.

Parmentier, F.-J. W., and Coauthors, 2024: Rapid ice-wedge collapse and permafrost carbon loss triggered by increased snow depth and surface runoff. *Geophys. Res. Let.*, **51**, e2023GL108020, https://doi.org/10.1029/2023GL108020.

Peng, G., W. N. Meier, D. J. Scott, and M. H. Savoie, 2013: A long-term and reproducible passive microwave sea ice concentration data record for climate studies and monitoring. *Earth Syst. Sci. Data*, **5**, 311–318, https://doi.org/10.5194/essd-5-311-2013.

Peterson, B. J., R. M. Holmes, J. W. McClelland, C. J. Vörösmarty, R. B. Lammers, A. I. Shiklomanov, I. A. Shiklomanov, and S. Rahmstorf, 2002: Increasing river discharge to the Arctic Ocean. *Science*, **298**, 2171–2173, https://doi.org/10.1126/science.1077445.

Petty, A. A., N. T. Kurtz, R. Kwok, T. Markus, and T. A. Neumann, 2020: Winter Arctic sea ice thickness from ICESat-2 freeboards. *J. Geophys. Res. Oceans*, **125**, e2019JC015764, https://doi.org/10.1029/2019JC015764.

——, N. Keeney, A. Cabaj, P. Kushner, and M. Bagnardi, 2023a: Winter Arctic sea ice thickness from ICESat-2: Upgrades to freeboard and snow loading estimates and an assessment of the first three winters of data collection. *Cryosphere*, **17**, 127–156, https://doi.org/10.5194/tc-17-127-2023.

——, N. Kurtz, R. Kwok, T. Markus, T. A. Neumann, and N. Keeney, 2023b: ICESat-2 L4 monthly gridded sea ice thickness, version 3. NASA National Snow and Ice Data Center Distributed Active Archive Center, accessed 1 September 2024, https://doi.org/10.5067/ZCSU8Y5U1BQW.

Phoenix, G. K., and Coauthors, 2025: Browning events in Arctic ecosystems: Diverse causes with common consequences. *PLOS Climate*, **4**, e0000570, https://doi.org/10.1371/journal.pclm.0000570.

Pinzon, J. E., C. J. Tucker, U. S. Bhatt, G. V. Frost, and M. J. Macander, 2023: Global Vegetation Greenness (NDVI) from AVHRR GIMMS-3G+, 1981-2022. Accessed 19 May 2025, https://doi.org/10.3334/ORNLDAAC/2187.

Polyakov, I. V., T. J. Ballinger, R. Lader, and X. Zhang, 2024: Modulated trends in Arctic surface air temperature extremes as a fingerprint of climate change. *J. Climate*, **37**, 2381–2404, https://doi.org/10.1175/JCLI-D-23-0266.1.

Qian, L., J. Rao, R. Ren, C. Shi, and S. Liu, 2024: Enhanced stratosphere-troposphere and tropics-Arctic couplings in the 2023/24 winter. *Commun. Earth Environ.*, **5**, 631, https://doi.org/10.1038/s43247-024-01812-x.

Rawlins, M. A., and Coauthors, 2010: Analysis of the arctic system freshwater cycle intensification: Observations and expectations. *J. Climate*, **23**, 5715–5737, https://doi.org/10.1175/2010JCLI3421.1.

Raynolds, M. K., and Coauthors, 2019: A raster version of the Circumpolar Arctic Vegetation Map (CAVM). Remote Sens. *Environ.*, **232**, 111297, https://doi.org/10.1016/j.rse.2019.111297.

Reynolds, R. W., N. A. Rayner, T. M. Smith, D. C. Stokes, and W. Wang, 2002: An improved in situ and satellite SST analysis for climate. *J. Climate*, **15**, 1609–1625, https://doi.org/10.1175/1520-0442(2002)015<1609:AIISAS>2.0.CO;2.

——, T. M. Smith, C. Liu, D. B. Chelton, K. S. Casey, and M. G. Schlax, 2007: Daily high-resolution-blended analyses for sea surface temperature. *J. Climate*, **20**, 5473–5496, https://doi.org/10.1175/2007JCLI1824.1.

Ricker, R., S. Hendricks, L. Kaleschke, X. Tian-Kunze, J. King, and C. Haas, 2017: A weekly Arctic sea-ice thickness data record from merged CryoSat-2 and SMOS satellite data. *Cryosphere*, **11**, 1607–1623, https://doi.org/10.5194/tc-11-1607-2017.

Robinson, D. A., T. W. Estilow, and NOAA CDR Program, 2012: NOAA Climate Data Record (CDR) of Northern Hemisphere (NH) Snow Cover Extent (SCE), version 1. NOAA National Centers for Environmental Information, accessed 3 September 2024, https://doi.org/10.7289/V5N014G9.

Román, M. O., and Coauthors, 2024: Continuity between NASA MODIS Collection 6.1 and VIIRS Collection 2 land products. *Remote Sens. Environ.*, **302**, 113963, https://doi.org/10.1016/j.rse.2023.113963.

Romanovsky, V., and Coauthors, 2017: Changing permafrost and its impacts. Snow, Water, Ice and Permafrost in the Arctic (SWIPA) 2017, Arctic Monitoring and Assessment Program (AMAP), 65–102, https://www.amap.no/documents/doc/snow-water-ice-and-permafrost-in-the-arctic-swipa-2017/1610.

Schneider, U., P. Finger, E. Rustemeier, M. Ziese, and S. Hänsel, 2022: Global precipitation analysis products of the GPCC. 17 pp., https://opendata.dwd.de/climate_environment/GPCC/PDF/GPCC_intro_products_v2022.pdf.

Schuur, E. A. G., and Coauthors, 2022: Permafrost and climate change: Carbon cycle feedbacks from the warming Arctic. *Annu. Rev. Environ. Resour.*, **47**, 343–371, https://doi.org/10.1146/annurev-environ-012220-011847.

Schyberg H., and Coauthors, 2020: Arctic regional reanalysis on single levels from 1991 to present. Copernicus Climate Change Service (C3S) Climate Data Store (CDS), accessed 26 March 2025, https://doi.org/10.24381/cds.713858f6

See, C. R., and Coauthors, 2024: Decadal increases in carbon uptake offset by respiratory losses across northern permafrost ecosystems. *Nat. Clim. Chang.*, **14**, 853–862, https://doi.org/10.1038/s41558-024-02057-4.

Serreze, M. C., M. P. Clark, and D. H. Bromwich, 2003: Monitoring precipitation over the Arctic terrestrial drainage system: Data requirements, shortcomings, and applications of atmospheric reanalysis. *J. Hydrometeor.*, **4**, 387–407, https://doi.org/10.1175/1525-7541(2003)4<387:MPOTAT>2.0.CO;2.

——, S. Bigalke, R. Lader, T. J. Ballinger, and J. E. Walsh, 2024: Precipitation [in "State of the Climate in 2023"]. *Bull. Amer. Meteor. Soc.*, **105** (8), S295–S297, https://doi.org/10.1175/BAMS-D-24-0101.1.

Shrestha, R. R., K. E. Bennett, D. L. Peters, and D. Yang, 2021: Hydrologic extremes in Arctic rivers and regions: Historical variability and future perspectives. *Arctic Hydrology, Permafrost and Ecosystems*, D. Yang and D. L. Kane, Eds., Springer Nature Switzerland, 187–218, https://doi.org/10.1007/978-3-030-50930-9_7.

Sigmond, M., J. C. Fyfe, and N. C. Swart, 2018: Ice-free Arctic projections under the Paris Agreement. *Nat. Climate Change*, **8**, 404–408, https://doi.org/10.1038/s41558-018-0124-y.

Smith, B., and Coauthors, 2023: ATLAS/ICESat-2 L3B gridded Antarctic and Arctic land ice height change, version 3. NASA National Snow and Ice Data Center Distributed Active Archive Center, accessed 7 February 2025, https://doi.org/10.5067/ATLAS/ATL15.003.

Smith, S. L., H. B. O'Neill, K. Isaksen, J. Noetzli, and V. E. Romanovsky, 2022: The changing thermal state of permafrost. *Nat. Rev. Earth Environ.*, **3**, 10–23, https://doi.org/10.1038/s43017-021-00240-1.

——, V. E. Romanovsky, K. Isaksen, K. Nyland, N. I. Shiklomanov, D. A. Streletskiy, and H. H. Christiansen, 2024a: Permafrost [in "State of the Climate in 2023"]. *Bull. Amer. Meteor. Soc.*, **105** (8), S314–S317, https://doi.org/10.1175/BAMS-D-24-0101.1.

——, C. Duchesne, and H. B. O'Neill, 2024b: Long-term permafrost monitoring in Northern Canada—What have we learned? 12th Int. Conf. on Permafrost, Whitehorse, YT, Canada, International Permafrost Association, 398–404, https://doi.org/10.52381/ICOP2024.84.1.

Streletskiy, D. A., and Coauthors, 2025: Thawing permafrost is subsiding in the Northern Hemisphere—Review and perspectives. *Environ. Res. Lett.*, **20**, 013006, https://doi.org/10.1088/1748-9326/ada2ff.

Sweeney, A. J., Q. Fu, S. Po-Chedley, H. Wang, and M. Wang, 2023: Internal variability increased Arctic amplification during 1980–2022. *Geophys. Res. Lett.*, **50**, e2023GL106060, https://doi.org/10.1029/2023GL106060.

Tank, S. E., and Coauthors, 2023: Recent trends in the chemistry of major northern rivers signal widespread Arctic change. *Nat. Geosci.*, **16**, 789–796, https://doi.org/10.1038/s41561-023-01247-7.

Tapley, B. D., and Coauthors, 2019: Contributions of GRACE to understanding climate change. *Nat. Climate Change*, **5**, 358–369, https://doi.org/10.1038/s41558-019-0456-2.

Taylor, P. C., and Coauthors, 2022: Process drivers, inter-model spread, and the path forward: A review of amplified Arctic warming. *Front. Earth Sci.*, **9**, 758361, https://doi.org/10.3389/feart.2021.758361.

Thoman, R. L., M. Brubaker, M. Heata, and J. Jeuring, 2024: Summer 2023 weather and climate impacts [in "State of the Climate in 2023"]. *Bull. Amer. Meteor. Soc.*, **105** (8), S293–S294, https://doi.org/10.1175/BAMS-D-24-0101.1.

Thompson, D. W. J., and J. M. Wallace, 2000: Annular modes in the extratropical circulation. Part I: Month-to-month variability. *J. Climate*, **13**, 1000–1016, https://doi.org/10.1175/1520-0442(2000)013<1000:AMITEC>2.0.CO;2.

Timmermans, M.-L., and Z. M. Labe, 2024: Sea surface temperature. Arctic Report Card 2024, T. A. Moon, M. L. Druckenmiller, and R. L. Thoman, Eds., NOAA Tech. Rep. OAR ARC 24-07, 7 pp., https://doi.org/10.25923/9z96-aq19.

Tretiyakov, M. V., O. V. Muzhdaba, A. A. Piskun, and R. A. Terekhova, 2022: The state of the Roshydromet Hydrological Observation Network in the mouth areas of RFAZ. *Water Resour.*, **49**, 796–807, https://doi.org/10.1134/S0097807822050153.

Tschudi, M., W. N. Meier, J. S. Stewart, C. Fowler, and J. Maslanik, 2019a: EASE-grid sea ice age, version 4. NASA National Snow and Ice Data Center Distributed Active Archive Center, accessed 4 October 2024, https://doi.org/10.5067/UTAV7490FEPB.

——, ——, and ——, 2019b: Quicklook Arctic weekly EASE-grid sea ice age, version 1. NASA National Snow and Ice Data Center Distributed Active Archive Center, accessed 4 October 2024, https://doi.org/10.5067/2XXGZY3DUGNQ.

U.S. National Ice Center, 2008: IMS daily Northern Hemisphere snow and ice analysis at 1 km, 4 km, and 24 km resolutions, version 1. National Snow and Ice Data Center, accessed 3 August 2024, https://doi.org/10.7265/N52R3PMC.

Vandecrux, B., and Coauthors, 2023: The historical Greenland Climate Network (GC-Net) curated and augmented level-1 dataset. *Earth Syst. Sci. Data*, **15**, 5467–5489, https://doi.org/10.5194/essd-15-5467-2023.

Wegmann, M., and Coauthors, 2015: Arctic moisture source for Eurasian snow cover variations in autumn. *Environ. Res. Lett.*, **10**, 054015, https://doi.org/10.1088/1748-9326/10/5/054015.

Wehrlé, A., J. E. Box, A. M. Anesio, and R. S. Fausto, 2021: Greenland bare-ice albedo from PROMICE automatic weather station measurements and Sentinel-3 satellite observations. *GEUS Bull.*, **47**, 5284, https://doi.org/10.34194/geusb.v47.5284.

Williams, R. S., M. I. Hegglin, P. Jöckel, H. Garny, and K. P. Shine, 2024: Air quality and radiative impacts of downward-propagating sudden stratospheric warmings (SSWs). *Atmos. Chem. Phys.*, **24**, 1389–1413, https://doi.org/10.5194/acp-24-1389-2024.

Wolken, G. J., and Coauthors, 2021: Glacier and permafrost hazards. Arctic Report Card 2021, T. A. Moon, M. L. Druckenmiller, and R. L. Thoman, Eds., NOAA Tech. Rep. OAR ARC 21-13, 93–101, https://doi.org/10.25923/v40r-0956.

Yang, X., and Coauthors, 2020: C3S Arctic regional reanalysis—Full system documentation. Copernicus Climate Change Service (C3S), accessed 26 Mar 2025, https://datastore.copernicus-climate.eu/documents/reanalysis-carra/CARRAFullSystemDocumentationFinal.pdf.

Yu, L., and S. Zhong, 2021: Trends in Arctic seasonal and extreme precipitation in recent decades. *Theor. Appl. Climatol.*, **145**, 1541–1559, https://doi.org/10.1007/s00704-021-03717-7.

Zhou, S., A. J. Miller, J. Wang, and J. K. Angell, 2001: Trends of NAO and AO and their associations with stratospheric processes. *Geophys. Res. Lett.*, **28**, 4107–4110, https://doi.org/10.1029/2001GL013660.

Zhou, W., L. R. Leung, and J. Lu, 2024: Steady threefold Arctic amplification of externally forced warming masked by natural variability. *Nat. Geosci.*, **17**, 508–515, https://doi.org/10.1038/s41561-024-01441-1.

Zhu, X., G. Jia, and X. Xu, 2024: Wildfire emissions offset more permafrost ecosystem carbon sink in the 21st century. *Earth's Future*, **12**, e2024EF005098, https://doi.org/10.1029/2024EF005098.